Université catholique de Louvain
Faculté des Bioingénieurs
Earth and Life Institute

Remote sensing of drought stress with sun-induced chlorophyll fluorescence

From canopy to global scale

Simon De Cannière

Thèse présentée en vue de l'obtention du grade de

docteur en sciences agronomiques et ingénierie biologique

Jury de thèse:

Prof. François Jonard (Promoteur)	UCLouvain, Belgique
Prof. Pierre Defourny (Promoteur)	UCLouvain, Belgique
Prof. Marnik Vanclooster (Président)	UCLouvain, Belgique
Prof. Xavier Draye	UCLouvain, Belgique
Prof. Harry Vereecken	Forschungszentrum Jülich, Allemagne
Prof. Ivan Janssens	Universiteit Antwerpen, Belgique

Louvain-la-Neuve, Août 2023

Acknowledgements / Remerciements / Dankwoord

Une thèse de doctorat, c'est tout un processus - la mienne a pris près de cinq ans, avec ses hauts et ses bas, ses moments de galère, mais aussi ses moments de gloire, ses aventures délirantes, des faits tout à fait établis et des surprises bienvenues. En théorie, une thèse c'est un travail très personnel, mais bon, je ne peux pas m'empêcher de remercier différentes personnes qui m'ont soutenu dans les moments difficiles, qui m'ont poussé vers le succès, ou simplement avec qui j'ai partagé de super moments. Avant tout, je tiens à exprimer toute ma reconnaissance envers François pour m'avoir offert l'opportunité de me lancer dans cette recherche et pour ses conseils tout au long du chemin. Ses conseils ont pris différentes formes ; tantôt en tant que guide, tantôt en tant que critique, tantôt en tant que compagnon d'aventure. C'est grâce à lui que j'ai appris les ficelles du métier de chercheur ; depuis le travail théorique jusqu'au travail sur le terrain, des analyses pointues à une vue d'ensemble. Ensuite, un grand merci à Pierre aussi, pour avoir élargi mon horizon en ce qui concerne les observations par satellite, pour les défis intellectuels relevés ensemble et pour son soutien indéfectible.

Apès, je remercie cordialement mes collegues GERU: Axelle, Benoît, Damien, Elise, Jean-Baptiste, Kaijun, Maud, Martin, Sebastien, Timothee: merci pour l'acceuil chaleureux lors de mon arrivée à Louvain-la-Neuve, pour les blagues pendant la pause café, pour les jeux de cartes, pour le voyage incroyable en Namibie, pour les sessions piscine-frite... C'était un grand plaisir de venir au labo grâce à vous!

I also express my sincierest gratitude to my collegues from FZ Jülich. Here, I want to thank Michael Herbst, particularly for teaching how to use the AgroC model, to Harry Vereecken for the discussions on the paper manuscripts. Finally, I want to thank Jordan Bates for the fun

times in Jülich and for the help in the fieldwork, a type of collaboration that I am happy to continue in the upcoming year.
During the PhD, I had the chance to go and visit the research group of Dara Entekhabi in Boston, where I also met the researchers from the German Aerospace Agency. These trips lead to what is now chapter four in this thesis, and I am enormously grateful to David, Martin and Thomas for the intense collaboration and insightful discussions. This collaboration allowed to apply the local-scale knowledge from the two other chapters at the global scale and forms the capstone of this thesis.

Verder een grote bedanking aan de vrienden uit Aartselaar. Bedankt voor de warme zomeravonden, voor de covid-wandelingen en de vele fietstochtjes, wanneer ik 'eventjes' terug in Aartselaar was. Dat jullie in grote getalen de taalgrens oversteken naar 'het verre Wallonië' maakt me uiteraard zeer blij. In deze categorie een extra bedanking aan Robin Van Tendeloo; Robin, je tekening (figuur 2.1) heeft het tot helemaal het einde van het doctoraat gehaald. Ik had het je graag getoond.
Ook een bedanking aan Dieter, Laurens, Lore en Lize. Het is fijn om, na samen te studeren, ook samen de golven van het doctoraatsbestaan te bedwingen en hierin vreugdes en frustraties te delen. En soms nichehumor. A big thank you to my housemates (yes, Anse and Daan, that includes you, no Mr. Mouse, that does not include you) for the wonderful evenings in the Tower, where it was a pleasure to come home from after a day of work or to work from. Many of us lived/are living the same joys and sorrows of the PhD, and it is wonderful to share them with each and every one of you.
Uiteraard ook nog een grote bedanking aan mijn ouders, zussen, Elie en Tom, in het Swaeneleike, in de Gemeentestraat of de Provinciestraat. Bedankt om hierin te geloven van het begin af aan, voor het klankbord, of om mijn enthousiasme te kunnen delen. En voor de onvoorwaardelijke steun.
Indien ik door een vergetelheid iemand ben vergeten te bedanken, gelieve deze vergetelheid als dusdanig te beschouwen ;).

Contents

Acknowledgements / Remerciements / Dankwoord iii

Contents v

List of acronyms and symbols vii

1 Introduction 1
- 1.1 Societal context . . . 1
- 1.2 Drought monitoring techniques . . . 2
- 1.3 A brief history of photosynthesis research . . . 3
- 1.4 Connecting photosynthesis and chlorophyll fluorescence . . . 3
- 1.5 Chlorophyll fluorescence . . . 5
- 1.6 Physiological response of plants to drought . . . 6
- 1.7 Remote sensing of drought stress . . . 13
- 1.8 Objectives and general outline of the thesis . . . 20

2 Observed effect of drought on SIF at the canopy scale 23
- 2.1 Introduction . . . 25
- 2.2 Materials and methods . . . 27
- 2.3 Results . . . 33
- 2.4 Discussion . . . 44
- 2.5 Summary and outlook . . . 48

3 Constraining a crop growth model with SIF data 51
- 3.1 Introduction . . . 53
- 3.2 Materials and methods . . . 56
- 3.3 Results . . . 77
- 3.4 Discussion . . . 83
- 3.5 Summary and outlook . . . 86

3.6 Appendix: description of the photosynthesis model based on Farquhar approach 86

4 Water availability and atmospheric demand controls on space-borne SIF yield 89
4.1 Introduction 91
4.2 Materials and Methods 93
4.3 Results 105
4.4 Discussion 119
4.5 Conclusion 124
4.6 Appendix 125

5 Conclusion and perspectives 129
5.1 Key findings 129
5.2 Research Perspectives 131
5.3 Towards operational applications in the near and distant future 134

Bibliography 141

Abstract 171

List of acronyms and symbols

Greek symbols

α	Stress factor
β	Fitting parameter for calculating K_N
γ	Fitting parameter for calculating K_N
δ_A	Minimum degradation rate
δ_ψ	Minimum production rate
ϵ_{760}	Fluorescence emission efficiency at 760 nm
ζ	Quantum efficiency
κ	Conversion factor from leaf- to canopy level fluorescence
λ	Wavelength
λE	Latent heat
ν	Fitting parameter for K_n
ρ	Pearson's correlation coefficient
σ	Slope of the morning-noon VOD curve, degree of anisohydricity
τ_p	Expected standard deviation of considered PROSAIL parameter p
ϕ_F	Fluorescence yield

$\phi_{F'_m}$	Maximal fluorescence yield
ϕ_N	Non photochemical quenching yield
ϕ_P	Photochemical quenching yield
ϕ_{P0}	Maximal photochemical quenching yield
ψ_{leaf}	Leaf water potential
ω	Angular direction

Variables

$APAR$	Absorbed Photosynthetically Active Radiation
Chl	Chlorophyll
C_{dm}	Leaf dry matter
C_w	Leaf water content
$ET0$	Reference Evapotranspiration
f_{esc}	Escape probability
F_0	Steady-state fluorescence emission under low-light conditions
F_s	Steady-state fluorescence under hight light conditions
$FCVI$	Fluorescence Correction Vegetation Index
G_s	Canopy conductance
$h_1 - h_4$	Feddes parameters
h	Soil suction
J_F	Fluorescence electron flow
J_P	Photochemical electron flow
J_N	NPQ electron flow

K_c	Crop coefficient
K_D	Fluorescence thermal decay rate constant
K_F	Fluorescence rate constant
K_m	Michaelis-Menten Fitting Parameters
K_N	NPQ rate constant
K_{N0}	Fitting parameter for calcualting K_N
$K_{N,avg}$	NPQ rate constant modelled calculated according to weighted average on drought conditions
$K_{N,drought}$	NPQ rate constant modelled with drought parameters
$K_{N,standard}$	NPQ rate constant modelled with standard parameters
K_P	Photochemical rate constant
$NIRvP$	NDVI multiplied by NIR reflectance and PAR
R_λ	Reflectance at wavelength λ
$R_{\mathbf{gas}}$	Universal gas constant
x	Light saturation

Acronyms

ABA	Abscisic acid
AMSR-E	Advanced Microwave Scanning Radiometer for EOS
ATP	Adenosine Triphosphate
BETHY	Biosphere Energy Transfer HYdrology
ChlF	Chlorophyll fluorescence
CLM	Community Land Model
CWSI	Crop Water Stress Index

EASE-2 Equal Area Scalable Earth version 2

EC Eddy Covariance

EP Evaporation

EUMETSAT European Meteorological Satellite

ESA European Space Agency

ETA Actual evapotranspiration

FAO Food and Agriculture Organization

FLD Fraunhofer Line Depth

FLEX Fluorescence EXplorer

FLORIS FLuorescence Imaging Spectrometer

FloX Fluorescence Box

fPAR fraction of photosynthetically active radiation

GOCI Geostationary Ocean Color Imager

GOME-2 Global Ozone Monitoring Experiment-2

HR High Resolution

ICOS Integrated Carbon Observatory System

iFLD Improved Fraunhofer Line Depth

LAI Leaf Area Index

LHCII Light-harvesting complexes II

LIDF Leaf Inclination Distribution Function

LR Low Resolution

MT-DCA Multi Temporal - Dual Channel Algorithm

MTG-S Meteosat Third Generation Sounder

NEE	Net Ecosystem Exchange
NADPD	Nictotinamide adenine dinucleotide phosphate
NASA	National Aeronautics and Space Administration
NPQ	Non-photochemical quenching
NSE	Nash-Sutcliffe Efficiency
PAM	Pulse-Amplitude Modulation
pF	*potenz Freier Energie*; Free energy of water
PQ	Plastoquinone
PSI	Photosystem I
PSII	Photosystem II
PRI	Photochemical Reflectance Index
PROSAIL	PROSPECT (*Propriétés Spectrales*; Spectral properties) + SAIL (Scattering by Arbitrarily Inclined Leaves)
$\mathbf{Rad_{glob}}$	Global Radiation
Res	Respiration
ROS	Reactive Oxygen Species
Rubisco	Ribulose-1,5-bisphosphate carboxylate/oxygenase
SCOPE	Soil Canopy Observations Photosynthesis Energy
SFM	Spectral Filling Method
SIF	Sun-Induced chlorophyll fluorescence
SM	Soil Moisture
SMAP	Soil Moisture Active Passive
SMOS	Soil Moisture Ocean Salanity

SSiB2 Simplified Simple Biosphere model 2.0

TERENO Terrestrial Environmental Observatory

TROPOMI TROPOspheric MOnitoring Instrument

VCMax Maximum carboxylation capacity

VPD Vapour Pressure Deficit

USDA United States Department of Agriculture

VOD Vegetation Optical Depth

Y(II) Actual PSII efficiency

Chapter 1

Introduction

1.1 Societal context

Climate change is altering global precipitation patterns, leading to an increase in the frequency, duration, and intensity of droughts. Unlike floods, which have a very clear onset, ending, and intensity, the definition of drought, as well as its duration, is more context-dependent. In crop science, as well as in ecology, drought is often defined as a period in which water limits plant development. This leads to reduced crop yields, or reduced tree devolopment. These have, in turn, various socio-economic consequences, such as rising food prices. The annual cost of droughts in the EU and UK combined is estimated between 9.7 and 17.3 billion €, half of which falls on the agricultural sector. These drought-induced costs include money spent on irrigation water, drilling new wells, as well as crop yield loss (Cammellari et al., 2020). Traditionally, droughts have been managed as an emergency, but policymakers are

1.5-1.6 were taken from Jonard, F., **De Cannière, S.**, Brüggemann, N., Gentine, P., Short Gianotti, D.J., Lobet, G., Miralles, D.G., Montzka, C., Pagán, B.R., Rascher, U., Vereecken, H. (2020). Value of sun-induced chlorophyll fluorescence for quantifying hydrological states and fluxes: Current status and challenges. Agricultural and Forest Meteorology 291. The candidate was in charge of these paragraphs.

stressing their need for early drought detection mechanisms, allowing them to match the water availability with the water demand in earlier stages of a drought, through e.g., careful irrigation planning (Hervás-Gámez and Delgado-Ramos, 2019), or by a more adequate crop choice.

1.2 Drought monitoring techniques

As food is an essential element for any society to thrive, techniques to predict harvests exist for centuries. A famous example from the Middle Ages and Early Modern Era are the *Hungersteine* (hunger stones), found in various cities on the Elbe River. These stones were put on certain levels of the river floor and served as a warning if the water level dropped below the level of the hunger stones, making them visible, indicating that the year's harvest will be poor and that food rationing should begin (Elleder et al., 2020). A more formal metric to determine regional-scale drought is the Palmer Drought Severity Index (PDSI), which relies on in-situ measurements of temperature and precipitation (Palmer, 1965). However, these methods do not take into account the vast variety of plant drought reactions. A defining moment was the launch of the Landsat satellite in 1972, as it allowed to monitor the vegetation greenness which then serves as a proxy for vegetation status, at a large scale. Over the last 50 years, greenness has proved its value in drought stress monitoring (West et al., 2019). However, these techniques lack physiological interpretation. More recent techniques have attempted to remotely sense information in a way that is closer to the physiology of the plant. A good example here is thermal remote sensing, which is sensitive to the increase in sensible heat flux on the leaves, but it needs a large amount of ancillary data for a proper interpretation (Zhou et al., 2021). These ancillary data include data on the background termperature, as well as a wet and dry reference for the leaf. Today, various researchers are looking for remote sensing signals that can be interpreted in terms of physiological processes. Here, the process of photosynthesis is one of the most interesting processes to monitor with a remote sensing infrastructure.

1.3 A brief history of photosynthesis research

Photosynthesis is nothing less than a miraculous process that forms the backbone of all life on Earth. Consequently, it is one of the most ancient and fundamental subjects of scientific research. The first research on photosynthesis can be traced back to 1644, when the Belgian physician Jan Baptist Van Helmont described, in an early scientific style, how plants arose from water and chaos, and suggested that process to be the 'reverse' of a burning process. In the late 1600s, the Englishman John Woodward described that water is consumed by the plant in its growth process rather than it being used as a nutrient (Ducheyne, 2008). The first notion of the chemical nature of the concept of photosynthesis came in the Summer of 1770, when the Dutch-English physician Jan Ingenhouz observed the creation of gas in plants in the presence of sunlight. While the term photosynthesis was not coined until 1891 (Gest, 2002), these early works describe the two requirements for a plant to perform photosynthesis: water and energy.

1.4 Connecting photosynthesis and chlorophyll fluorescence

The need for water and energy in photosynthesis can be traced back to its biochemical origins. Photosynthesis breaks down into two families of biochemical reactions; the light and dark reactions (Figure 1.1). In the light reactions, a chlorophyll molecule harvests the energy from photons sent out by the Sun, and funnels it down a series of photochemical reactions, thereby producing adenosine triphosphate (ATP), nicotinamide adenine dinucleotide phosphate (NADPH) and Nicotinamide adenine dinucleotide (NADH), that serve as energy and electron carriers (Rabinowitsch and Govindjee, 1969). These carriers are then sent to the dark reactions, also referred to as the Calvin cycle. In the latter family of reactions, atmospheric CO_2 is assimilated into carbohydrates. The CO_2 enters the leaf through the stomata, small openings in the leaf surface that can open and close in the function of the environmental conditions. This process is catalyzed by the enzyme ribulose-1,5-biphosphate carboxylase oxygenase (Rubisco) and consumes the energy stored in ATP and NAD(P)H (Bassham et al.,

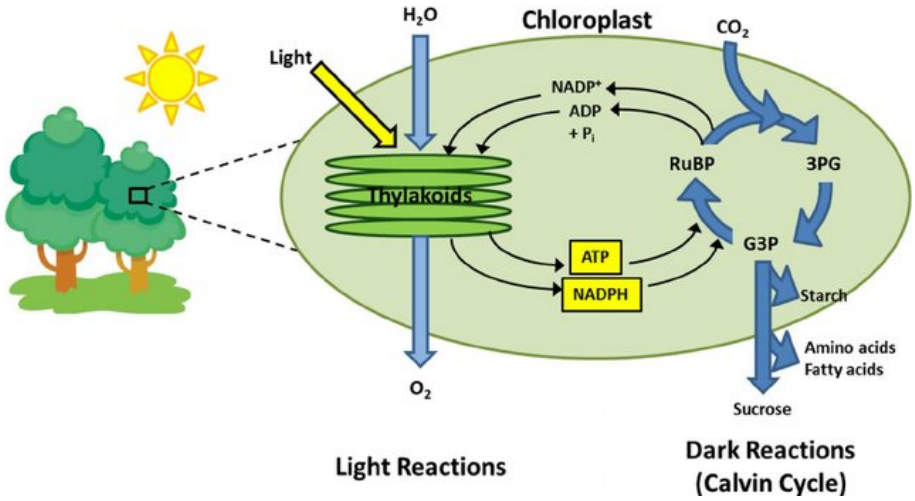


Figure 1.1: Schematic overview of photosynthesis (Rasmussen and Minteer, 2014).

1950). Like any kind of complex machinery, the rate of the light and dark reactions must be in tune with each other.

Given the highly dynamic nature of the availability in sunlight and in atmospheric water demand, a plant possesses various regulatory mechanisms that allow to finetune the rate by which the light reactions are happening. Specifically, an absorbed photon in the photosystem can go down three pathways, the photochemistry, the heat dissipation, called the non-photochemical quenching (NPQ) and the chlorophyll fluorescence. NPQ is the mechanism that plants use to prevent an accumulation of energy in the photosynthetic electron transport chain, and an increase of it induces a change in the fluorescence emission. A stress can lead to a reduction in the carbon assimilation rate, forcing the light reactions to follow and increase the NPQ component. It is important to realize that NPQ is not the same as the increase in sensible heat flux. The sensible heat flux finds its origins in irradiation that has not been absorbed by chlorophyll molecules. Despite NPQ not being a significant heat source to the plant, drought stress does cause both NPQ and the sensible heat flux to increase.

A tool to connect the molecular origins of photosynthesis to the macro-process of plant development is chlorophyll fluorescence. The

intensity of chlorophyll fluorescence is linked to the various aspects of photosynthesis, most notably to the NPQ rate. First described in 1931 (Kautsky and Hirsch, 1931), chlorophyll fluorescence became a cornerstone in the field of leaf-scale photosynthesis. More recently, advances in spectrometer technology enabled us to study chlorophyll fluorescence from airborne and satellite-based sensors, the sun-induced chlorophyll fluorescence (SIF). Since these sensors allow to monitor of vast areas frequently, large-scale data on chlorophyll fluorescence enable the monitoring of large-scale photosynthesis. This use of fluorescence data dissonates with their traditional usage, as a tool to measure photosynthesis at the molecular and the leaf scales. However, information on large-scale photosynthesis provides key information on the water and carbon cycles.

1.5 Chlorophyll fluorescence

Photosynthesis strongly depends on environmental variables, such as soil and leaf water potentials, water vapour pressure deficit, or soil nutrient concentration (Jarvis, 1976). The measurement of chlorophyll fluorescence (ChlF) might therefore provide valuable information on how these environmental variables control photosynthesis. While ChlF has been investigated for nearly a century, mainly under laboratory conditions and by using active detection methods, many questions remain. How does ChlF emission change in function of photosynthetic activity? What is the impact of drought stress on ChlF emission? Better understanding the behaviour of the ChlF emission at different scales (from chloroplast to ecosystem) –and how this emission is driven by stress-induced changes in photosystem-level ChlF emission and in canopy structure (Dechant et al., 2020) –may provide opportunities to improve the understanding of the role of photosynthesis in the coupling of the carbon and water cycles (Gentine and Alemohammad, 2018). Fluorescence measurements can be performed at different spatial scales (from the leaf to the ecosystem scale) and temporal resolutions (from seconds to years). The different measurement techniques can be classified as active and passive. Active systems use an artificial source of energy to excite ChlF, while passive systems measure ChlF induced by the absorption of sunlight. Active methods use

light pulses of different intensities. The shape of the fluorescence response to these pulses, as well as the relative height of the different pulse-induced peaks, provide information about the state of photosynthesis (Govindjee, 1995), therefore enabling the detection of abiotic stresses, including drought (Stirbet et al., 2018). The current standard in active fluorescence is the Pulse-Amplitude Modulation (PAM) (Schreiber et al., 1986). Passive techniques can measure SIF over large scales thanks to advances in spectrometer technology in terms of spectral resolution and accuracy during the last decade (Li et al., 2022; Mohammed et al., 2019). Unlike active measurements, they rely on the absolute value of the emitted fluorescence under natural light conditions and therefore are dependent on the absorbed radiation and the information content of SIF is lower than one can expect from active approaches. As SIF amounts to only between 1 and 3 % of the absorbed shortwave radiation, it can only be measured in specific spectral bands, in which solar irradiation is reduced (paragraph 1.7.2). Early studies of ChlF have mainly focused on the relation between ChlF and photosynthetic activity or carbon assimilation at the leaf level (Govindjee, 1995). More recently, with increased developments in passive measurement techniques allowing estimates of SIF over large spatial scales, several research initiatives have investigated the value of SIF as a constraint for land surface models, in particular for gross primary production (GPP) of vegetation canopies (Liu et al., 2022; MacBean et al., 2018; Wieneke et al., 2016) and crop yield (Guanter et al., 2014). As photosynthesis is closely linked to hydrological processes, information on SIF may help to illuminate processes within the soil-plant-atmosphere continuum (Maes et al., 2020; Short Gianotti et al., 2019).

1.6 Physiological response of plants to drought

1.6.1 Interactions between photosynthesis and plant hydraulics

Photosynthetic response to low soil water potential is complex. Between the dry soil with low water potential and the site of photosynthesis, the path of water is regulated at many sites in the plant (Figure 1.2). Locally, the hydraulic conductivity of soil and roots varies with soil water potential, especially in the vicinity of fine roots (Siqueira et al., 2009). On short time scales (minutes to hours), water channels,

or aquaporins, can be downregulated or gated as soil water potential decreases and thus reduce the flow of water between cells (Cochard et al., 2007). On longer time scales (hours to days), root segments growing in soil regions with low soil water potential can also develop hydrophobic barriers by depositing suberin, a hydrophobic compound, in specific root layers (Barberon et al., 2016). These two processes have the direct effect of hydraulically isolating the root from its direct dry environment, hence preventing a drop in internal xylem water potential. The sensitivity of these responses has been shown to be variable between plant species (Martínez-Ballesta et al., 2003). A second layer of control lies within the network of xylem vessels. Xylem vessels are straw-like organs, responsible for water transport from the root system up to the leaves, based on a difference in water potential between the soil and the leaves. However, when the potential difference within the vessels exceeds a certain threshold, an embolism occurs, i.e., gas bubbles start to form; a process referred to as cavitation (Sperry and Love, 2015). Wherever cavitation occurs, the hydraulic conductivity of the corresponding xylem element drops, blocking the flow in that part of the xylem. Some suggest cavitation to be a blessing in disguise, as the lowered xylem transport lowers the plant transpiration (Vergeynst et al., 2015). Depending on the intensity of the cavitation, plants can refill the embolized vessels (Zwieniecki and Holbrook, 2009), however, this refiling process shows plant-level variation (Cochard et al., 2007). The plant hydraulics affect the photosynthesis through the stomata. Due to the decrease in water potential within the substomatal cavities and hormonal triggers, stomata may partially close, reducing the amount of CO_2 entering the plant and therefore decreasing photosynthesis, and at the same time reducing the flux of vapour into the atmosphere through transpiration (Lemordant et al., 2016). The sensitivity of guard cells to hydraulic and hormonal signals (Tardieu et al., 2015) determines the plant water response. Plants with a near-isohydric behaviour limit xylem cavitation through early stomatal closure, while plants with more anisohydric behaviour keep their stomata more open while drought progresses, thus sustaining higher transpiration rates (Konings and Gentine, 2017; Novick et al., 2019). These two strategies can be species-specific (e.g., cactus is isohydric, while lettuce is anisohydric), but also genotype-specific, as observed in tomatoes (Sade et al., 2012) or even vary with drought level, with the phenology (Gong

et al., 2022), or with the root system architecture (Javaux and Carminati, 2021). The second form of response occurring under drought conditions is a non-stomatal limitation of photosynthesis. This limitation is measured as the change in the ratio between the net CO_2 assimilation rate and the leaf-internal CO_2 concentration (A–Ci curve) (Long and Bernacchi, 2003; Zhou et al., 2013), which can be divided into two components. The first is the reduction of the mesophyll conductance to CO_2 (Flexas et al., 2016). This limitation can be large and is thought to be due to a down-regulation of aquaporins (Flexas et al., 2006). The second type of non-stomatal limitation is linked to a reduction in the metabolic efficiency of the enzyme Rubisco due to a reduction in CO_2 availability (Grassi and Magnani, 2005). Under normal conditions, there is a strong coordination between Rubisco activity and the CO_2 diffusional characteristics of leaves. However, under prolonged water deficit (several days), this coordination is lost and less reversible damages start to occur, such as the deterioration of thylakoid membranes (Sperdouli and Moustakas, 2012). The relative contribution of the stomatal and non-stomatal limitations is not constant and varies between species (Zhou et al., 2013), cultivars (Bota et al., 2016), developmental stages (Egea et al., 2011) and stress severity (Galmés et al., 2007). Over longer periods of severe water stress, leaf area per plant decreases, as does chlorophyll density within leaves, xylem conductivity, and vegetated-to-bare soil ratio.

1.6.2 Fluorescence response on the drought stress

Stomatal and non-stomatal responses to drought result in a lower internal CO_2 in the sub-stomatal chambers, reducing the efficiency of the Calvin cycle. This leads to a lower demand of ATP and NADPH which, in turn, slows down the photosynthetic electron transport (Vanlerberghe et al., 2016). The lowered ATPase activity causes protons to accumulate in the thylakoids, resulting in a pH gradient over the thylakoid membrane (Campos et al., 2014; Cousins et al., 2002). The increased pH gradient over the thylakoid membrane triggers an increase in non-photochemical quenching (NPQ), leading to a change in fluorescence emission at the photosystem level, i.e., in fluorescence yield (ϕ_F). NPQ covers a variety of biochemical and biophysical processes that dissipate the excess energy from the photosystems, avoiding the

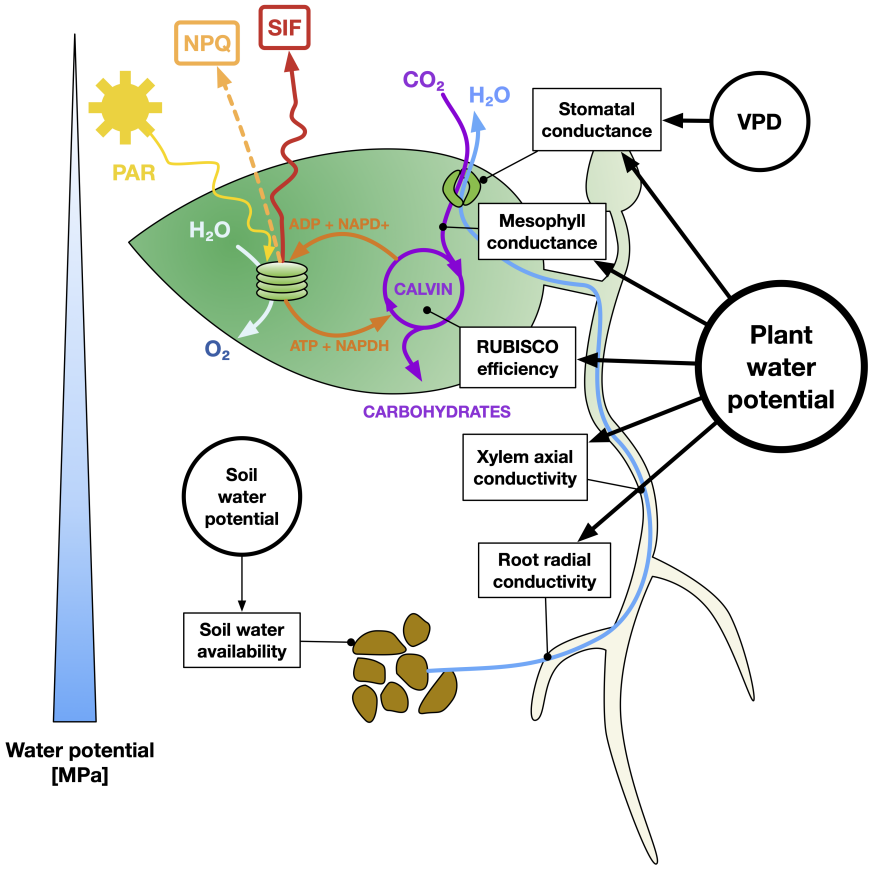


Figure 1.2: Overview of plant scale processes and water potential gradient in the soil—plant—atmosphere continuum (Jonard et al., 2020).

formation of reactive oxygen species (ROS) and the concomitant destruction of the photosynthetic complexes (e.g., Jahns and Holzwarth, 2012; Niyogi and Truong, 2013). The main sub-processes of NPQ are triggered by the increased pH gradient also causes kinases to move light-harvesting complex II (LHCII) from PSII to PSI (Campos et al., 2014; Kruger et al., 2012). This process is linked with the phosphorylation of the PSII, inactivating it, and preventing it from funneling photons down the electron transport chain (Niyogi and Truong, 2013). This way, the PSI-bound LHCII provides photoprotection for PSI. Un-

like linear electron transport, cyclic electron transport does not produce NADPH, allowing adaptation to the decreased Calvin cycle activity (Figure 1.3). A second process modulating the transfer of energy to the photosynthetic electron transport chain is the damage and repair cycle of PSII (Jin et al., 2003). An overstimulation of PSII leads to the production of singlet oxygen, inducing reversible damage to the PSII. If the damage occurs at a faster rate than the repair, the downstream energy transfer is slowed down. This phenomenon is called photoinhibition (Demmig-Adams et al., 2012).

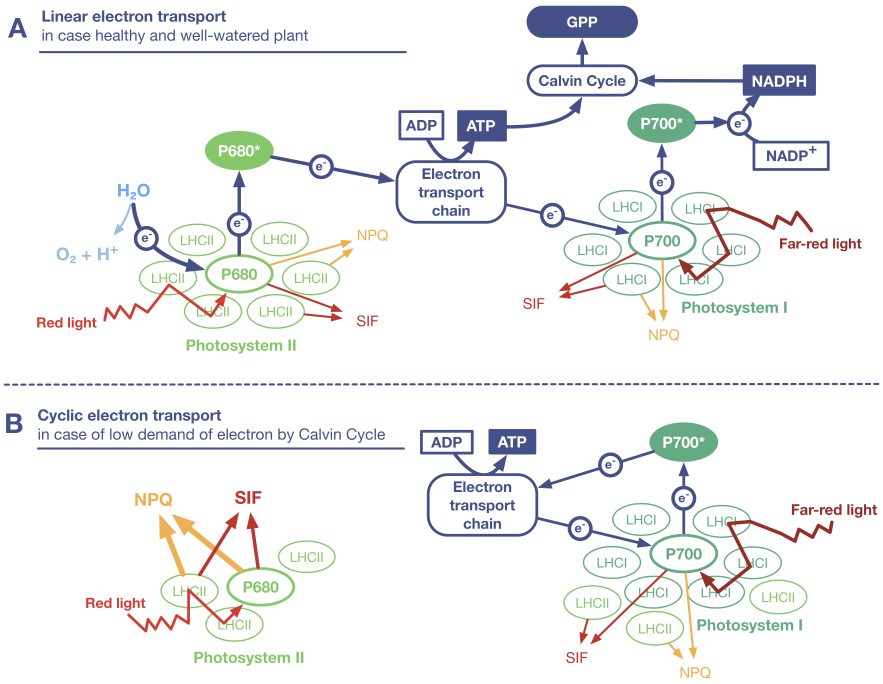


Figure 1.3: Visualization of linear (A) and cyclic (B) electron transport in photosynthesis (Jonard et al., 2020).

The movement of the light-harvesting complexes and the increased pH gradient over the thylakoid membrane alters the partitioning of energy between the pathways of photosynthesis, heat dissipation (both regulated and non-regulated) and fluorescence, the latter two providing an alternative electron sink to photosynthesis. The effect of drought

stress on the fluorescence itself differs at the photosystem level. Upon overstimulation, either by over-illumination or by a reduced plastoquinone pool, the sum of the energy dissipated by NPQ increases, protecting PSII from photobleaching. The PSI is protected by the movement of LHCII to PSI and by the cyclic electron transport around it (Porcar-Castell et al., 2014), reducing the need for NPQ-based photoprotection of PSI (Miyake et al., 2004). In addition, other environmental factors can interact with drought stress and influence the photosynthetic efficiency and fluorescence emission. Nitrogen (N), for instance, is an important component in the synthesis of photosynthetic pigments and Rubisco. As such, N availability can play a role in the response of photosynthesis to drought stress. In winter wheat, an appropriate level of N supply has been shown to improve the photosynthesis response to decreasing soil water content and to decrease the effect of drought stress (Wang et al., 2016). Low N levels, in combination with drought, can lead to more severe reductions of photosynthesis (Wang et al., 2016; Wu et al., 2008). There are only very limited studies available on the link between low temperatures (chilling) and SIF. Ač et al. (2015) found in their meta-analysis a larger increase in far-red fluorescence compared to red fluorescence in response to chilling stress, which could be attributed to a reduction of plastoquinone (PQ). Other studies using active fluorescence methods seem to support this and, for example, (Lin et al., 2007) observed an increase in minimal fluorescence yield in the dark-adapted state (F0) because of chilling stress. Wang et al. (2016) observed a decrease in thylakoid membrane fluidity, blocking electron transfer in the PSII reaction centres and reducing NPQ, also resulting in increased fluorescence. High temperature (heat) stress is often associated with drought stress, as high air temperatures increase the atmospheric vapour pressure deficit. In addition to the drought effect, heat stress tends to damage the chloroplast membranes, changing the activity of various proteins (Feng et al., 2014). Consequently, heat stress results in a decrease in both red and far-red fluorescence (Ač et al., 2015).

Connecting the dots from the previous studies, the following story can be built to explain the mechanistic link between drought stress and chlorophyll fluorescence: during a drought, a plant tends to close its stomata, saving up on its water use at the expense of a lowered CO_2 uptake, thereby lowering the energy demand by the Calvin cy-

cle. Through a series of regulatory mechanisms, the energy harvested by the photosynthetic light reactions and the energy consumed by the Calvin cycle are neatly equilibrated. An excess of energy at the level of the photosystems leads to the production of reactive oxygen species (ROS), damaging the proteins in the plant. At sub-second timescales, ROS production is prevented by providing for alternative electron sinks within the photosynthetic electron transport chain. This alternative sink is regulated through a series of different mechanisms, collectively referred to as non-photochemical quenching (NPQ). In order to retrieve ϕ_F from remote sensing data, a two-step approach is imperative. The first step deals with retrieving the sun-induced chlorophyll fluorescence (SIF), using methods that rely on Fraunhofer lines or oxygen absorption lines. In a second instance, SIF needs to be corrected for the photosynthetically active radiation (PAR), by the fraction of absorbed photosynthetically active radiation (fPAR), as well as the escape probability (fesc). All three beforementioned factors show dynamics at the second's timescale, as each of them has a sensitivity to the meteorological conditions.

1.6.3 Link between soil moisture and fluorescence: findings from experimental studies

Various experimental studies have explored the potential of specific parameters derived from active measurements of chlorophyll fluorescence to provide information on soil moisture status in the root zone. Analysis of existing literature shows contradictory information about the effect of soil moisture on ChlF. Depending on the studied species, and the type and intensity of the stress applied, either no effect, a positive, or a negative effect of soil moisture were observed on parameters related to active measurements of ChlF. These diverse results may be partly explained by the non-uniformity in the studied stress duration, the type of plant, the type of soil or also the soil moisture levels imposed in these studies. As the relationship is nonlinear in nature and depends on the range of soil moisture values, a range of dependence may be found, while for high soil moisture values, minimal stress is expected. While some studies report soil moisture only in qualitative wet/dry terms (e.g., Pettigrew, 2004), even quantitative inter-comparison of the soil moisture/ChlF relationship across stud-

ies is hampered by difficulty converting between gravimetric (Kebbas et al., 2015; Man et al., 2017; Xia et al., 2014; Xu and Zhou, 2011), volumetric (Gajanayake and Reddy, 2016; Lang et al., 2018; Trigo-Córdoba et al., 2015), and soil water potential (Li et al., 2004; Snider et al., 2014; Vincent et al., 2015) methods without sufficient reported soil characteristics for inter-conversion. To some degree, this is a disciplinary disconnect between hydrological and physiological lenses. Necessary root zone variables to fully determine the soil moisture/ChlF relationship are soil water potential—preferably as a profile in depth, root water potential, and magnitude and duration of soil moisture deficits.

1.7 Remote sensing of drought stress

1.7.1 Traditional approaches for remote sensing of drought stress

For decades, the workhorse for remote sensing-based drought stress detection came in the form of the Normalized Difference Vegetation Index (NDVI; Rouse et al., 1973), a metric sensitive to the chlorophyll content, as well as to the canopy structure. The concept is relatively simple; a poorly-watered ecosystem has less chances to properly develop itself, leading to smaller, or less green plant material. The approach has proven its value over various ecosystems, from temperate ecosystems to drylands (Caturegli et al., 2020; Ihuoma and Madramootoo, 2019; West et al., 2019), but its is prone to saturation. Other research has developed more refined vegetation indices, all of which were sensitive to other vegetation traits, such as leaf chlorophyll content with the Meris Terrestrial Chlorophyll Index, (MTCI; Dash and Curran, 2004), the vegetation structure with the Modified Triangular Vegetation Index (MTVI2) (Haboudane et al., 2004). However, rather than sensing the stress itself, NDVI rather measures the accumulation of the stress that an ecosystem has gone through during its history. Consequently, a link between vegetation indices and instantaneous stress—stress at the moment of the measurement —is not straightforward. At the turn of the century, the scientific community showed a growing interest in remote sensing indicators that were closer to plant physiology. A noteworthy indicator here is the Normalized Difference Water Index (NDWI; Gao, 1996), which is sensitive to the absorption of in the shortwave infrared by the mesophyll water. With an improvement in spectrometer tech-

nology, vegetation indices could also focus on nanometre-scale absorption features. Here, the photochemical reflectance index (PRI; Gamon et al., 1992) is an important indicator, as it is linked to the relative importance NPQ component. While vegetation indices have shown empirical links with ecosystem water status, a mechanistic link to ecosystem water status is hard to obtain (Damm et al., 2018). The lack of this mechanic link limits the ecological interpretation of such indices to a specific region (De Lannoy et al., 2022). A more mechanistic method is the metrics that rely on thermal remote sensing. This technique makes use of the heating up of the leaves as a result of drought stress, as drought stress leads to a reduction in the latent heat flux due to a partial closing of the stomata, leading to an increase in the sensible heat flux. Thermal remote sensing carries an imprint of the instantaneous stress, but the entire ecosystem around a plant can heat up during drought periods, impeding the interpretation of land surface temperature data. Despite of that, assimilating thermal remote sensing data did improve the modelling of carbon and water fluxes (Huang et al., 2019). In the last 10 years, novel techniques are arising, allowing for a mechanistic-based remote sensing of the plant water status. Two techniques are especially promising here: the vegetation optical depth and the sun-induced chlorophyll fluorescence. While the Vegetation Optical Depth (VOD) is linked to the attenuation of microwaves by the water in the vegetation (Meyer et al., 2019), the sun-induced chlorophyll fluorescence (SIF) comes from the heart of the photosynthetic apparatus.

1.7.2 Retrieval of SIF

The idea of using chlorophyll fluorescence as a remotely sensed variable (McFarlane et al., 1980) is, in fact, not a lot younger compared to the NDVI (Rouse et al., 1973). However, while the NDVI relies on broadband observations of red and NIR radiance, SIF retrieval comes with more difficulties. A chlorophyll molecule's fluorescence emission tends to vary between 1 and 3% of its absorbed radiation, numbers that are dwarfed by the percentages of the reflection. Consequently, a series of filters are needed to insulate the fluorescent light from the reflected light. Nature provides these filters in the form of Telluric bands, as well as in the form of Fraunhofer lines. In both these filters,

the solar irradiation is strongly reduced, by the atmosphere and by the metals in the outer Solar layers, respectively. These bands have a sub-nanometre width, therefore a high-quality spectrometer is imperative for SIF retrieval. Amidst the lowering costs and improving resolutions of spectrometers during the last and current decade, measurements with a high spectral resolution, including SIF measurements are becoming more and more available (Li et al., 2022).

The first algorithm designed for SIF retrieval was the Fraunhofer Line Depth (FLD) method (Plascyk and Gabriel, 1975). This algorithm compares the up- and downwelling radiation in- and outside the Fraunhofer line or Telluric band. A Fraunhofer line is caused by absorption at the outer Solar layers, while Telluric lines find their origin in atmospheric absorption. The relative enrichment of the upwelling radiation inside the Fraunhofer line is then an estimate for the SIF emission. This approach is later refined to rely on multiple Fraunhofer lines or Telluric bands (e.g., Maier, 2002), and by introducing correction coefficients (e.g. Alonso et al., 2008). A more sophisticated approach is the spectral filling method (SFM), which relies on all available Fraunhofer lines and Telluric bands.

The two major Telluric bands are the O_2 absorption lines. These are notably deeper than the Fraunhofer lines, or than the other Telluric bands, making SIF retrieval relatively easier in these bands. For this reason, they have established themselves as the main bands for SIF retrieval in airplane- or tower-based experiments. SIF retrieved in the O_2-B absorption band, at 687 nm is referred to as SIFB, by some authors also called SIFB, while its counterpart at the O_2-A band is referred to as SIFA. While most operating spaceborne SIF data products rely on the solar absorption lines, the upcoming FLuorescence EXplorer (FLEX) satellite is planned to retrieve its SIF based on a SFM that exploits infromation from both the O_2 absorption lines (European Space Agency (ESA), 2015), allowing SIF to be retrieved in different wavelengths (Drusch et al., 2017).

It is interesting to retrieve wavelength-dependent SIF, as its properties are wavelength-dependant. The first difference is in the relative contribution of PSII and PSI to the SIF signal, in which SIFA is relatively more affected by PSI compared to SIFB (Figure 1.4). A second aspect is a difference in re-absorption; since the emission and absorption

spectra of chlorophyll overlap (Figure 1.5) when wavelength $\lambda < 700$ nm. In this region, the SIF is prone to re-absorption, since chlorophyll molecules located in the upper leaf layers can re-absorb upwelling fluorescent radiation.

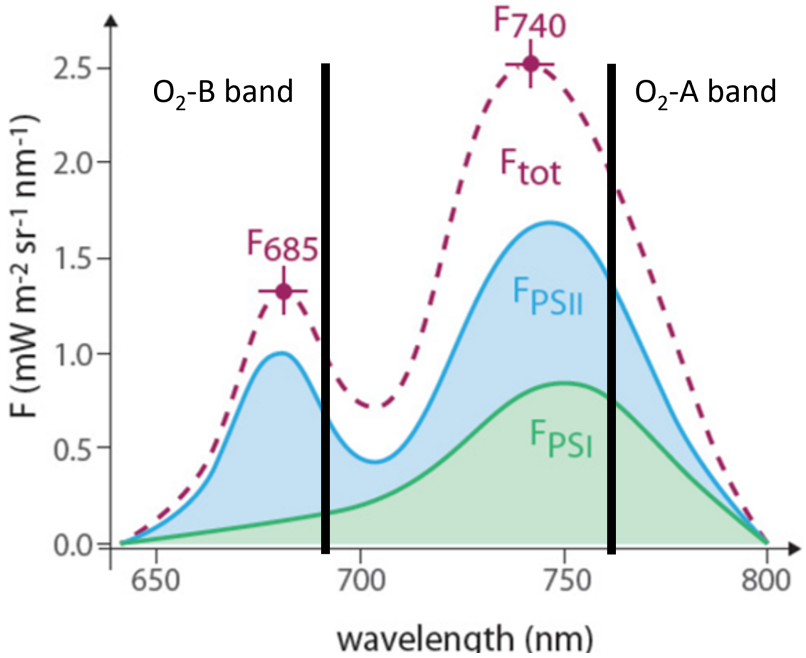


Figure 1.4: Relative contribution of two photosystems along fluorescence spectrum (Drusch et al., 2017). 685 nm and 740 nm are the maxima of the fluorescence emission curve. F_{PSI} and F_{PSII} represent the contribution of each of the photosystems.

1.7.3 Global SIF observations

As a result of the ever-increasing quality and ever-lowering costs of spectrometers, various spaceborne spectrometers allow for global-scale SIF retrievals. The first satellite that allowed for a global SIF retrieval was the Global Ozone Monitoring Experiment (GOME) on the European Remote Sensing Satellite 2 (ERS-2), that provided SIF retrievals from 1995 onwards (Joiner et al., 2022). The current state-of-the-art

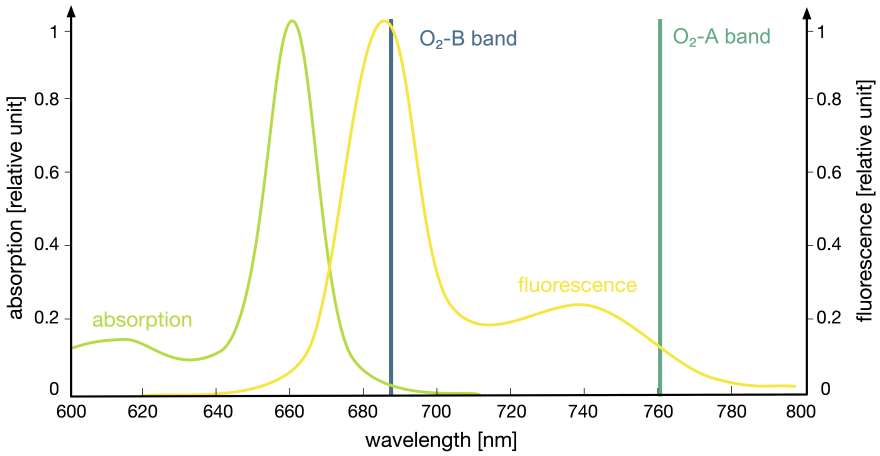


Figure 1.5: Absorption and fluorescence spectra of dissolved chlorophyll with main Telluric bands (Jonard et al., 2020).

global SIF database comes from the TROPOspheric Monitoring Instrument (TROPOMI), aboard the Sentinel-5 precursor satellite (Guanter et al., 2021). Both sensors provide daily global coverage. Up until now, these spectrometers have been tailored to the monitoring of atmospheric trace gasses, and therefore not to SIF retrieval, leading to sub-optimal SIF measurements, at kilometre-scale spatial resolutions. In this aspect, the FLuorescence EXplorer (FLEX), the 8th Earth Explorer mission from the European Space Agency, is expected to be a game-changer, as it will be the first mission dedicated to fluorescence measurements (Drusch et al., 2017) and is expected to launch in 2025. FLEX will fly in tandem with the Sentinel-3 satellite. This tandem schedule allows FLEX to makes use of Sentinel-3's atmospheric parameters (clouds, aerosols, water vapour) observations to minimize any artefacts from the atmospheric composition on the FLEX SIF retrieval (Sabater et al., 2015). FLEX will host the Low Resolution Fluorescence Imaging Spectrometer (FLORIS LR), acquiring data in the red edge, chlorophyll absorption and Photochemical Reflectance Index bands (500—780 nm) with a spectral sampling width of 0.5—2.0 nm, and the High Resolution Fluorescence Imaging Spectrometer (FLORIS HR) with a sampling width of 0.1 nm in the two oxygen bands (677—697 nm and 740—780 nm). As explained in paragraph 1.6.2, the SIF emis-

sion is sensitive to irradiation and VPD, both of which show a clear diurnal pattern, which translates into a SIF diurnal pattern. This diurnal effect is entrenched in the physiological origins of the SIF emissions. Therefore, satellite overpass time is an essential element of a SIF retrieval. FLEX/Sentinel-3 overpass time will be 10:00 local solar time, corresponding to the maximal SIF emission over the diurnal cycle (Drusch et al., 2017). Given the diurnal pattern in the SIF emission, there is also a growing interest in using geostationary missions for SIF retrievals (Chang et al., 2021). Currently, the Geostationary Ocean Color Imager (GOCI) provides multiple SIF images a day over the Korean Peninsula (Gupana et al., 2021). On April 7th 2023, the National Aeronautics and Space Administration (NASA) launched the Tropospheric Emissions: Monitoring of Pollution (TEMPO; Zoogman et al., 2017) satellite, which is providing multiple SIF images over the contiguous United States. ESA is launching the Sentinel-4 aboard the Meteosat Third Generation-Sounder (MTG-S) next year. This mission should provide multiple SIF observations a day over Europe. In light of the upcoming geostationary and FLEX missions, it is important to go and understand the behaviour of the SIF signal in the context of increasing stresses. This knowledge will then allow for a physiologically consistent interpretation of SIF. Table 1.1 provides an overview of all operational and upcoming SIF capable satellite sensors.

Table 1.1: Overview operational and upcoming SIF-capable spaceborne sensors (adapted from: Jonard et al., 2020).

Platform	Sensor	Observation period	Spatial resolution (km)	Spectral resolution (nm)	SIF fitting window (nm)
ERS-2	GOME	July 1995 - June 2003	30 x 320	0.4	595-793
EnviSat	SCIAMACHY	Mar. 2002 - Apr. 2012	60 x 30	0.48	595-812
MetOp-A/B/C	GOME-2	Jan. 2007 - present	40 x 80	0.5	593-790
GOSAT	TANSO-FTS	Jan. 2009 - present	82, circular	0.025	758-775
GOSAT-2	TANSO-FTS-2	Oct. 2019 - present	10.5 circular		
GOCI	GOCI	Jun. 2010 - present	0.5x0.5	10	660-680
OCO-2	OCO-2	Sept. 2014 - present	1.3 x 2.5	0.042	757-775
Sentinel-5P	TROPOMI	Oct. 2017 - present	7 x 7	0.5	675-775
TanSat	ACGS	Feb. 2018 - present	2 x 3	0.044	758-778
ISS	OCO-3	Mar. 2019 - present	1.6 x 2.2	0.05	540-740
TEMPO	TEMPO	Apr. 2023 - present	4 x 5	0.6	757-772
MTG-S	Sentinel-4	2024	8 x 8	0.12	757-772
FLEX	FLORIS LR/HR	2025	0.3 x 0.3	0.5-2 (LR) 0.1 (HR)	500-780 (LR) 759-769 (HR)

1.7.4 Missing knowledge for a consistent interpretation of remotely sensed SIF

Porcar-Castell et al. (2021) lies out a roadmap for a consistent interpretation of fluorescence across scales. These seven obstacles are: (i) calculating the partition of the absorbed light between the different pigments, (ii) unravel the distribution of energy between PSI and PSII, (iii) calculate the energy partitioning photosynthesis - NPQ - fluorescence at the level of PSII, (iv) estimate the effect of downstream alternative energy sinks (e.g, the Mehler reaction in the water-water cycle), (v) calculate scattering of fluorescent light over the canopy, (vi) correct for atmospheric scattering and absorption and (vii) integrating SIF controls over space and time. To solve these issues, they stress the need for research making an odyssey from photosystem drought reactions all the way up to the ecosystem drought reaction. This thesis is a part of this oddysey, proposing solutions for (iii) and (vii), while also touching (ii) and (v). The thesis pays particular attention to a drought situation.

1.8 Objectives and general outline of the thesis

To bridge the gap between the photosystem and global scale, the thesis studies the behavior of sun-induced chlorophyll fluorescence through a combination of fluorescence measurements at the leaf, canopy, and global levels. Various plant models are used to quantitatively link the SIF data to plant variables. The overall goal of bridging the gap between the photosystem and global scales is split into three research questions, that each deal with the specificities of their scale. Each thesis objective builds upon the findings of the previous.

- What is the sensitivity of the plant-scale SIF emission to drought conditions?
- How can the sensitivity of SIF to drought conditions be used for improving a crop growth model?
- Can SIF be used to detect drought stress at the landscape to the global scale?

Each chapter of this thesis is tailored to each research question. The first research question, answered in Chapter 2, lays out the foundations for the two other chapters. In this sense, Chapter 2 forms a stepping stone between the physiological scale and the plant scale. It manages to identify the key processes explaining the SIF drought reaction. Chapter 3 pours this link into concrete by mechanistically connecting the stress reaction at the photosystem level to the SIF emission based on a plot scale experiment and by incorporating the stress reaction in a crop growth model. In Chapter 4, the knowledge of the mechanisms driving the SIF drought reaction is catapulted from the plot to the global scale. This thesis is of special interest in light of the upcoming satellite missions that have capabilities for measuring SIF, especially the FLEX mission, the first satellite designated for global SIF retrieval.

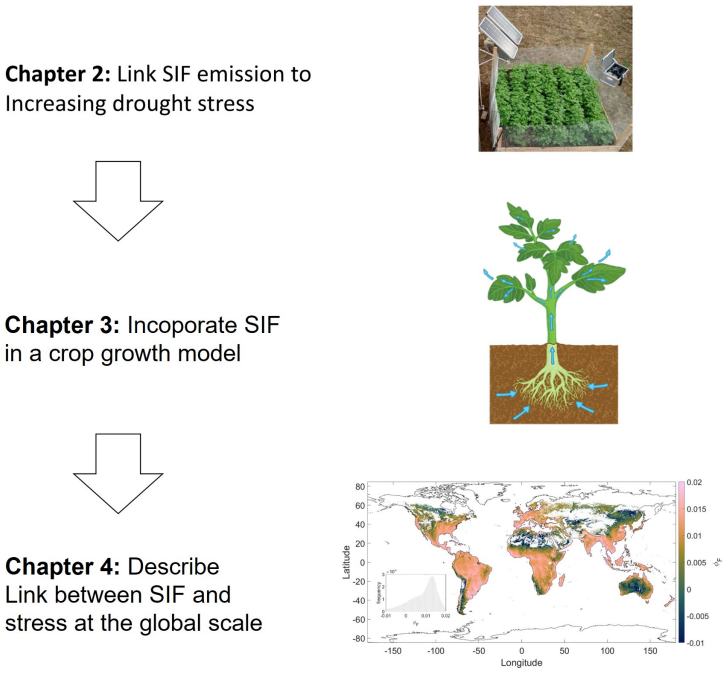


Figure 1.6: Link between the different chapters of the thesis.

Chapter 2

Observed effect of drought on SIF at the canopy scale

This chapter is based on the following article:

De Cannière, S., Vereecken, H., Defourny, P., Jonard, F. (2022). Remote Sensing of Instantaneous Drought Stress at Canopy Level Using Sun-Induced Chlorophyll Fluorescence and Canopy Reflectance, In Remote Sensing, volume 14, page 2642.

Abstract

Climate change amplifies the intensity and occurrence of dry periods leading to drought stress in vegetation. For monitoring vegetation stresses, sun-induced chlorophyll fluorescence (SIF) observations are a potential game-changer, as the SIF emission is mechanistically coupled to photosynthetic activity. Yet, the benefit of SIF for drought stress monitoring is not yet understood. This study analyses the impact of drought stress on canopy-scale SIF emission and surface reflectance over a lettuce and mustard stand with continuous field spectrometer measurements. Here, the SIF measurements are linked to the plant's photosynthetic efficiency, whereas the surface reflectance can be used to monitor the canopy structure. The mustard canopy showed a reduction in the biochemical component of its SIF emission (the fluorescence emission efficiency at 760 nm —ϵ_{760}) as a reaction to drought stress, whereas its structural component (the Fluorescence Correction Vegetation Index—FCVI) barely showed a reaction. The lettuce canopy showed both an increase in the variability of its surface reflectance at a sub-daily scale and a decrease in ϵ_{760} during a drought stress event. These reactions occurred simultaneously, suggesting that sun-induced chlorophyll fluorescence and reflectance-based indices sensitive to the canopy structure provide complementary information. The intensity of these reactions depend on both the soil water availability and the atmospheric water demand. This study highlights the potential for SIF from the upcoming FLuorescence EXplorer (FLEX) satellite to provide a unique insight into the plant's water status. At the same time, data on the canopy reflectance with a sub-daily temporal resolution are a promising additional stress indicator for certain species.

2.1 Introduction

Over the last 50 years, remote sensing has proven its value for large-scale drought stress monitoring. Classically, remote sensing monitors the greenness of the vegetation. A game changer in stress monitoring has been the introduction of sun-induced chlorophyll fluorescence (SIF), a remote sensing signal sensitive to the photosynthetic activity of a plant (Mohammed et al., 2019). Photosynthesis is particularly sensitive to drought conditions; since these induce stomatal closure to reduce the CO_2 uptake, the energy demand by the dark reactions is lowered. As a result, there is a need for an alternative energy sink, which is provided for by a series of reactions, collectively known as non-photochemical quenching (NPQ), which increases when the CO_2 uptake lowers. This, in response, also alters the SIF emission (Jonard et al., 2020). Through the stomata that are still open, plants lose water and therefore show a decrease in their turgor pressure (Petruzzellis et al., 2019). This leads to changes in the leaf angle (Briglia et al., 2020), changing the canopy reflectance, especially in the near-infrared (Kautsky and Hirsch, 1931). This makes high-temporal resolution observations of near-infrared reflectance another promising indicator for instantaneous stress monitoring.
Since its discovery (Kautsky and Hirsch, 1931), chlorophyll fluorescence has proven its value for monitoring of photosynthetic activity, mostly through the form of pulse-amplitude modulation (PAM; Murchie and Lawson, 2013). Here, a leaf is illuminated with artificial light pulses, stimulating its chlorophyll molecules, after which they send out fluorescent light as a reaction. This reaction informs about the stress status. Specifically, stress lowers the actual PSII efficiency (YII), as the demand for energy in the photosynthetic electron transport chain lowers. As an alternative energy sink, NPQ increases. The increase in NPQ and decrease in Y(II) have a downstream effect on the emission of the steady-state fluorescence emission (Fs/F0). The latter variable describes the emission of fluorescence by a chlorophyll molecule under high light (e.g., sunlit) conditions. Fs/F0 is conceptually similar to SIF, which is the steady-state emission of chlorophyll fluorescence measured by a spectrometer and uses the sun as the illumination source. A drought-induced decrease in Fs/F0 has been observed over various species (Flexas et al., 2002).

SIF provides a fluorescence signal from the leaf to the ecosystem scale. Since SIF only comprises 1—3% of the absorbed energy, its retrieval is limited to solar and atmospheric absorption lines (Porcar-Castell et al., 2014). Canopy-scale SIF is typically retrieved at the O_2-A and O_2-B Telluric bands, situated at 760 nm and 687 nm, respectively. Their corresponding SIF observations are referred to as SIFA and SIFB. Canopy-scale SIF is expected to show a wavelength-specific behaviour. First, the relative contribution of photosystem I (PSI) to the SIF emission is more important for SIFA compared to SIFB. Second, 687 nm is within the absorption spectrum of chlorophyll, causing SIFB to be prone to reabsorption by another chlorophyll molecule. This is not the case with SIFA. Third, the re-emitted photon is scattered around in the canopy. By its nature, scattering is wavelength-specific behaviour (Porcar-Castell et al., 2021). Another hyperspectral remote sensing vegetation index that is linked to photosynthetic activity is the photochemical reflectance index (PRI; Gamon et al., 1992), which is inversely correlated to the NPQ. Therefore, SIF and PRI are expected to provide similar, yet complementary information on the plant's photosynthetic activity.

Over the plant kingdom, plants possess a wide arsenal of drought survival strategies. These strategies break down into two broad categories, isohydric and anisohydric, which exist alongside each other on a spectrum (Konings and Gentine, 2017). Isohydric plants tend to have a risk-avoidant strategy, closing their stomata immediately in cases of a water shortage. This leads to reduced growth in case of drought stress. The anisohydric strategy is a higher-risk strategy, in which a plant keeps its stomata open, maintaining its growth rate while suffering high water losses through transpiration (Sade et al., 2012), thereby showing larger variations in turgor pressure (Konings and Gentine, 2017). Plants following a more anisohydric strategy are expected to show a fierce reaction in their canopy structure compared to more isohydric plants.

Because of its mechanistic link to photosynthesis, canopy-scale SIF is typically linearly linked to ecosystem-scale photosynthesis, quantified by the Gross Primary Productivity (GPP; Wieneke et al., 2016; Yang et al., 2018a), but the link between SIF and GPP is less straightforward in cases of drought stress. A field-scale SIF-GPP relationship could be finetuned during drought periods using PRI data (Ma et al., 2022). Field-scale studies have pointed out drought stress at both the structural and biochemical level (Xu et al., 2021). Both stress-induced

changes in the leaf biochemistry and in the canopy structure affect both SIFA and SIFB (Wieneke et al., 2018). Due to the sensitivity of the biochemical component to drought stress, SIF proved to be an interesting input for a crop growth model (De Cannière et al., 2021).
This study describes the reaction of SIFA and SIFB to increasing drought stress conditions by monitoring the SIF emission and canopy reflectance of a yellow mustard (Sinapsis alba) and a common lettuce (Lactuca sativa) canopy continuously over their growing season, and thus capturing a variety of stress conditions. In addition, the near-infrared reflectance is monitored to estimate short-term variations in canopy structure. Yellow mustard and common lettuce differ greatly in their degree of isohydricity, in which the mustard is more isohydric than the lettuce. We expect the lettuce to show a more expressed structural reaction because it tends to lose more turgor pressure given its anisohydric nature. The mustard's more isohydric nature should force its stomata to close more quickly, and thereby causing a reaction at the level of the leaf physiology.

2.2 Materials and methods

2.2.1 Site description and experimental design

The experiment took place at the remote sensing field test facility of Forschungszentrum Jülich in Selhausen (Niederzier, Germany). Two 2 by 2 metre wooden boxes were built with a soil depth of 40 cm (Figures 2.1 and 2.2). The boxes were filled with the soil from the site, containing 13% sand, 70% silt and 17% clay, according to the USDA textural classification (United States Department of Agriculture, 1987). The soil was placed on top of a gravel layer, with geotextile separating the silty loam from the gravel layer. This setup allows standing water to drain away, limiting its water storage capacity. Gravel and stones were removed from the soil. A tripod with a hyperspectral instrument (Fluorescence box—FloX) was placed in between the boxes. The tripod was installed in such a way that the spectrometer could pivot between the boxes. During the vegetation development phase, identical irrigation schemes were applied to both boxes. After the leaf development phase, the boxes were subject to different irrigation regimes, causing one box to become significantly dryer compared to the other. By default, the

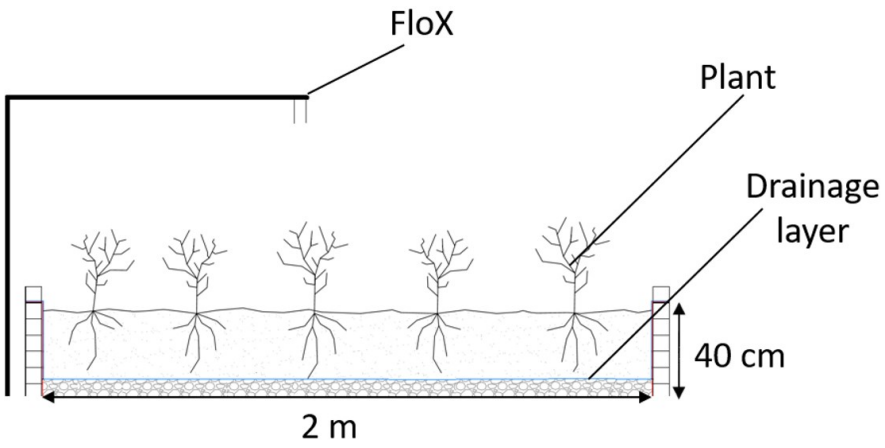


Figure 2.1: Schematic overview of the box design.

FloX instrument was installed to measure the dry box. During specific days, the cross-arm on the tripod was turned for the FloX to measure over the reference box.

The test facility was located next to the Integrated Carbon Observatory System (ICOS) and TERENO (Terrestrial Environmental Observatories) test site at Selhausen, from which data on air humidity and air temperature were used. Soil moisture, soil temperature and soil water potential (matric potential) were monitored in the plant boxes themselves. Table 2.1 gives an overview of the sensors used. The soil water availability was estimated by means of the soil water potential, expressed in pressure heads (h). These were converted to a pF value (Eq. 2.1). Soil moisture and soil water potential provide complementary information. Soil moisture is more commonly used in modelling of the hydrological cycle as it is easier to measure at large scale (Vereecken et al., 2016), whereas soil water potential corresponds more closely to the water the plant can extract from the soil (Robbins and Dinneny, 2018).



Figure 2.2: Picture of the boxes during the mustard experiment.

Table 2.1: Overview of equipment used during the measurement campaigns.

Variable	**Symbol**	**Unit**	**Instrument**
Air Temperature	T_{AIR}	°C	HPM45C, Vaisala Inc., Helsinki, Finland
Air Humidity	RH	%	HPM45C, Vaisala Inc., Helsinki, Finland
Vapour pressure deficit	VPD	kPa	HPM45C, Vaisala Inc., Helsinki, Finland
Precipitation	Prec	mm	Thies Clima tipping bucket, Ecotech, Bonn, Germany
Photosynthetically active radiation	PAR	Wm^{-2}	FloX, JB Hyperspectral Düsseldorf, Germany
Soil moisture	SM	cm^3cm^{-3}	5TE, Meter Environment, München, Germany
Soil water potential	SWP	kPa	Teros-21, Meter Environment, München, Germany

$$pF = -\log(h) \tag{2.1}$$

Two measurement campaigns were conducted. The mustard was sown on May 29th (DOY 149), 2021 and harvested on August 2nd (DOY 214), 2021. The lettuce was planted (not sown) on August 7th (DOY 219), 2021 and harvested on September 22nd (DOY 265), 2021.

2.2.2 Leaf-scale measurements of photosynthesis

In order to link the SIF signal to photosynthesis, leaf-scale active chlorophyll fluorescence measurements were taken with the portable PAM 2500 chlorophyll fluorimeter (Heinz Walz GmbH, Effentrich, Germany), to gain information on the efficiency of the PSII (Y(II)) and on the steady-state fluorescence (Fs/F0). Pulse-amplitude modulation (PAM) measurements were taken on sunny days, preferably, and multiple measurements were taken throughout the day.

2.2.3 Processing of Field Spectrometer Data

The SIF data were taken using a Fluorescence Box (FloX; JB hyperspectral, Düsseldorf, Germany), which combines two field spectrometers, retrieving in both the O_2-A and O_2-B band, respectively, and situated at 760 and 687 nm using the improve Fraunhofer Depth Line method (iFLD; Alonso et al., 2008). The spectrometers have a spectral sampling rate of 0.17 nm and 0.65 nm, respectively. Their respective spectral resolutions are 0.3 nm and 1.5 nm. The iFLD method compares the up- and downwelling radiances inside the oxygen absorption bands to the radiance just outside the absorption bands, resulting in an estimate for the SIFA and SIFB fluorescence (Julitta et al., 2016). In addition to the fluorescence, the FloX measures the hyperspectral surface reflectance in the region of 400—900 nm. The FloX spectrometer took data from 7 AM until 7 PM UTC+1 with a temporal resolution of one minute. Outliers in the fluorescence data, diverging more than 3 standard deviations from the daily mean, were removed. Then, both the fluorescence, irradiance and reflectance data were averaged to a temporal resolution of 30 min, reducing the noise in the time series.

2.2.4 Monitoring Leaf Biochemistry with Field Spectrometer Data

The canopy-scale SIF is not merely the sum of the SIF emissions of the individual leaves. Instead, considering the canopy scattering and reabsorption is vital when moving from leaf-level to canopy-level SIF, the behaviour of scattering and reabsorption are wavelength-specific. Consequently, SIF at a certain wavelength λ observed in a certain direction ω ($SIF_{\lambda,\omega}$) is affected by two wavelength-specific probabilities; the fluorescence emission efficiency ϵ_λ and the photon' s escape probability $f_{esc,\lambda,\omega}$ (Eq. 2.3). Both $f_{esc,\lambda,\omega}$ and ϵ_λ are expected to be reactive to water availability. This study aims at describing these two factors and their relation to drought stress.

$$SIF_{\lambda,\omega} = PAR \cdot fPAR \cdot \epsilon_\lambda \cdot f_{esc,\lambda,\omega} \tag{2.2}$$

Isolating ϵ_λ from the Eq. 2.3 allows extracting the biochemical information from the spectrometer-based $SIF_{\lambda,\omega}$. Yang et al. (2020) developed the Fluorescence Correction Vegetation Index (FCVI; Eq. 2.3), which is a reflectance-based surrogate factor for the canopy absorption and canopy scattering. This index is formulated as the difference between the near-infrared reflectance R_{NIR} between 767 and 773 nm and the broadband visible reflectance R_{VIS} between 400 and 700 nm, assuming that the reflectance observations are taken from the same direction as the SIF measurements. This approach is only valid in the absence of any reabsorption, which is why it is only meaningful for SIFA.

$$FCVI = R_{NIR} - R_{VIS} \approx f_{esc,760} \cdot fPAR \tag{2.3}$$

The biochemistry can be assessed with three variables: fluorescence emission efficiency at 760 nm (ϵ_{760}: Eq. 2.4), the SIFB yield (SIFBY: Eq. 2.5) and the photochemical reflectance index (PRI: Eq. 2.6). The ϵ_{760} contains the SIFA normalized by the PAR and FCVI and integrated over a hemispherical space. The PRI is a reflectance-based, narrow-band vegetation index, related to the de-epoxidation of xanthophyll, which is linked to the NPQ. A more negative PRI should indicate a higher NPQ (Gamon et al., 1992), and therefore a higher stress level. Similar to SIF, PRI is affected by a biochemical and a structural component (Wong and Gamon, 2015). The epoxidation of xanthophyll causes only

a change in very limited parts of the absorption spectrum, which is why a bandwidth of 2 nm is chosen in Eq. 2.6.

$$\epsilon_{760} = \frac{\pi \cdot \mathrm{SIFA}}{\mathrm{FCVI} \cdot \mathrm{PAR}} \tag{2.4}$$

$$\mathrm{SIFBY} = \frac{\mathrm{SIF}_{687}}{\mathrm{PAR}} \tag{2.5}$$

$$\mathrm{PRI} = \frac{R_{531} - R_{570}}{R_{531} + R_{570}} \tag{2.6}$$

To assess the sensitivity to PAR of the leaf biochemistry, the daily correlation coefficient ρ was calculated. To do so, the Pearson's correlation coefficient between the ϵ_{760} and SIBY was used on one hand, and, on the other hand, PAR was calculated for each day individually, resulting in a daily correlation coefficient. The daily correlation coefficient only considered data taken between 9 AM and 3 PM, since light-limited photosynthesis is expected in early morning or late afternoon, due to the lower solar irradiations at these times of the day.

2.2.5 Monitoring canopy structure with field spectrometer data

The canopy structure was monitored by means of the FCVI. Canopy structure contains two elements: the leaf area index (LAI), which depends on the plant's phenology, and the leaf angle. The leaf angle is subject to sub-daily changes. A large variation in leaf angle is expected to translate into a large diurnal variation in FCVI. Trends in the FCVI are linked to changes in LAI due to vegetation growth.

2.3 Results

2.3.1 Description of meteorological conditions during growing season

The mustard grew mainly in June and July 2021. The growing season had a precipitation of 101.7 mm and a mean temperature of 18.34° C. The mustard reached its adult phase in July, a month with a mean temperature of 17.9°C. On July 16th 2021 (DOY 197), the experiment was struck by unusual amounts of rainfall, so much so that the equipment could not keep up with the precipitation. However, the high rainfall

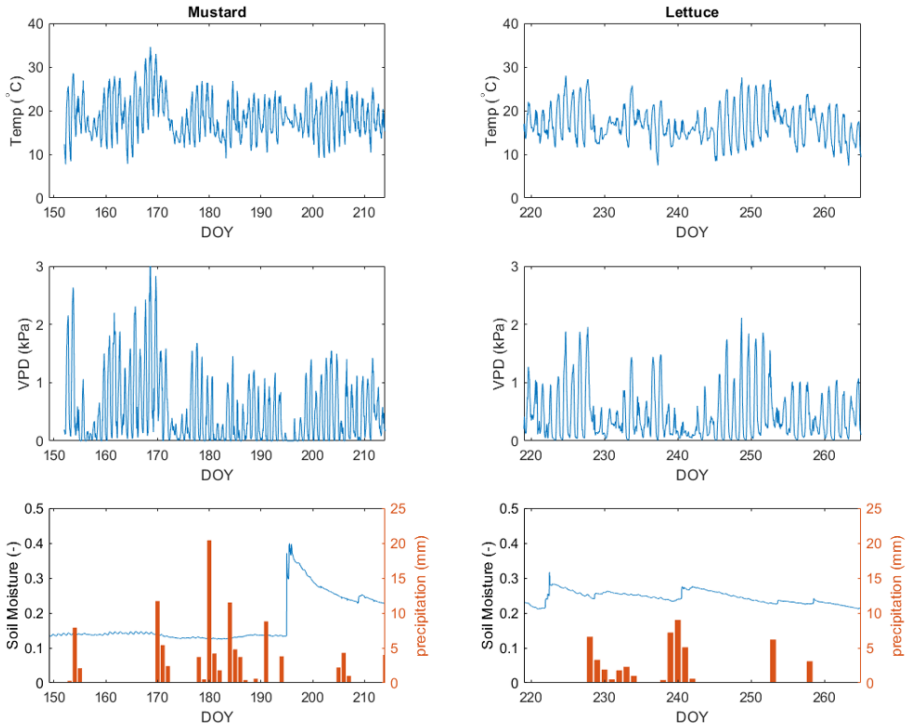


Figure 2.3: Description of the meteorological conditions during the growing season for mustard and lettuce.

explains the sharp peak in soil moisture on that day. The period after, between DOY 198 and DOY 205, showed a clear decrease in soil moisture. The lettuce experiment took place in the late summer, with both lower precipitations (49.3 mm) and lower temperatures (16.9° C), compared to the mustard experiment (Figure 2.3). During the 2021 lettuce experiment, more irrigation was applied to the reference box. These irrigation events resulted in slight increases in soil water content.

2.3.2 Canopy Structure and SIF Emission at Sub-Daily Scale

To illustrate the behaviour of the biochemical variables ϵ_{760} and PRI, as well as the behaviour of the structural variable FCVI at the diurnal

level, two days of the lettuce experiment and two days of the mustard experiment are plotted (Figure 2.4). These days had very different weather and soil conditions, corresponding to low and high water stress. In the lettuce dataset, the PRI remained constant over the unstressed day, whereas the ϵ_{760} showed a bell-shaped pattern. For the stressed day, the shape of the ϵ_{760} reverses to a valley shape. A similar valley-shaped pattern is visible for the PRI on that day. The biochemistry-related variables ϵ_{760} or PRI to stress between the lettuce and the mustard plant show a similar behaviour; both turn into a valley-like shape during the stressed period. The FCVI does however show a different reaction between the two species. Whereas the lettuce FCVI shows a bell shape during stressed days over the lettuce canopy, the mustard FCVI barely shows any sensitivity to stress.

2.3.3 Reaction of structural and physiological variables to increasing stress

In addition to the changes in the diurnal behavior, the daily mean value of the mustard biochemical variables changes in function of the stress intensity (Figure 2.5). This research considers a plant stressed if it suffers from both low soil water availability and high atmospheric demand. Between DOY 201 and DOY 209, the plants experienced drought stress, through a combination of high PAR, VPD and pF values. The period between DOY 201 and 209 shows a decrease in ϵ_{760}, compared to the period between DOY 196 and DOY 202. After DOY 209, the ϵ_{760} increased to its pre-stress levels. Like the ϵ_{760}, the PRI showed a decrease between DOY 201 and DOY 204. At DOY 205, corresponding to a cloudy, colder day, the PRI jumped back up. This reaction was not observed with the ϵ_{760}. It is interesting to note that dry soil (i.e., high pF values), combined with low VPD and PAR values, does not induce a decrease in ϵ_{760}, as seen in DOY 212 and DOY 213. During the mustard experiment, the FCVI hovered around 0.27 and showed little same-day variation. Unlike SIFA, SIFB shows very little reactivity to water limitation. Consequently, SIFA and SIFB are further apart during stressed days compared to unstressed days.

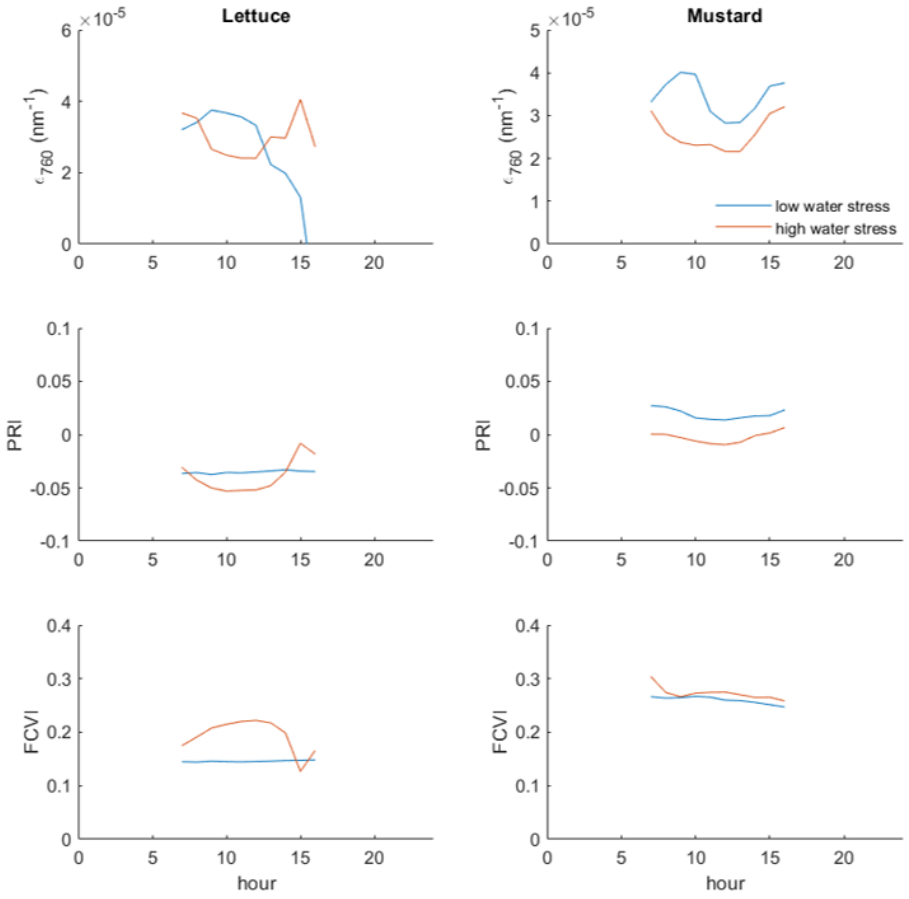


Figure 2.4: Behavior of ϵ_{760}, PRI and FCVI for three days during the lettuce experiment. For the lettuce dataset, DOY 244 was the unstressed day (blue line), DOY 247 the stressed one (red line). For the mustard dataset, DOY 198 was the unstressed day (blue line), DOY 202 the stressed one (red line). The water stress conditions are indicated by the soil water potential.

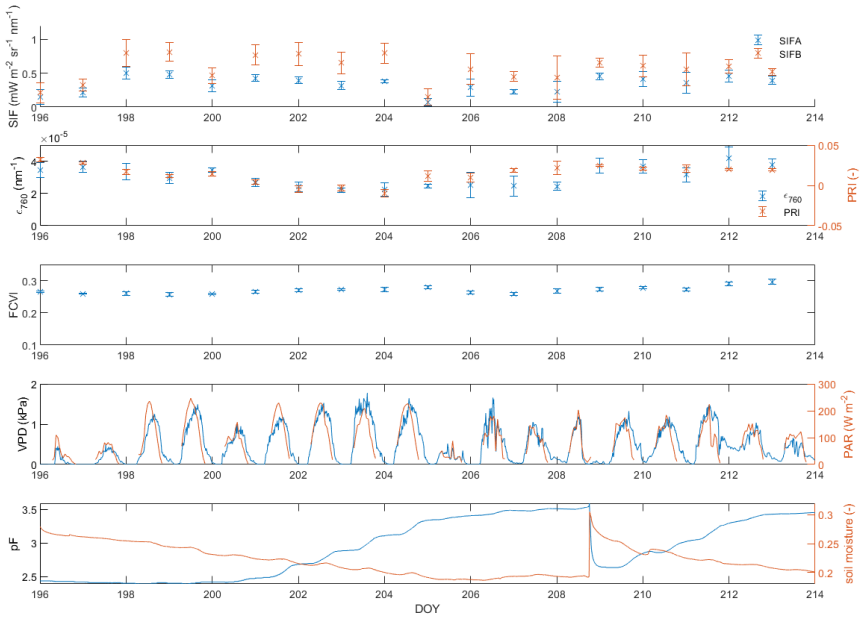


Figure 2.5: Evolution of SIFA, SIFB, FCVI, ϵ_{760} and PRI for the 2021 mustard campaign. The drought conditions are given by the VPD, PAR, soil water potential and soil moisture.

In the lettuce dataset, both the PRI and FCVI showed an upward trend during the growing season, explained by vegetation growth. The ϵ_{760} did not show such trend. Similar to the observations of the mustard dataset, lettuce physiological variables (ϵ_{760}, PRI) also show a decrease during drought events (Figure 2.6), albeit not as expressed as with the mustard dataset. The decreased values of ϵ_{760} were found between DOY 246 and DOY 251. During that same period, the PRI showed a slight decrease, before retaking its upward trend. Interestingly, the standard deviation of FCVI increased in days with high VPD, indicating that the lettuce plant shows major drought-induced, short-term variability in its canopy structure. The increased daily standard deviation in FCVI is prevalent in the period between 245 and 251, and it decreases in the days after. The mustard FCVI (Figure 2.5) did not show such behaviour.

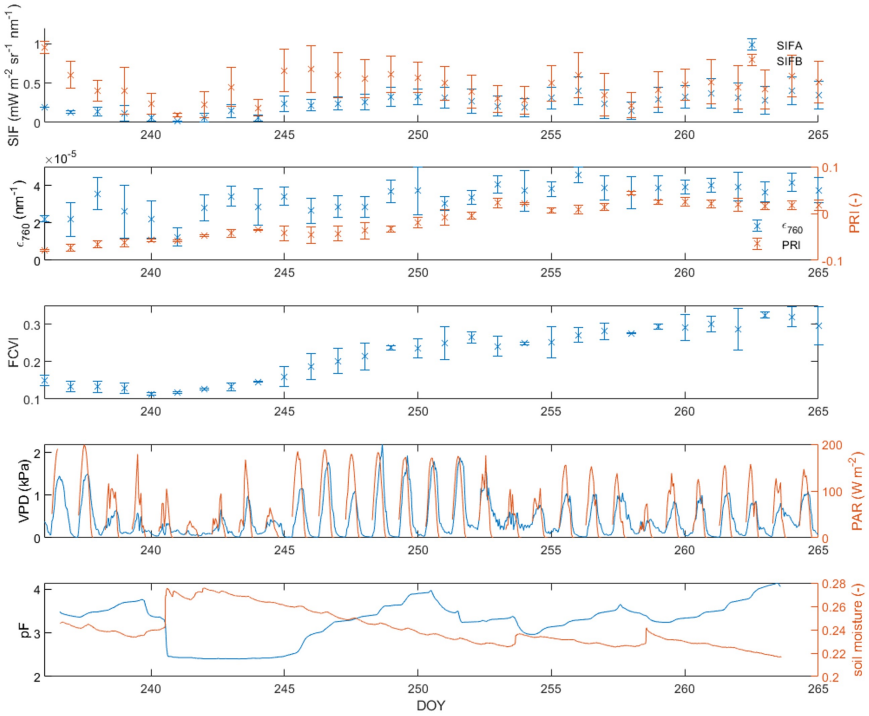


Figure 2.6: Evolution of SIFA, SIFB, FCVI, ϵ_{760} and PRI for the 2021 lettuce campaign. The drought conditions are given by the VPD, PAR, soil water potential and soil moisture.

2.3.4 Relationship between SIF and APAR

Similar to light response curves used in photosynthesis research (e.g., Herrmann et al., 2019), the SIF-PAR curves were fitted with the Michaelis—Menten function (Eq. 2.7), in which the parameters SIF_{max} and K_m are fitting parameters. This equation suggests that an increase in PAR leads to an increase in SIF emission, up until a certain degree of saturation. The ϵ_{760}-PAR curve was fitted using a second-order polynomial function with the mustard reaching its maximum at PAR = 90 W/m^2 and lettuce reaching its maximum at PAR = 97 W/m^2. The lettuce ϵ_{760}-PAR plot is more curved compared to its mustard counterpart (Figure 2.7). The SIFA-PAR curve for the lettuce shows a lot more scatter compared to its counterpart over the mustard canopy. The SIFB-PAR plots show a near-linear relationship. There is little difference in the SIFB-PAR plots between the two crops. The lower R^2 values for the SIFA-PAR compared to the SIFB-PAR plots suggest that there is more non-PAR-related information in the SIFA compared to the SIFB.

$$SIF = \frac{SIF_{max} \cdot PAR}{K_m + PAR} \tag{2.7}$$

2.3.5 Response of ϵ_{760} to different light intensities under light- and water limitation

Figure 2.8 shows the daily correlation coefficient between PAR and two SIF-related variables: ϵ_{760} and SIFBY for both the lettuce and mustard datasets. They each show a different behavior. The daily ρ between ϵ_{760} and PAR show a high, positive ρ on days with clear light-limitation values (e.g., between DOY 196 or DOY 245). This correlation switches to an anti-correlation in the case of water limitation, as seen between DOY 198 and DOY 205 for the mustard dataset and between DOY 246 and DOY 251 for the lettuce dataset. This negative ρ is quick to switch to a positive ρ on days with a lower VPD, or on days with a lower pF value. Examples are the increased ρ between DOY 206 and DOY 215 for the mustard dataset and between DOY 252 and DOY 260 for the lettuce dataset. The correlation between SIFBY and PAR remained between 0.5 and 1 for almost the entire growing season for both crops. A decrease in the SIFBY-PAR correlation is found between DOY 199 and

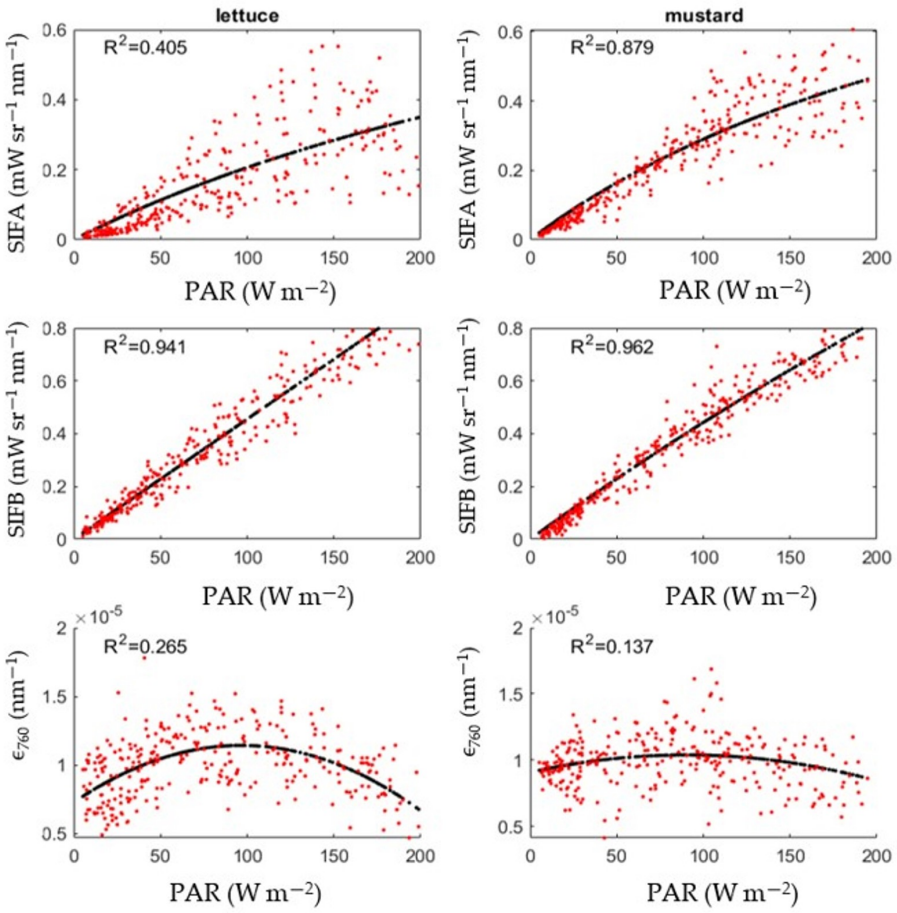


Figure 2.7: Fitted (black dots) and observed (red dots) values of SIFA, SIFB and ϵ_{760}.

DOY 205 for the mustard dataset, which corresponds to days with intense water limitation. The period between DOY 205 and DOY 209 still has a low soil water availability, but the period is cloudier, lowering the PAR and therefore putting the plant in a light-limited regime for large parts of the day. The anti-correlation between PAR and ϵ_{760} is the most expressed on DOY 203 and DOY 204, corresponding to the days with the highest pF values. Similarly, a drop in the ρ between SIFBY and

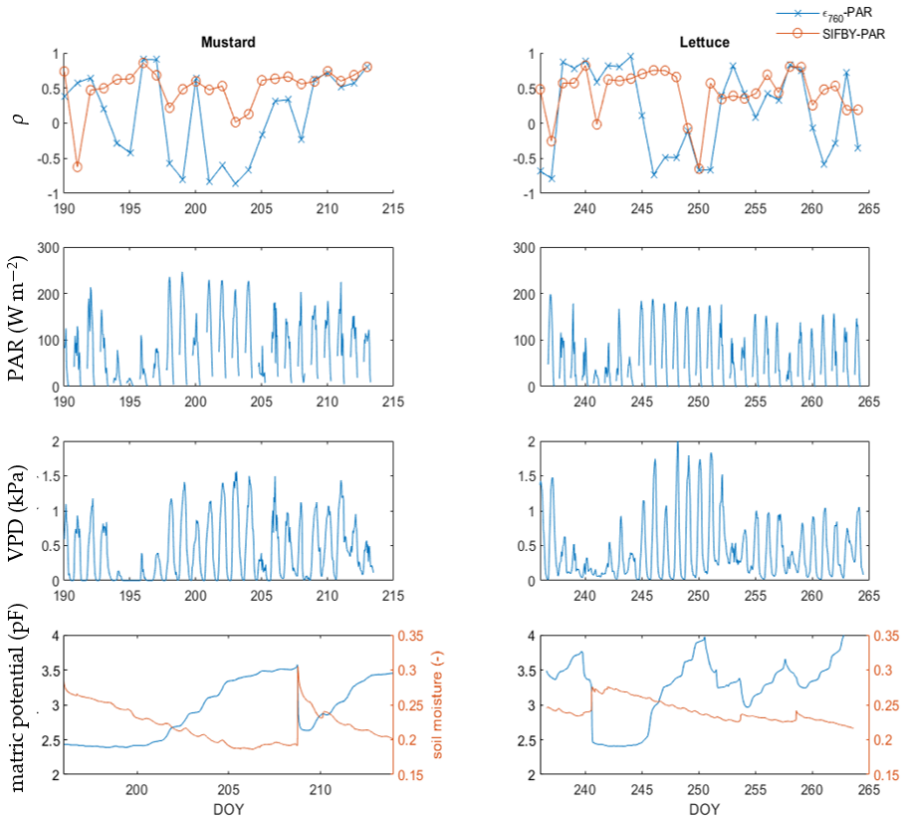


Figure 2.8: Daily correlation coefficient of ϵ_{760}, SIFBY and FCVI to PAR for the mustard and lettuce experiments during their adult phase.

PAR is found on DOY 250 and DOY 251 for the lettuce dataset, corresponding to two days with a clear water limitation.

2.3.6 Linking PAM and FloX measurements

Figure 2.9 shows a series of PAM measurements, taken on DOY 264 and DOY 271 during the lettuce experiment. DOY 264 was a sunnier day, with a more expressed water limitation. Two PAM parameters that were put special emphasis on were steady-state fluorescence Fs/F0, linked to the SIF, and the PSII effective quantum yield Y(II), linked to the PRI. The PAM data showed large variability, expressed by

their standard deviation. This large variability is linked to changes in photosynthetic activity at the leaf level, due to differences in illumination conditions, for example. During both DOY 264 and DOY 271, PRI and Y(II) followed a similar pattern, with their minimal values around between 11h and 14h. Linking Fs/F0 values to ϵ_{760} values is harder due to the large standard deviation of the Fs/F0 measurements. Both the Fs/F0 and ϵ_{760} values did not change significantly during either DOY 264 or DOY 271. The FloX measurements of ϵ_{760} between the stress box and the reference box did not differ significantly for DOY 264 and DOY 271. The PRI was significantly higher in the reference box on DOY 264, indicating higher stress conditions in the stressed box compared to the reference box.

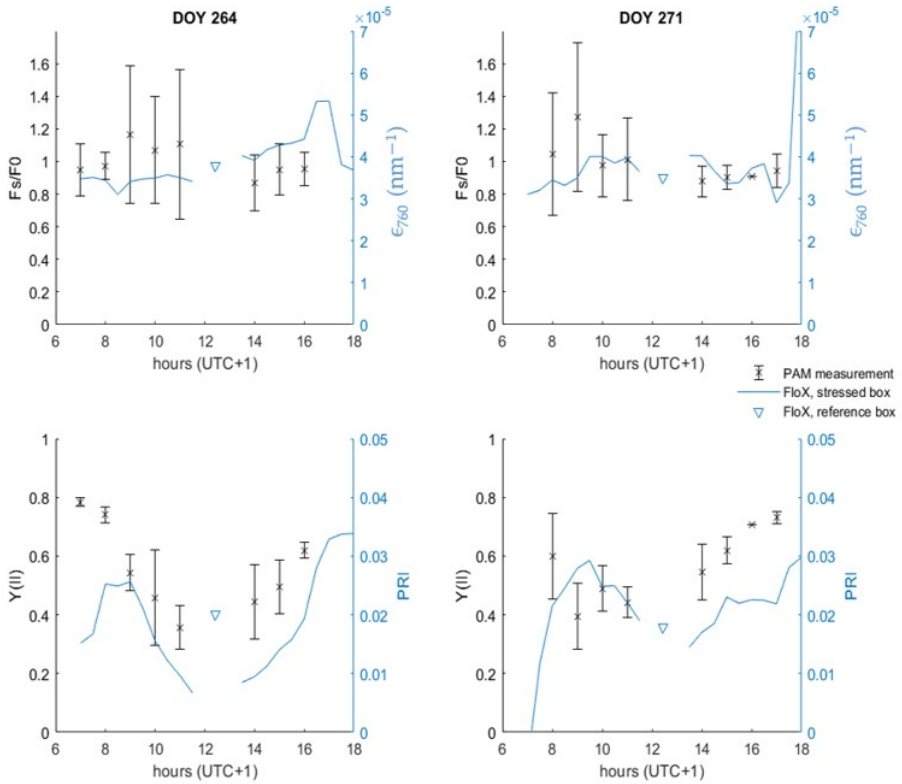


Figure 2.9: Behaviour of the PAM-based variables Fs/F0 and Y(II) as well as two FloX-based variables, ϵ_{760} and PRI for DOY 264 and DOY 271 during the lettuce experiment. Each PAM data point is an average of 10 measurements. The PAM measurements were taken in the stressed box.

2.4 Discussion

2.4.1 Relative timing of plant structural and physiological reactions

In both the lettuce and mustard datasets, the ϵ_{760} reacted without delay to changes in light or water limitation (Figure 2.8). The decrease in ϵ_{760} was more expressed during the mustard experiment compared to the lettuce experiment. The lettuce, however, showed a simultaneous reaction in both its biochemical variable ϵ_{760} and in its structural

variable, FCVI. A possible explanation for the different behaviour between the two crops lies in the difference in their degree of isohydricity. Because of the loose stomatal regulation by the lettuce plant (Eriksen et al., 2020), it is expected to lose its turgor more quickly compared to mustard. These variations in turgor induce a change in the leaf angle (Deckmyn et al., 2000). Field studies have observed that these changes occur before any irreversible damage occurs, through necrosis, for example (Nguyen et al., 2019). Near-infrared reflectance is therefore a promising early water stress indicator. A sub-daily temporal resolution is recommended here since the changes in turgor pressure typically show a clear diurnal pattern (Javaux and Carminati, 2021). Mustard's more isohydric stomatal regulation could explain its little diurnal FCVI variability. This suggests that the short-term changes in canopy structure are mainly useful as a stress indicator over anisohydric plants. Given the shallow box depth, the plants are forced to root at a shallow depth, eliminating the possibility of deep rooting. This might cause real-world systems to react slower compared to this semi-artificial structure.

2.4.2 Plant physiological interpretation of ϵ_{760} and PRI behaviour

PAM-based studies have observed a decrease in steady-state fluorescence (Fs/F0) under high-light conditions with increasing light saturation (Magney et al., 2017; van der Tol et al., 2014), similar to the decrease in ϵ_{760} for high PAR values in Figure 2.7. Similarly, other PAM studies have observed the same parameter in case of in the case of water stress combined with high-light conditions, with a minimum around noon (Wohlfahrt et al., 2018). This behaviour is similar to the anticorrelations between ϵ_{760} and PAR shown in Figure 2.8. These findings confirm that ϵ_{760} can be conceptualized as a canopy-averaged variant of fluorescence yield (ϕ_F). The large standard deviations in Figure 2.9 point out that there is a large variability in leaf-scale Fs. Interpreting SIFB in physiological terms is harder compared to SIFA because SIFB structural and biochemical components cannot be separated. The light response curves in Figure 2.7 report a clear difference in light response between SIFA and SIFB; the SIFB seems to adhere to its linear relationship with PAR, even under high-light and low-water conditions, whereas SIFA emissions seem to saturate. Whereas various sources

have observed some sort of decrease in SIFA during drought stress (Xu et al., 2021; Wieneke et al., 2018; De Cannière et al., 2021; Ač et al., 2015), studies linking SIFB to drought stress have been inconclusive, with some reporting an increase (Wieneke et al., 2018) and others a decrease (Xu et al., 2021). Leaf-scale studies report a decrease in SIFB emission in the case of a drought stress (Jonard et al., 2022). Figure 2.8 suggests that SIBY becomes anti-correlated with PAR, similar to ϵ_{760}, albeit only in more severe stress conditions.

2.4.3 Use of SIF as a water stress monitoring tool

Because of its mechanistic link to the photosynthetic apparatus, ϵ_{760} is reactive to ambient stress conditions, being a combination of the soil water availability, the VPD and the PAR. These conditions change during the day. At dawn, when PAR approximates 0, a plant grows in a light-limited regime, regardless of its soil water status. Assuming cloud-free conditions, PAR and VPD follow a bell-shaped pattern, and the plant will switch to a water-limited regime once the PAR and VPD reach a certain level. The point at which this happens depends on the plant water status, and, therefore, also on the soil moisture as well as on the plant isohydricity. Figures 2.5—2.7 have shown that more intense water limitation results in a more expressed decrease in ϵ_{760}, making it an indicator for the instantaneous stress conditions. This makes ϵ_{760} an especially interesting indicator in the light of the upcoming FLuorescence EXplorer (FLEX), as it will provide global maps of ϵ_{760} with a spatial resolution of 300 m. Global-scale SIF from the TROPOMI sensor has already proven its value to classify ecosystems as water- or light-limited (Garbulsky et al., 2011). The drought-induced decrease in ϵ_{760} is expected to allow monitoring the intensity of the water limitation.

2.4.4 Use of PRI as a stress indicator

Figure 2.9 shows that the PRI neatly follows the same diurnal behaviour as Y(II), which is, by definition, inversely related to NPQ, making it a biochemical indicator that is complementary to SIF. When using PRI, it is important to consider that PRI bears both structural and biochemical information. Unlike to SIFA, there is no corrective vegetation index to separate the biochemical and structural components

of PRI. This makes the interpretation of PRI in physiological terms less straightforward. Still, PRI time series revealed some stressed periods, as PRI did not adhere to its upward trend during this period. Using high-temporal resolution data of PRI, several methods using detrending techniques exist to remove the structural effect from the PRI measurement (Kohzuma et al., 2021; Kovác et al., 2022). The differences in the stress reaction between PRI and SIFA indicate that both variables are sensitive to different parts of the photosynthetic apparatus. This suggests that they provide complementary information on the plant's photosynthesis. The combination of ecosystem-scale PRI and SIFA has already proven its value for photosynthesis estimations (Kovác et al., 2022).

2.4.5 Complementarity of structural and physiological information

Water losses through transpiration might result in a drop in turgor pressure. This induces changes in the leaf configuration, affecting the f_{esc} and fPAR. The plant's isohydricity determines whether it will rather drop its turgor pressure or slow down its photosynthesis (Roman et al., 2015). The drop in turgor pressure and the structural changes associated with it take place at the diurnal timescale (Junttila et al., 2021), which is why diurnal observations of the FCVI (or any other structure indicator) are necessary in order to link canopy structure to drought stress. As, the ϵ_{760} is only sensitive to the biochemical component of SIF emission, FCVI and ϵ_{760} provide independent, yet complementary information on the instantaneous stress conditions. It is interesting to note that detecting the structural reaction requires less strict requirements regarding spectral resolution compared to SIF observations, but measuring the full diurnal cycle of FCVI is needed to link it to leaf angle and water stress changes. Because of the absence of full diurnal measurements, satellite-based SIF might be more reactive than satellite-based vegetation indices (Cao et al., 2021), despite the structural and biochemical reaction taking place simultaneously. It is worth noting that water limitation also impedes vegetation growth, lowering its green biomass, which, in turn, affects various remote sensing metrics, including the NIR reflectance, and thus the FCVI. Short- and long-term variations in FCVI, therefore, represent other processes. The combined long- and short-term dynamics, affecting FCVI are visible on

Figure 2.6; the upward trend in FCVI represents the growth of the lettuce plant, whereas the diurnal variations in FCVI are due to changes in the leaf angle.

2.5 Summary and outlook

This study describes the reaction of the sun-induced chlorophyll fluorescence (SIF) emission and the canopy reflectance to increasing water limitation for both a mustard and a lettuce stand during a field experiment that lasted their entire growing seasons. The SIFA emission was decomposed into a biochemical component, being the fluorescence emission efficiency (ϵ_{760}) and a structural component, the Fluorescence Correction Vegetation Index (FCVI). Such an operation was not done for SIFB. In addition, the photochemical reflectance index (PRI) was monitored. Both plants showed a biochemical reaction to increasing stress, most notably in the fluorescence emission efficiency (ϵ_{760}). The reaction of ϵ_{760} to increasing stress was observed in two ways. First, ϵ_{760} decreases according to the stress intensity. Second, ϵ_{760} and PAR show an anticorrelation under water-limited days and a positive correlation under light-limited days. Under intensely stressed days, SIFBY and PAR also showed an anti-correlation. Given the more isohydric nature of the mustard plant, it showed a clearer biochemical reaction compared to the lettuce. In addition to the biochemical reaction, the lettuce also showed a change in its canopy structure. The structural reaction is visible through diurnal variations in the FCVI. This behaviour was not observed for the mustard FCVI. Given the anisohydric nature of the lettuce plant, it was expected to show more variations in its turgor pressure compared to the mustard. This is consistent with the large diurnal variation in leaf angle by the lettuce canopy. Complementary to the SIF, PRI (photochemical reflectance index) decreases in the case of stress. Affected by both plant development and leaf biochemistry, a high temporal resolution of PRI measurements is needed to unravel the leaf biochemistry and plant development effects. The findings in this study contribute to the monitoring of plant water status. Whereas this study explains the reaction of the leaf biochemistry and the canopy structure at the local scale, the same logic can be applied at a larger scale. The structural reaction (FCVI) is a valuable stress indicator if the seasonal and daily dynamics in the canopy can be disentangled. The

seasonal dynamics are influenced by vegetation growth, whereas the short-term dynamics are related to changes in leaf angle, which are influenced by the turgor pressure. The biochemical reaction is a decrease in ϵ_{760} during periods of low soil water availability and high water demand and is especially interesting information for the FLuorescence EXplorer (FLEX) mission. The photochemical reflectance index (PRI) provides additional information on the plantś biochemistry, but its dependency on the canopy structure hampers a clean interpretation of PRI in terms of leaf biochemistry. Future studies could elaborate on the effect of drought on SIF emission with plants that are allowed to root in real-field conditions. Secondly, making more repetitions of the same drought conditions might give an idea on the variability of the drought reaction. Thirdly, repeating this experiment with a C4 plant provides information on the generalizability of the findings along the plant kingdom. To cover a wide range of meteorological conditions, using plants with a relatively long growing season might be recommended.

Chapter 3

Constraining a crop growth model with SIF data

This chapter is based on the following article:

De Cannière, S., Herbst, M., Vereecken, H., Defourny, P., Jonard, F. (2021). Constraining water limitation of photosynthesis in a crop growth model with sun-induced chlorophyll fluorescence, in: Remote Sensing of Environment, volume 267, Page 112722.

Abstract

Water fulfils key roles in maintaining a plant's biological activity. Water shortage induces stomatal closure, causing a reduction in photosynthesis and transpiration rates. Sun-induced chlorophyll fluorescence (SIF) emission is sensitive to subtle, stress-induced variations in non-photochemical quenching and in photosynthetic electron transport, caused by e.g., a fluctuation in the water availability. Based on this sensitivity, a framework for calibrating a water stress function in a crop growth model using ground-based SIF observations is proposed. SIF time series are simulated by coupling the AgroC crop growth model to the Soil Canopy Observations Photosynthesis Energy (SCOPE) model. This allowed parametrizing the water stress function in the AgroC crop growth model, resulting in improved estimates of actual evapotranspiration and net ecosystem exchange over a sugar beet stand during stressed periods. The improvement in the estimation of the water and carbon fluxes by AgroC during the summer months highlights the ability of canopy scale SIF observations to serve as a remote sensing metric to indicate the intensity of a stress condition. We argue that our framework, linking SIF emission to stress functions, can be used to extract information concerning drought stress from the Fluorescence Explorer (FLEX) satellite, scheduled for launch in 2025.

3.1 Introduction

Croplands play a vital role in the global food supply. Over the last five decades, two thirds of global cropland was affected from drought-induced crop yield losses (Heino et al., 2018). Crop models are suitable tools for assessing the impact of drought stress on the future crop yield (Kumar, 2016). Remote sensing datasets are valuable for informing crop growth models, as they allow the collection of data about the vegetation status over large spatial and temporal scales. Thermal, optical and microwave data have shown their added value in the context of crop growth modeling (Ghazaryan et al., 2020).

The capacity of a plant to assimilate CO_2 through photosynthesis in light-abundant conditions is expressed by the maximum carboxylation capacity (VCMax). Stress reduces VCMax through a series of regulatory mechanisms (Zhou et al., 2014), causing the CO_2 assimilation in the dark reactions to slow down, forcing the light reactions to slow down with it, since an excess of light energy in the photosynthetic apparatus leads to oxidative stress. Through non-photochemical quenching (NPQ), a plant can dissipate the excess amount of light energy that is absorbed by a chlorophyll molecule as heat. As a third process, in parallel with heat dissipation and photosynthesis, the absorbed photon can be re-emitted by a chlorophyll molecule (Ač et al., 2015). The latter process is referred to as chlorophyll fluorescence. Chlorophyll fluorescence has a specific emission spectrum between 650 nm and 800 nm, with emission peaks at 685 nm and 740 nm. Sun-induced chlorophyll fluorescence (SIF, i.e., the emission of chlorophyll fluorescence induced by the sun) corresponds to 1-3% of the absorbed radiation (Porcar-Castell et al., 2014). SIF occurs under natural conditions and it is observable through proximal and spaceborne remote sensing. As it deals with only a limited amount of emitted energy, the retrieval of sun-induced chlorophyll fluorescence (SIF) is restricted to the solar and atmospheric absorption lines. Two main atmospheric absorption lines are linked to the absorption of atmospheric oxygen at 760 and 687 nm. These lines are referred to as the O_2-A and O_2-B band respectively. Named after their respective oxygen absorption band, SIF emission retrieved in these lines is referred to as SIFA and SIFB. ESA's FLuorescence EXplorer (FLEX) satellite mission, scheduled for launch in 2025,

will measure SIF in these bands (Drusch et al., 2017). Given the narrow bandwidth of these atmospheric absorption lines, a sub-nanometer spectral resolution is imperative to reliably measure SIF emission, both at the plot and at the satellite scale. The requirements to measure SIF emission in the O_2-B band are even stricter compared to the O_2-A band, the former needing a spectral resolution below 0.5 nm (Julitta et al., 2016). Because of its less strict requirements concerning the spectral resolution, the behavior of field-observed SIFA in the context of stress is better described in the literature (Jonard et al., 2020).

Based on the mechanistic link between SIF emission and carbon assimilation, SIF is an interesting input to carbon uptake models, as it can serve as a constraint to photosynthetic activity, both at the local and at the global scale (Damm et al., 2010). SIF observations from already operational satellite missions have been used to constrain carbon uptake models at the global scale (Parazoo et al., 2014). Lee et al. (2015) expanded the community land model (CLM) with a SIF module based on van der Tol et al. (2014) and using the NPQ model from Lee et al. (2013). By implementing the photosynthesis and SIF modules from the Soil Canopy Observations Photosynthesis Energy (SCOPE) model into the Biosphere Energy Transfer HYdrology (BETHY) model, Norton et al. (2018) reduced the uncertainty in the model's gross primary productivity (GPP) estimates. Qiu et al. (2018) constrained evapotranspiration (ET), SIF, and GPP simulations in the Simplified Simple Biosphere Model 2.0 (SSiB2) land surface model using soil moisture observations from the Soil Moisture Ocean Salinity (SMOS) satellite, to adapt the soil hydraulic parameters and the wilting point.

The link between photosynthetic activity, SIF emission and soil water content has also been investigated at the local scale. A crucial variable in linking SIF emission to photosynthesis is VCMax. However, most studies only focused on one part of this link. Camino et al. (2019) retrieved VCMax based on airborne SIF measurements. They noted a correlation between soil moisture and VCMax in case of drought stress. Bayat et al. (2019) established a link between the soil water content and the GPP, by scaling the VCMax using a water stress factor, defined as a function of the soil water content. Wieneke et al. (2018) noted a reduction in SIFA emission in case of drought stress. Because of the link between stomatal closure and the reduction in the transpiration

rate, Maes et al. (2020) observed a connection between SIF emission and transpiration.

To interpret a spectrometer-observed value of SIF in a meaningful way, it is important to realize that the SIF signal is affected by many factors. The main driver of SIF is the absorbed photosynthetically active radiation (APAR) (Yang et al., 2018b; Jonard et al., 2020). Along with the biochemical effects that affect the SIF emission, it is also affected by canopy radiative transfer including scattering and reabsorption processes that are determined by leaf properties and the 3D structure of the canopy (Yang and van der Tol, 2018; Pacheco-Labrador et al., 2019), which is, in turn, affected by the turgor pressure and thus by the plant water status (Parkash and Singh, 2020). As the SCOPE model considers these leaf and canopy processes, it is particularly well adapted to mechanistically link SIF emission to photosynthesis (Celesti et al., 2018).

At the local scale, the AgroC (Herbst et al., 2008) crop growth model describes the development of a certain crop type during an entire growing season. Previous studies have used the model to predict the field-scale (NEE) (Klosterhalfen et al., 2017), and simulate within-field variability of LAI (Brogi et al., 2020; Herbst et al., 2021). AgroC contains an aboveground module, describing the photosynthesis and the leaf and canopy development as well as a belowground module describing the root water uptake. In order to run properly, AgroC requires detailed information concerning the plant properties. Remote sensing is a suitable tool for providing such information to crop growth models since it allows for the retrieval of plant properties over large areas. Recently, there has been a special interest is around the use of SIF to parametrize crop growth models, since SIF provides direct information from the photosynthetic apparatus, allowing to constrain the photosynthetic module in a crop growth model (Huang et al., 2019). Informing a crop growth model with SIF is therefore expected to lead to a better parametrization of VCMax. The latter quantifies the carboxylation rate, which happens at the end of the photosynthesis, and which decreases in case of a drought.

Given the crucial role of drought on VCMax in modeling photosynthesis and SIF emission, we aim at better estimating VCMax from SIF observations exploiting the sensitivity of VCMax to root zone water availability. Unlike to other studies, this study does not seek to improve the parametrization of the maximum carboxylation capacity under reference conditions (VCMax,25). Instead, the sensitivity of VCMax to drought stress forms the backbone of this study. Specifically, a better estimation of the drought stress conditions is supposed to improve the estimate of VCMax and therefore to lead to a better estimate of the photosynthetic activity. A water stress function quantifies the stress conditions at a given soil matric potential or soil water content. While water stress functions have proven their value in crop growth modeling, it is hard to characterize these functions for real field conditions. Since the parameterization of the water stress function quantifies the stress-induced reduction in VCMax, the sensitivity of the SIF emission to the parametrization of the water stress function is expected. AgroC uses the root water uptake model of Feddes et al. (1974) to define a water stress function. This function considers a region of soil water potential causing drought stress and a range of soil water potentials indicating waterlogging, with an optimal range of root water uptake in between. This study establishes a framework for parametrizing a water stress function in a crop growth model using SIF observations. An improvement in the estimated carbon and water fluxes is expected when calibrating the Feddes function using SIF observations.

3.2 Materials and methods

3.2.1 Site description

This study was performed over a sugar beet stand in Merzenhausen (50°52'14''N, 6°26'59''E), Germany at 93 m above sea level. The region has a maritime influenced climate with annual precipitation of 698 mm and an annual mean temperature of 9.9°C in 2019 (Klosterhalfen et al., 2017). The soil is classified with a silt loam texture according to the USDA classification. The site is a part of the German Terrestrial Environmental Observatories (TERENO) initiative, an Earth observation network across Germany (Bogena et al., 2016). An eddy covariance (EC) at two meter high and a meteorological station provide data on

atmospheric CO_2 and H_2O concentration (c_a and c_{H_2O}, respectively), 3D wind components, air temperature (T_{air}), air humidity (RH) and the global radiation (Rad_{glob}) (table 3.1). Based on this, the Net Ecosystem Exchange (NEE) and latent heat flux (λE) are calculated. Soil water content (SWC) and soil temperature T_{soil} at different depths (5, 10, 20 and 50 cm) were also measured with in-situ sensors (table 3.1). A detailed description of the site and the TERENO infrastructures is given in Bogena et al. (2016). The processing and quality assessment were done with the standardized TERENO strategy (Mauder et al., 2013) for EC data. The sugar beets were sown on April 24th (DOY 114) and they were harvested on November 14th (DOY 316).

Table 3.1: Description of the TERENO infrastructure in Merzenhausen.

Variable	**Symbol**	**Unit**	**Instrument**
Atmospheric CO_2 concentration	c_a	mmol CO_2 m^{-3}	LI7500, LI-COR Inc, Lincoln, USA
Atmospheric H_2O concentration	c_{H_2O}	mmol H_2O m^{-3}	LI7500, LI-COR Inc, Lincoln, USA
Wind speed	WS	m s^{-1}	Campbell Scientific, Inc. Logan, USA
Wind direction	WD	deg	Campbell Scientific, Inc. Logan, USA
Soil Water Content	SWC	cm^3 cm^{-3}	Hydraprobe, Steven Water Monitoring Inc., Portland, USA
Soil Temperature	T_{soil}	$°C$	Hydraprobe, Steven Water Monitoring Inc., Portland, USA
Global radiation	Rad_{glob}	W m^{-2}	CMP3, Kipp & Zonen, Delft, The Netherlands
Precipitation	Prec	mm	Thies Clima tipping bucket, Ecotech, Bonn, Germany
Air Pressure	P_{air}	hPa	WXT521, Vaisala Inc., Helsinki, Finland
Air Temperature	T_{air}	°C	HMP45C, Vaisala Inc., Helsinki, Finland
Relative Air Humidity	RH	%	HMP45C, Vaisala Inc., Helsinki, Finland

3.2.2 Canopy-scale observations of SIF

Measurement description

SIF was measured with the Fluorescence Box (FloX) field spectrometer (JB hyperspectral devices, Düsseldorf, Germany), commonly used in field-based SIF studies (Wohlfahrt et al., 2018; Yang et al., 2020). The FloX combines information from two spectrometers (QE Pro, Ocean Optics, USA), both designed to measure the upwelling as well as the downwelling radiation. The first spectrometer (spectrometer 1) focusses on the fluorescence spectrum (i.e., the red and near-infrared zone), while the second (spectrometer 2) focusses on the visible and near-infrared regions (table 3.2). Considering the spectral range, the spectrometer 2 also provides measurements of the incoming Photosynthetically Active Radiation (PAR, 400-700 nm). The spectrometers were fixed at a height of 4 m, providing a footprint of 2.4 m^2 (Figure 3.1). SIF was retrieved in the oxygen absorption lines at 760 nm (SIFA) with the improved Fraunhofer Line Depth (iFLD; Alonso et al., 2008) method. This method is based on the classical Fraunhofer Line Depth method, comparing the up-and downwelling radiances inside the oxygen absorption band (760 nm) and outside the absorption band (750 nm). In addition, a correction factor based on the reflectance is added to better separate the contributions of the reflected radiance and the fluorescence on the measured signal (Julitta et al., 2016; Mohammed et al., 2019). While the combination of SIFA and SIFB has been used to assess drought conditions (Wieneke et al., 2016) or GPP (Campbell et al., 2019), notable mismatches have been found when predicting SIFB based on photosynthetic activity (Wohlfahrt et al., 2018). Consequently, this study's focus is limited to SIFA.

Interpretation of canopy-scale SIFA

Unlike to the canopy-scale GPP, which is the sum of the carbon uptake of all the leaves, the canopy-scale SIFA is not merely the sum of the SIF emitted by the individual leaves. Therefore, obtaining the physiological component of SIF is obtained by use of the FCVI, identical to paragraph 2.2.4.

To minimize crop phenology effects on the SIF signal, we only took FloX measurements between August 1st (DOY 213) and August 23th,



Figure 3.1: Picture of the FloX, measuring SIF and hyperspectral reflectance over the test site.

2019 (DOY 235). During this period, the vegetation was fully developed. FloX measures the SIF emission with a temporal resolution of ~ 1 min. Outliers, defined as data that diverged more than 3 standard deviations from the seasonal mean, were removed. The data were averaged to hourly averages between 10 AM and 2 PM UTC. This period was chosen to remove effects induced by variation in solar zenith angle. The FloX turned off when the solar panel-powered battery could not keep up with the power demand by the device and its cooling system. This reduced the size of the SIF observations dataset to 10 non-constetutive days.

Table 3.2: Characteristics of the spectrometers in the Fluorescence Box.

	Spectrometer 1	**Spectrometer 2**
Spectral range	650-800 nm	400-950 nm
Spectral sampling	0.17 nm	0.65 nm
Spectral resolution	0.3 nm	1.5 nm
Field of view downwelling Rad	180°	180°
Field of view upwelling Rad	25°	25°

3.2.3 Description of the AgroC-SCOPE model

Modeling carbon fluxes in AgroC

AgroC (version 1.0; Herbst et al., 2008; Klosterhalfen et al., 2017) is a 1D crop growth model consisting of three modules: the crop growth module SUCROS (Spitters et al., 1988), the soil water, heat, and CO_2 flux module SOILCO2 (Simunek and Suarez, 1993) as well as the soil carbon turnover module RothC (Jenkinson and Coleman, 2008). AgroC requires: meteorological forcing variables as well as plant-related parameters and soil-related parameters. The soil- and plant-related parameters are field- and crop-specific, but time-invariant. These were taken from Klosterhalfen et al. (2017), which ran AgroC for sugar beets over the same test field. The meteorological input variables (air temperature, soil surface temperature, precipitation, solar radiation, and potential grass reference evapotranspiration) were aggregated to a temporal resolution of 1 hour. Potential grass evapotranspiration was calculated using the FAO guidelines (Allen et al., 1998). As output, AgroC simulates both the aboveground and belowground plant growth and carbon fluxes, which are the sum of the GPP, the aboveground respiration (Res_{ABG}) and the belowground respiration (Res_{BG}). These fluxes are balanced to calculate the Net Ecosystem Exchange (NEE; Eq. 3.1). The latter corresponds to the variable that is measured by EC towers. We, therefore, evaluated the capacity of AgroC to model carbon fluxes using the NEE.

$$NEE = GPP + Res_{ABG} + Res_{BG} \tag{3.1}$$

Photosynthesis is described with the Farquhar et al. (1980) model, incorporated into the SUCROS part of the AgroC model. This mech-

anistic model considers three internally limiting factors on photosynthesis, being the light absorption, water availability and the rubisco concentration (see appendix for a detailled description of the Farquhar model). A key variable in this model is the maximum carboxylation rate (VCMax), which is affected by a water stress factor ($\overline{\alpha}$), the maximum carboxylation capacity in reference conditions (VCMax,25) and an air temperature correction factor ($f(T_{\text{air}})$) (Eq. 3.2). The latter formula does not consider photorespiration.

$$\text{VCMax} = \overline{\alpha} \cdot \text{VCMax,25} \cdot f(T_{\text{air}}) \tag{3.2}$$

Modeling water fluxes in AgroC

Belowground, AgroC models the terms of the soil water balance: soil water storage change, actual evapotranspiration, infiltration by solving the Richard's equations (Herbst et al., 2008) with an hourly resolution. To do so, AgroC makes use of two input variables: the precipitation and grass reference evapotranspiration (ET0). Based on the precipitation, the amount of interception (Int) was calculated and the amount of infiltration was calculated, which then supplied the soil water content. Based on the crop coefficient K_c, which is a plant-specific literature value describing the plant transpiration in each stage of its growing season, and on the LAI, the ET0 was split into a potential evaporation (EP) and transpiration (TP) component (Eq. 3.3 & 3.4).

$$\text{EP} = \text{ET0} \cdot K_c \cdot e^{-0.6 \cdot \text{LAI}} \tag{3.3}$$

$$\text{TP} = \text{ET0} \cdot K_c - \text{EP} - \text{Int} \tag{3.4}$$

Potential transpiration is then scaled with the depth-specific stress factor α to reduce the depth-specific root water uptake once the potential evapotranspiration exceeds the water availability. To form the actual transpiration TA, TP is scaled with the average stress factor $\overline{\alpha}$. The belowground water flow and the root water uptake in the soil are characterized in the SOILCO2 module through the site-specific soil hydraulic parameters (van Genuchten parameters), the bulk density and the porosity. These parameters are assigned to each vertical node in the soil profile, allowing the soil water content, water flow and root water

uptake to be calculated for each node. For the experimental field in Merzenhausen, Klosterhalfen et al. (2017) calibrated the soil hydraulic parameters.

Use of SCOPE to model SIF emission

The Soil Canopy Observations Photosynthesis Energy (SCOPE; van der Tol et al., 2009) is an integrated model of soil-canopy spectral radiances, photosynthesis, fluorescence, temperature, and energy balance. This approach allows to model both the physiological and structural aspects of SIF emission. Both AgroC and SCOPE allow the use of the Farquhar et al. (1980) model to describe photosynthesis. In the latter model, stress conditions can be considered by lowering the carboxylation capacity VCMax, which forms the connection between the AgroC and SCOPE models. The leaf reflectance and canopy scattering are affected by the plant properties, which are estimated based on reflectance time series. Given the mechanistic link between SIF emission, photosynthesis, and stress conditions, this study aims for estimating stress conditions based on SIF observations and use this information to inform the water stress model implemented in AgroC.

3.2.4 Quantifying drought stress in AgroC

Thanks to its description of the entire root profile, AgroC is remarkably well-suited for drought stress-related modelling. The belowground and aboveground modules of AgroC are connected through root water uptake, which is linked to the soil water status. Actual root water uptake is calculated by scaling the potential root water uptake with the depth-specific water stress factor α, calculated for each node in the soil profile. To do so, the module uses the Feddes function (Feddes et al., 1974), which requires information on the soil water status (expressed in pressure head h) and four threshold values h_1 to h_4, defining three zones, as visualized in Figure 3.2. Each zone has its relationship be-

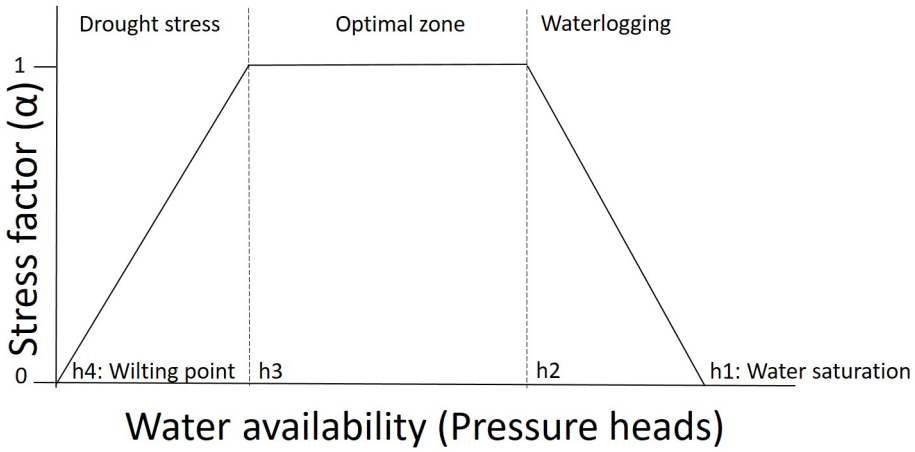


Figure 3.2: Stress factor α in function of water availability with the Feddes function.

tween water availability and water stress (Eq. 3.5).

$$\alpha(h) = \begin{cases} \dfrac{h_1 - h}{h_1 - h_2} & h_1 > h > h_2 \\ 1 \quad \text{for} & h_2 \geq h \geq h_3 \\ \dfrac{h_3 - h}{h_3 - h_4} & h_3 > h > h_4 \end{cases} \tag{3.5}$$

The position of h_4 and h_1 are universal at the wilting point (-15 000 cm) and the water saturation (0 cm) point respectively. The values of h_2 (field capacity) and h_3 (drought onset) are a function of the plant and soil properties and have therefore to be calibrated for each site individually. Affecting both the duration and the intensity of the stress, knowing the exact position of h_3 is crucial for correctly linking drought stress to soil water availability. The four Feddes parameters are considered constant over the entire root profile and the entire growing season. Applying the Feddes function to each node in the soil profile results in a distribution of α along the root zone. The averaged value of the reduction factor along the depth profile becomes the water stress

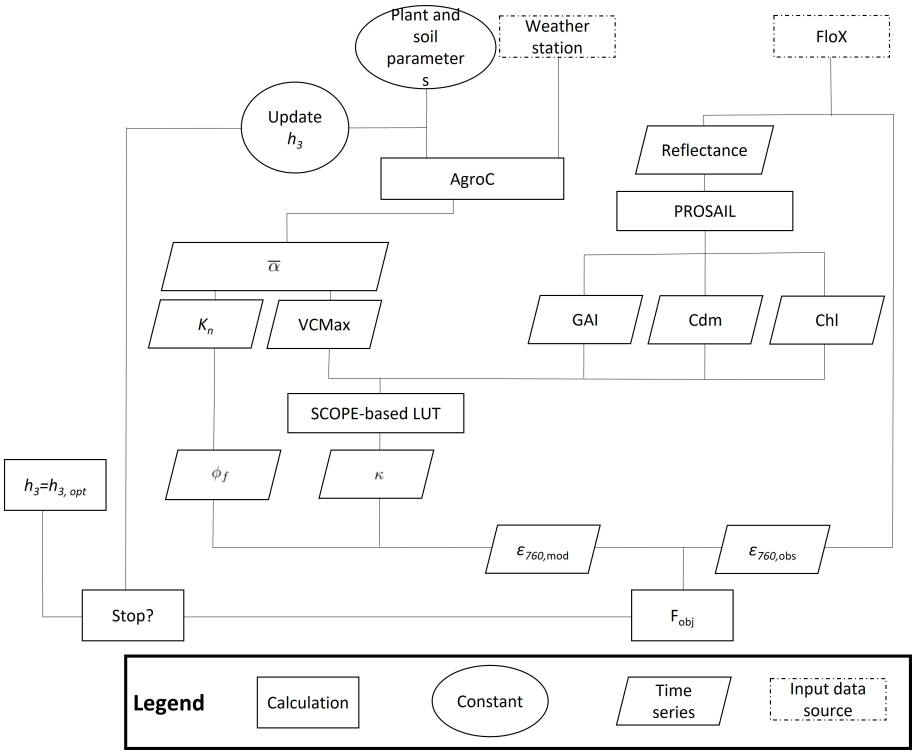


Figure 3.3: Visualization of the optimization approach.

factor $\overline{\alpha}$, serving as a correction factor for VCMax,25 to calculate VCMax (Eq. 3.2). Based on the sugar beet measurements of (Vilfan et al., 2019), VCMax,25 was set to 100 μmol CO_2 m^{-2} s^{-1}. We expect to see a connection between ϵ_{760} and h_3 as $\overline{\alpha}$ affects the value of VCMax and the rate of non-photochemical quenching K_n (explained in paragraph 3.2.5; Figure 3.3). This connection should enable ϵ_{760} data to serve as a metric of the drought stress conditions. This information allows calibrating the value of h_3, which affects both the onset of a drought as well as the intensity of ongoing drought conditions. As waterlogging conditions are not met during this study, h_2 is kept constant at -50 cm. Figure 3.3 visualizes the workflow of the calibration of h_3 based on the ϵ_{760} observations. Each paragraph in the sections 3.2.5-3.2.8 explains one step of this workflow.

3.2.5 Connecting fluorescence emission with photosynthesis in AgroC

AgroC models the photosynthesis with the Farquhar et al. (1980) model, which calculates the photosynthesis along with the photosynthetic yield (ϕ_p), being the ratio of electrons participating in photosynthesis (J_p) with the absorbed photosynthetically active radiation (APAR) (Eq. 3.6).

$$\phi_p = \frac{J_p}{\text{APAR}} \tag{3.6}$$

From the ϕ_p, the light saturation (x) is calculated, in which the maximum photosynthetic yield ϕ_{p0} is set to 0.8 by default, corresponding to the $Fv/Fm(=\phi_0)$ value for undamaged PSII:

$$x = 1 - \frac{\phi_p}{\phi_{p0}} \tag{3.7}$$

The light saturation is used to calculate the NPQ component. To establish the link between x and NPQ, we make use of a formalism called the rate constants (Butler, 1978), denoted here with K_n, K_p, K_d and K_f for the non-photochemical, photochemical, thermal decay and fluorescence components, respectively. The difference between K_n and K_d is that K_n reprsents regulated thermal dissipation, while K_d represents non-regulated, temperature-dependent, thermal decay. The difference between these two variables is rather mathematical than physiological. The fluorescence and thermal decay have default values being $K_f = 0.05$ and $K_d = \max(0.03 \cdot T_{\text{air}} + 0.0773, 0.87)$ (Lee et al., 2015). As proposed by van der Tol et al. (2014), K_n is calculated based on x and on three fitting parameters γ, β and K_{n0} (Eq. 3.8-3.9).

$$\nu = \frac{(1+\beta)x^\gamma}{\beta + x^\gamma} \tag{3.8}$$

$$K_n = \nu . K_{n0} \tag{3.9}$$

van der Tol et al. (2014) proposes two sets of fitting parameters to link K_n to x, depending on the plant water status, leading to calculation of $K_{n,\text{drought}}$ and $K_{n,\text{standard}}$ (table 3.3). For high values of light saturation, the values of $K_{n,\text{drought}}$ and $K_{n,\text{standard}}$ can differ seriously,

Table 3.3: Parametrization of the K_n model according to van der Tol et al. (2014) for standard and drought conditions.

	Drought	**Standard**
γ	1.93	2.83
β	10	0.114
K_{n0}	5.01	2.48

since drought-stressed plants have the tendancy to increase the non-photochemical quenching as a photoprotective mechanism, leading to an incease in K_n. This behavior is more expressed for plants that experience a more intense form of drought stress. In this framework, we propose a weighted average $K_{n,\text{avg}}$ between the $K_{n,\text{drought}}$ and $K_{n,\text{standard}}$ based on the stress factor $\overline{\alpha}$ (Eq. 3.10).

$$K_{n,\text{avg}} = (1 - \overline{\alpha}) \cdot K_{n,\text{drought}} + \overline{\alpha} \cdot K_{n,\text{standard}} \tag{3.10}$$

The fluorescence yield (ϕ_f) is calculated based on the rate constants (Eq. 3.11). These rate constants allow us to interpret SIF emission in comparison to variables from pulse-amplitude modulated (PAM) fluorometry, in which fluorescence is induced with artificial light (Murchie and Lawson, 2013; Porcar-Castell et al., 2014). PAM experiments have established a link between ϕ_p and ϕ_f, based on the maximal fluorescence yield ($\phi_{F'_m}$), corresponding to the fluorescence yield after a saturating light pulse. In this situation, none of the absorbed light goes to the photosynthesis, causing $K_p = 0$ (Eq. 3.12).

$$\phi_f = \frac{K_f}{K_f + K_p + K_d + K_{n,\text{avg}}} \tag{3.11}$$

$$\phi_{F'_m} = \frac{K_f}{K_f + K_d + K_{n,\text{avg}}} \tag{3.12}$$

The actual link between ϕ_p and ϕ_f is established through the Genty relationship (Genty et al. (1989); Eq. 3.13). This relationship shows that drought stress affects ϕ_f in two ways: on one hand, stress causes ϕ_p to decrease, increasing ϕ_f. On the other hand, stress induces an increase in $K_{n,\text{avg}}$, causing $\phi_{F'_m}$ to decrease. The resulting behavior of these two effects characterizes the reaction of ϕ_f to drought stress.

$$\phi_f = (1 - \phi_p)\phi_{F'_m} \tag{3.13}$$

3.2.6 Use of SCOPE to link AgroC ϕ_f to spectrometer measurements

The AgroC-based ϕ_f differs from ϵ_{760} in two ways. First, ϕ_f considers the fraction of energy emitted as fluorescence over the entire fluorescent spectrum, not the emission at a specific wavelength. Second: ϕ_f is a leaf-scale property, while ϵ_{760} is based on canopy measurements. Therefore, ϕ_f cannot be directly compared to in situ measurements. To make ϕ_f comparable to ϵ_{760}, measured at the canopy scale at 760 nm, a SCOPE-based correction is required. While running the entire SCOPE model in combination with AgroC would be too computationally heavy, a SCOPE-based conversion factor κ has been used. This factor serves two purposes: first, it links the leaf-level ϕ_f to canopy-level ϵ_{760}, considering both leaf-scale and canopy-scale variables. Second, ϕ_f considers the whole fluorescent spectrum, while ϵ_{760} is restricted to the fluorescence emission at 760 nm (Lee et al., 2015; Qiu et al., 2018). Consequently, κ considers both the photosynthetic variable VCMax as well as the leaf and canopy variables. After a sensitivity analysis using the ARTMO's 3.2.6. global sensitivity analysis (GSA) tool, chlorophyll content (Chl), dry matter content (Cdm) and green area index (GAI) came out as the most sensitive variables. Given the little sensitivity of κ to leaf inclination distribution function parameters (LIDFa and LIDFb), leaf equivalent water content (Cw) senescent material (Cs) and carotenoid content (Car), these variables were kept constant (sensitivity analysis not shown). To calculate κ, the SIF emission at 760 nm emitted by all leaves (F_{tot}) was simulated for each combination of VCMax, Chl, GAI and Cdm. F_{tot} was then divided by fPAR $\cdot$ PAR to calculate $\epsilon_{F,SCOPE}$ (Eq. 3.14; Yang et al., 2020).

$$\epsilon_{F,SCOPE} = \frac{F_{tot}}{PAR \cdot fPAR} \tag{3.14}$$

Then, only the biochemical module of SCOPE was run with varying input for VCMax, to calculate the ($\phi_{f,SCOPE}$) for each value of VCMax.

$\phi_{f,\mathrm{SCOPE}}$ is not affected by Chl, GAI or Cdm. The ratio between SCOPE-based ϕ_f and $\epsilon_{760,\mathrm{SCOPE}}$ is defined as κ (Eq. 3.15).

$$\kappa = \frac{\phi_{f,\mathrm{SCOPE}}}{\epsilon_{760,\mathrm{SCOPE}}} \tag{3.15}$$

For each combination of input variables, a value of κ was calculated and written into a look-up table (LUT) (table 3.4). The minimal and maximal values were chosen based on literature values for sugar beet (Berger et al., 2018; Vilfan et al., 2019; Herbst et al., 2021). For Car, LIDFa and LIDFb, a seasonal mean was used based on the PROSAIL retrievals (section 3.2.7). These values were Car=12 μg cm^{-2}, LIDFa=-0.6, LIDFb=0.

Table 3.4: Settings of the SCOPE based LUT for κ. Note that the LAI parameter in SCOPE corresponds to the green area index (GAI).

Variable	**Symbol**	**Minimal**	**Maximal**	**Step**
Maximum carboxylation capacity (μ mol CO_2 m^{-2} s^{-1})	VCMax	5	200	5
Chlorophyll content (μg cm^{-2})	Chl	35	45	5
Dry matter content (g cm^{-2})	Cdm	0.003	0.007	0.001
Green area index (m^2 m^{-2})	GAI	3	4	0.2

Finally, based on the κ value, which derived from the SCOPE model, it is possible to convert ϕ_f, calculated by AgroC, to ϵ_{760} (Eq. 3.16). In this context, the κ accounts for the behavior of the fluorescent light as it propagates through the leaf and the canopy.

$$\epsilon_{760,\text{mod}} = \frac{\phi_{f,\text{AgroC}}}{\kappa} \tag{3.16}$$

3.2.7 Inverting PROSAIL to retrieve plant properties

The SIF signal is determined by the plant properties and by the photosynthetic activity. The plant properties can be estimated using the PROSAIL radiative transfer model, which simulates the reflectance-based on leaf and canopy properties (Verhoef et al., 2007; Féret et al., 2017). PROSAIL inversions were applied to the hourly time series of the hyperspectral reflectance, measured by the FloX spectrometer 2 (Figure 3.3), to estimate the leaf and canopy traits that were considered to calculate κ. Similar to van der Tol et al. (2016), a cost function was calculated using both the squared difference between modeled and observed reflectance values (R_m and R_{obs} respectively) and the squared difference between the posterior p and the *a priori* values p_0, normalized by the assumed standard deviation τ_p of each parameter and weighted by a coefficient w linking the two terms.

$$f_{\text{cost}} = (R_{\text{obs}} - R_m)^T (R_{\text{obs}} - R_m) + w \cdot \left(\frac{p - p_0}{\tau_p}\right)^T \left(\frac{p - p_0}{\tau_p}\right) \tag{3.17}$$

The value of w was set to 0.03 to compensate for the difference in the order of magnitude between the two terms. The *a priori* values and the assumed standard deviations were based on AgroC output for green area index (GAI) and Cdm, and Berger et al. (2018) for the other variables. GAI represents the amount of green area on a surface as seen by the spectrometer. This variable is better suited to calculate the radiative transfer compared to LAI. However, LAI is calculated by AgroC and is designed to upscale photosynthesis and transpiration to the plant level. The cost function f_{cost} was minimized using the global multi-level coordinate search optimization (GMCS) algorithm combined with the local Levenberg-Marquardt algorithm. As an additional constraint,

Table 3.5: Setting of the PROSAIL variables retrieved from the model. LB and UB refer to the lower and upper boundary of the optimization, respectively. p_0 refers to the a priori value and τ_p shows the expected variance.

Variable	**Unit**	**LB**	**UB**	p_0	τ_p
Chl	μg cm^{-2}	30	45	40	30
Car	μg cm^{-2}	6	15	10	7
Cdm	mg cm^{-2}	1	10	4	6
1-$e^{-0.2\cdot\text{GAI}}$	(-)	0	0.55	0.4	0.2
LIDFa	(-)	-1	1	-0.4	0.6
LIDFb	(-)	-1	1	0	0.6

|LIDFa|+|LIDFa| < 1 linked the two leaf inclination distribution parameters.

3.2.8 Optimize h_3 with observed and modeled ϵ_{760}

As illustrated in Figure 3.3, modeled ϵ_{760} time series draws input from different three sources. First, the plant and canopy parameters are retrieved based on the FloX-observed reflectance. VCMax was calculated in the AgroC model while taking temperature and drought stress into account. These variables are combined into κ, which is then combined with the AgroC-based variable ϕ_f, which also affected by the photosynthetic efficiency. The resulting $\epsilon_{F,\text{mod}}$ is then compared to the observed $\epsilon_{F,\text{obs}}$ by calculating the sum of squared errors (SSE; Eq. 3.18), which serves as the objective function F_{obj}, which is minimized using the local Nelder-Mead simplex algorithm.

$$\text{SSE} = \sum_{t=1}^{T} (\epsilon_{760,\text{mod}}(t) - \epsilon_{760,\text{obs}}(t))^2 \tag{3.18}$$

By minimizing the SSE, the h_3 is parameter optimized. An update in h_3 adapts the photosynthetic module, by changing ϕ_f and VCMax, but it leaves the PROSAIL-based leaf and canopy variables untouched.

3.2.9 Evaluating the modeled carbon and water fluxes

AgroC was run between February 1st, 2019, and November 15th, 2019. To evaluate the effect of estimated h_3 values from SIF measurements, AgroC was run with both a default value used in Klosterhalfen et al. (2017) and the optimized value for h_3 to validate time series of estimates of NEE and ETA with EC measurements. The Nash-Sutcliffe Model Efficiency Coefficient (NSE, (Nash and Sutcliffe, 1970)), defined as one minus the ratio of the model error to the variance in the observations (Eq. 3.19) served as the evaluation metric for the efficiency of the modeling of the carbon and water fluxes. An NSE close to 1 indicates that the simulations describe the observations well, while an NSE lower than 0 indicates that the mean of the observations is a better predictor than the simulations.

$$\mathrm{NSE} = 1 - \frac{\sum_{t=1}^{T}(\mathrm{obs}_t - \mathrm{mod}_t)^2}{\sum_{t=1}^{T}(\mathrm{obs}_t - \overline{\mathrm{obs}})^2} \tag{3.19}$$

The growing season was split into a mid-season (DOY 176-255), containing most of the stressed days, an early (DOY 130-175) and a late (DOY 256-319) season. The mid-season contained 110 mm of precipitation, while other years report a precipitation between 180 mm (in 2017) and 360 mm (in 2014). NSE was calculated for each sub-season as well as for the whole season. Covering the summer months, the mid-season is expected to be more affected by water stress compared to the early or late seasons. To validate the water fluxes, AgroC ETA was compared to ETA derived from in-situ EC latent heat flux (λE). Assuming that all the energy in the latent heat flux goes to evapotranspiration, and having binned the EC and meteorological data to a temporal resolution of one hour, ETA has been calculated based on T_{air} and specific heat evaporation of water at 0°C (ΔQ_v) (Eq. 3.20; Wieneke et al., 2018).

$$\mathrm{ETA} = \frac{\lambda E \cdot 3600}{(\Delta Q_v - 0.00242 \cdot T_{\mathrm{air}}) \cdot 10^6} \tag{3.20}$$

The EC-observed carbon fluxes were split into its GPP and its respiration component using the flux partitioning algorithm using the nighttime-based carbon flux data (Reichstein et al., 2005), as implemented in the REddyProc tool (Wutzler et al., 2018), allowing to validate both the photosynthesis and respiration component in the carbon

fluxes. AgroC splits the respiration component into an aboveground and a belowground component. This distinction cannot be made based on EC data.

3.2.10 Description of the growing season

Based on observations of the on-site weather station, the 2019 growing season had a mean temperature of 13.2°C at that site. The driest period was observed at the beginning of July, with low topsoil moisture and no precipitation (Figure 3.4). Water stress was centred around the summer months (Figure 3.5). The relatively good agreement between the modeled and measured topsoil moisture confirms the validity of the parametrization of Klosterhalfen et al. (2017) for the soil hydraulic parameters of the test site (Figure 3.5a). The modeled soil moisture time series show a short period of drought stress around DOY 120, but most of the water stress occurred from DOY 220 onwards (Figure 3.5). The modeled soil moisture exceeded the measured soil water content in during the FloX campaign, but the modeled soil water content was underestimated between DOY 100 and 150. This mismatch could cause the model to underestimate the stress conditions in that period. The SIF-based parametrization of h_3 resulted in more sensitivity to low water availability and it added a short drought period in May (Figure 3.5b).

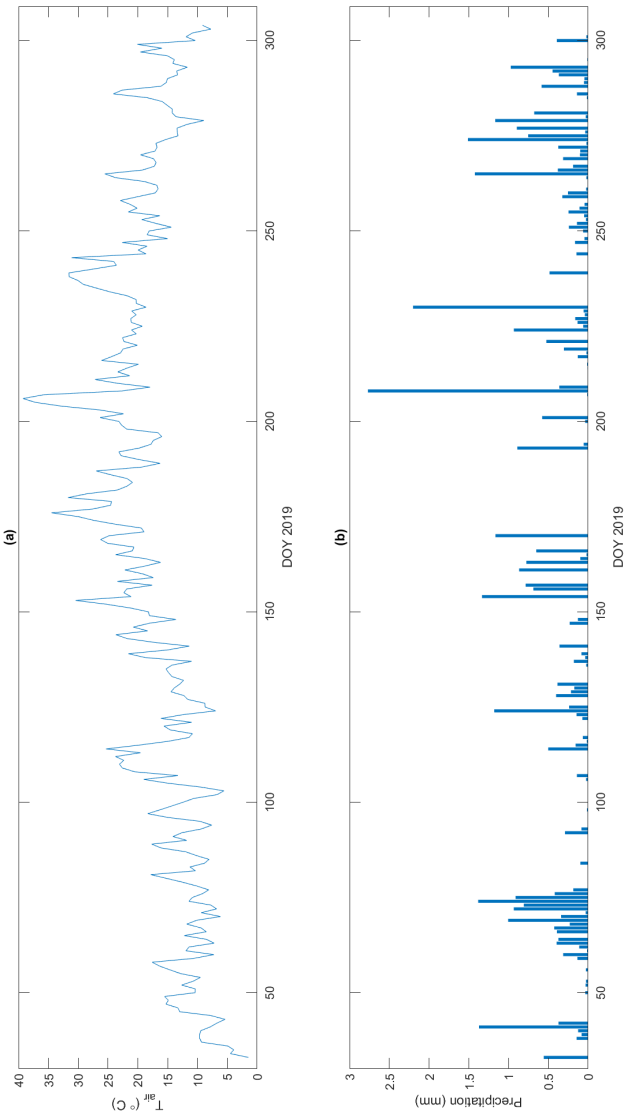


Figure 3.4: Description of the meteorology on the site consisting of (a) the evolution of the average air temperature between 11.30 UTC and 12.30 UTC (solar noon is at 11.30 UTC) and (b) the daily precipitation.

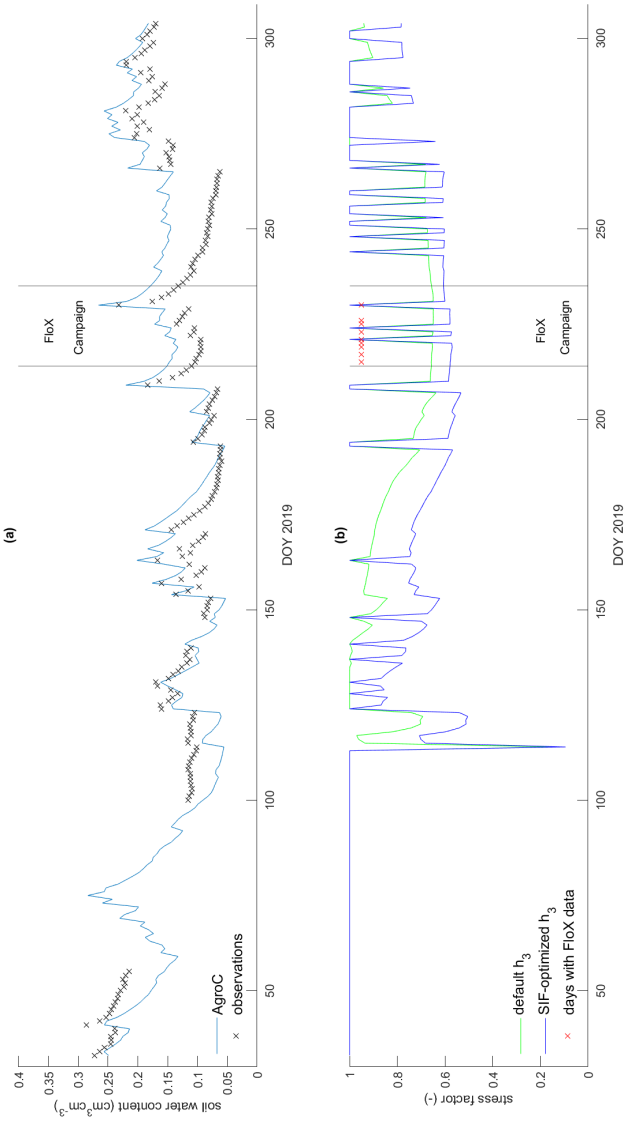


Figure 3.5: Description of the soil water status with different model parametrizations. (a): AgroC-SCOPE modeled topsoil water content at 5 cm compared to in-situ measurements; (b): water stress factor according to the two parametrizations of AgroC-SCOPE. SIF measurements were taken during the period of the FloX campaign.

3.3 Results

3.3.1 Forward modeling of ϵ_{760}

Figure 3.6 shows the comparison between modeled and observed ϵ_{760} for the SIF-optimized h_3. For the modeled ϵ_{760}, two AgroC-SCOPE simulations are considered: (i) one based on the SIF-optimized h_3 and (ii) one considering no stress. i.e., with a constant $\overline{\alpha} = 1$. The observed and modeled ϵ_{760} are in the same order of magnitude. Optimizing the h_3, the modeled ϵ_{760} leads to a better agreement betwen the model and the observations, lowering the SSE (table 3.6).

3.3.2 Sub-daily performance of ϵ_{760}

To gain a better insight into the behavior of ϵ_{760} and its reaction to drought stress, the daily evolution of ϵ_{760} was plotted for DOY 215 and DOY 219, along with the NEE and the PAR of these days. Between DOY 215 and DOY 219, a series of precipitation events took place, which is expected to provide for some stress relief. Both days report a higher variability in the observed ϵ_{760} compared to the modeled ϵ_{760}. DOY 215, which occurred before the precipitation events, reported an ϵ_{760} around $2 \cdot 10^{-5}$ nm^{-1}, while its modeled counterpart remained around $2.5 \cdot 10^{-5}$ nm^{-1}. In the case of DOY 219, the observed ϵ_{760} hovered around the modeled one.

3.3.3 SIF-constrained h_3 corrects NEE estimates in summer months

Figure 3.8 compares the NEE estimates at noon with the two different AgroC parametrizations. It shows that estimating the h_3 parameter from SIF measurements resulted in a significant improvement in

Table 3.6: Sum of squared errors (SSE) between modeled and observed ϵ_{760} and considering two model parametrizations (no stress and SIF-based h_3).

h_3 **parametrization**	**SSE**
no stress ($\overline{\alpha} = 1$)	$6.9 \cdot 10^{-9}$nm^{-2}
h_3=-730 cm (SIF-based)	$3.3 \cdot 10^{-9}$nm^{-2}

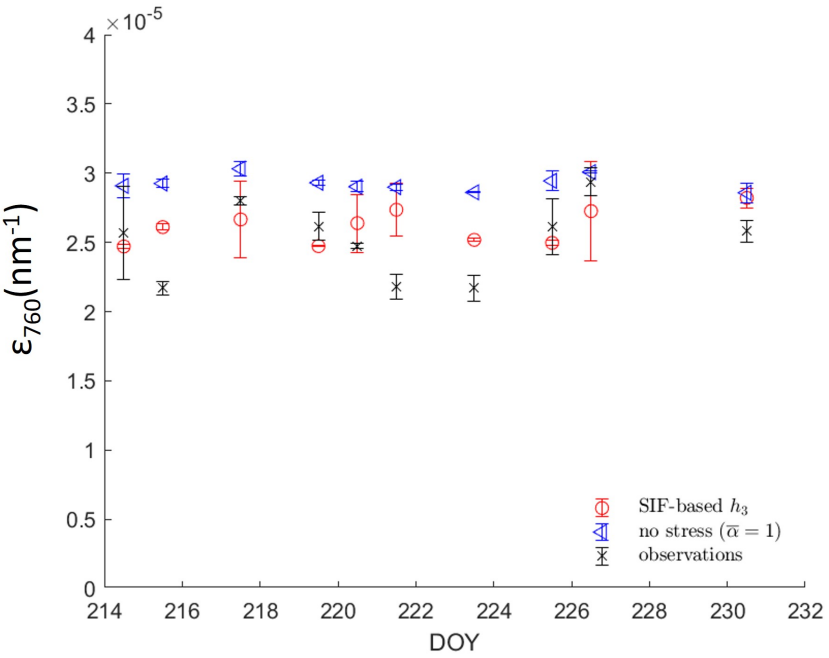


Figure 3.6: Daily averages of modeled ϵ_{760} time series using two model parametrizations (SIF-based h_3 and no stress) compared to daily averages of observed ϵ_{760} with their standard deviation. It should be noted that the FloX data were resampled to an hourly resolution before averaging. On DOY 225 and DOY 226, only data between 10 AM and 12 AM have been used.

the mid-season NEE estimates, as the default parametrization from (Klosterhalfen et al., 2017) underestimates the water stress in the mid-season, explaining the difference in NSE between both model runs (table 3.7). As the sugar beets experienced less water stress in the late season, calculating h_3 based on SIF observations did not improve the NEE estimates there. Considering the entire growing season, the model run with the SIF-optimized value for h_3 had the best NSE. Given the time-invariant nature of the Feddes curve, our approach leads to improvements in the NEE throughout the entire growing season, not only during the period in which the SIFA measurements were taken. Using only a few observations of ϵ_{760} during a drought-affected period was sufficient to correct the entire growing season. The GPP and Res

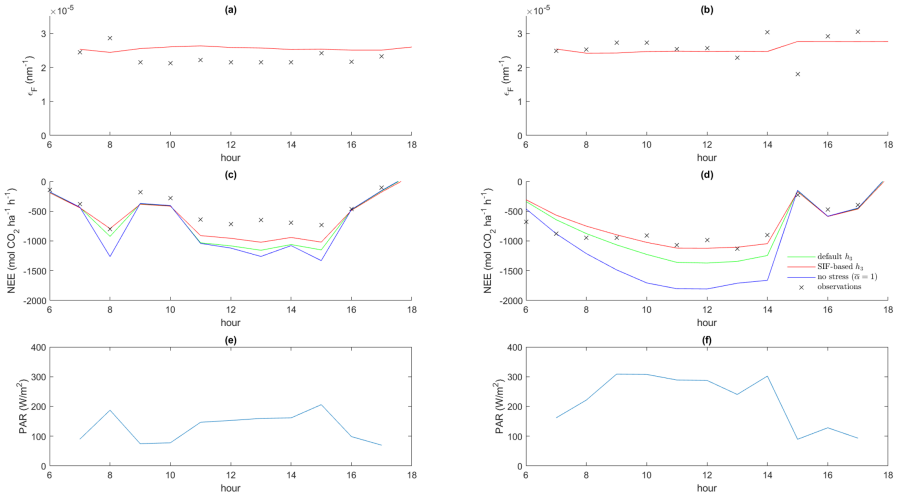


Figure 3.7: Hourly AgroC-SCOPE modeled ϵ_{760} and modeled NEE according to the three model parametrizations compared to observed data for DOY 215 (a, c) and DOY 219 (b, d), as well as hourly observed PAR data for DOY 215 (e) and DOY 219 (f).

Table 3.7: NSE for the NEE estimates in different parts of the growing season estimated with different parametrizations for the AgroC-SCOPE model.

Period	**Default h_3**	**SIF-based h_3**	**No Stress ($\overline{\alpha} = 1$)**
Early season	0.59	0.81	0.53
Mid season	0.60	0.78	0.35
Late season	0.81	0.79	0.81
Whole season	0.62	0.80	0.42

fluxes of the AgroC model are not compared separately to the EC fluxes of GPP and RES, since both the flux partitioning algorithm also relies on a series of assumptions and modeling, making it hard to estimate whether AgroC or EC does a better job in representing the in-situ situation. This is not the case for NEE, which comes more directly from the EC tower.

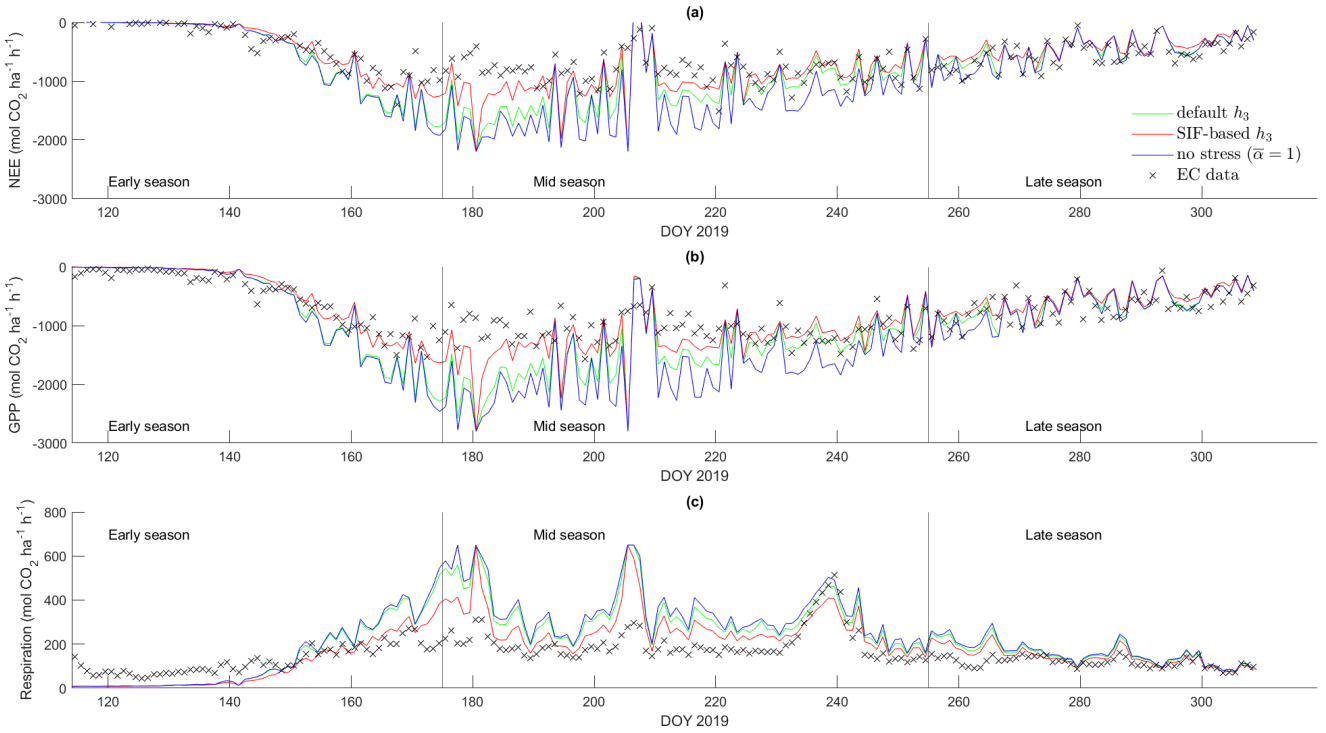


Figure 3.8: (a) NEE by AgroC-SCOPE according to three different model parametrizations and EC derived NEE; (b) GPP by AgroC-SCOPE according to three model parametrizations and EC derived GPP; (c) Respiration by AgroC-SCOPE according to three model parametrizations and EC derived respiration.

Table 3.8: NSE for the ETA estimates in different parts of the growing season estimated with different parametrizations for the AgroC-SCOPE model.

Period	**Default h_3**	**SIF-based h_3**	**No Stress ($\overline{\alpha} = 1$)**
Early season	0.84	0.87	0.82
Mid season	0.68	0.81	0.37
Late season	0.81	0.78	0.79
Whole season	0.66	0.70	0.55

Most of the correction in NEE comes from a correction in GPP, which is directly affected by the photosynthetic activity (Figure 3.8). All three model runs overestimated the respiration during almost the entire growing season, but the model run with the SIF-based parametrization shows the least overestimation in the respiration component.

3.3.4 Ability of AgroC to predict plant water fluxes

Correcting h_3 affects the modeled ETA in two ways: first, the stress factor $\overline{\alpha}$ serves as a scaling factor to convert the potential transpiration (TP) to actual transpiration (TA). Second, long-term drought stress exposure leads to reduced modeled plant growth, decreasing the modeled plant transpiration, which scales with the AgroC-modeled LAI. Calibrating the h_3 parameter with SIF observations also improved the mid-season ETA estimates, but the impact was less pronounced than for the NEE time series (table 3.8). At the later stages of the growing season, most of the stress-induced decrease in transpiration was compensated by an increase in evaporation, minimizing the effect of the stress factor on ETA (Figure 3.9).

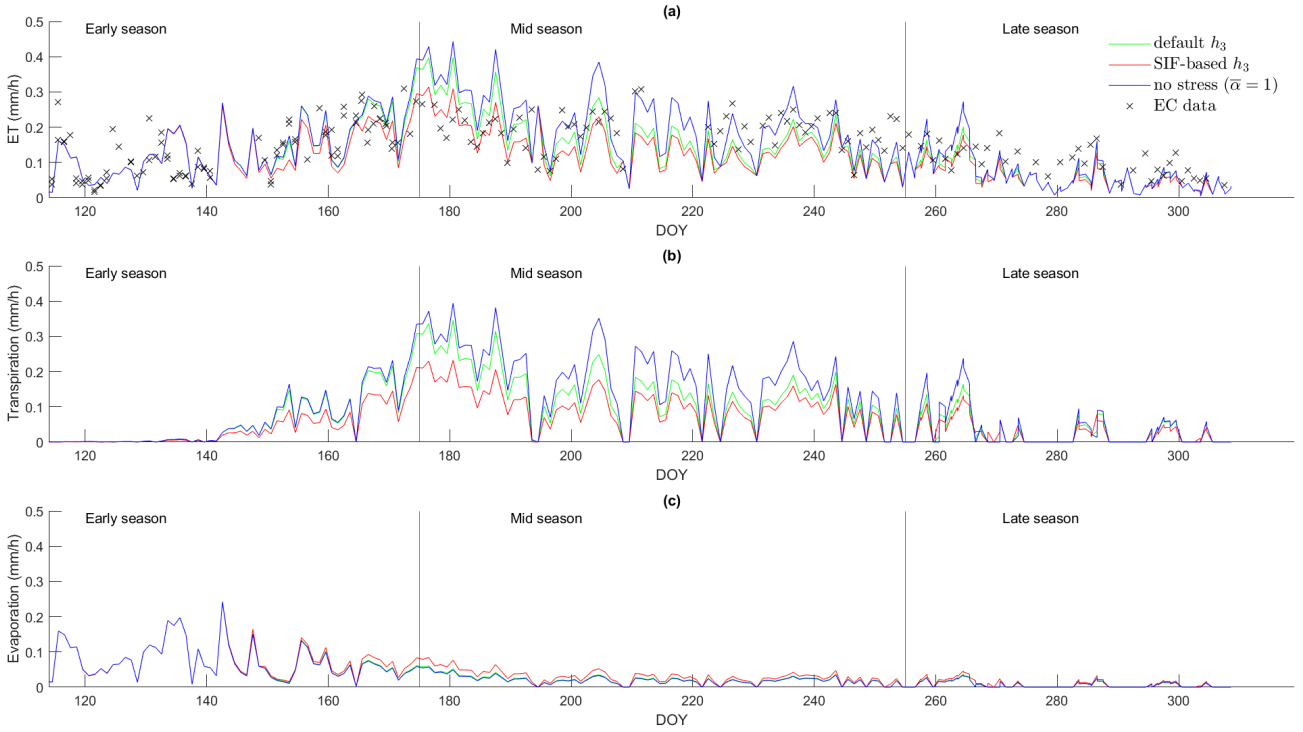


Figure 3.9: (a) AgroC-SCOPE modeled evapotranspiration using different parametrizations compared to EC-derived evapotranspiration; (b) modeled transpiration; (c) modeled evaporation.

3.4 Discussion

3.4.1 Measurement differences between the FloX and the EC tower data

One of the challenges of integrating EC and tower-based spectrometer data in the AgroC-SCOPE model lies in the difference in footprint size between the FloX spectrometer (2.4 m^2, right below the sensor) and the EC station; 80 to 100 % of the footprint comes from less than 20 m to 100 m distance from the tower depending on the wind conditions. In all cases, the footprint of the EC tower is expected to remain within the field. AgroC is a one-dimensional model that produces estimates of NEE and ETA at the scale of the whole field, as was done by Klosterhalfen et al. (2017) for the same field. Herbst et al. (2021) expanded the AgroC model by incorporating a description of the soil properties at a sub-field scale. While they noted some significant within-field variability in the case of drought stress, it had only little effect on the overall NEE estimates. Linking the crop growth model to spatially distributed SIF measurements might improve its ability to assess the susceptibility of the field to water stress, but it is beyond the scope of this study.

3.4.2 Stress-induced changes in canopy structure

In the context of drought stress monitoring, it is necessary to provide information on the temporal variability of the dynamic canopy structure, since a drop in turgor pressure might change the leaf inclination (Jopia et al., 2020). This profoundly affects the SIF signal, as confirmed by observations (Dechant et al., 2020) and by SCOPE model (Verrelst et al., 2015). The uncertainties in the parametrization at both the leaf biochemical and canopy level makes the variability in SIFA hard to model (van der Tol et al., 2016; Wohlfahrt et al., 2018). Given the number of variables affecting the SIF signal, many studies dealing with SIFA simulations only used a limited number of input time series to produce SIFA while keeping the other inputs constant (Lee et al., 2015; Qiu et al., 2018). Consequently, these studies report a lower variability in the modeled SIFA time series compared to their observed counterparts. Model sensitivity to the uncertainties in the parametrization of the canopy structure can be reduced by normalizing the SIFA by

FCVI, making the signal easier to interpret in biochemical terms. Consequently, ϵ_{760} appears to be a more suitable metric for detecting a stress-induced reduction in photosynthetic activity compared to SIFA itself. As an alternative, it would also be possible to retrieve canopy-scale ϕ_f using the methods of (Celesti et al., 2018). It is however worth noting that the change in the structural component itself can also bear information about the plant water status, because of its link to the leaf turgor.

3.4.3 Applicability of this framework to other vegetation models

The main merit of this study is the establishment of a quantitative link between water stress, water availability, photosynthesis and canopy-scale SIF emission, illustrated by coupling the AgroC and SCOPE models. In AgroC, water stress is described with the Feddes function and with water availabilities at different depths. While this exact structure is unique to the SoilCO2/RothC part of AgroC, the concept of a threshold value by which water stress starts to occur is found in various crop growth models (Tolomio and Casa, 2020). The same concept has also been used to constrain VCMax in SCOPE and thereby improve its GPP output (Bayat et al., 2019). If the input data can be aggregated correctly, AgroC, as well as many other crop growth models, can be run at the catchment scale or larger (Kuhnert et al., 2017). Problems might arise when models are run at a lower temporal resolution, since photosynthesis, non-photochemical quenching and therefore fluorescence shows a clear diurnal signal. To properly estimate the rate coefficients (i.e., K_p, K_n, K_d and K_f), an accurate description of the environmental conditions at the time by which the SIF measurements are taken is needed.

3.4.4 Perspectives on water stress function parametrization with spaceborne SIF data

This framework provides a method to define a stress level that considers both the SIF emission and the soil water availability. Since the soil water availability is modeled for the entire growing season, our

approach improves the water stress estimation for the entire growing season, even on days without SIF observations. This is interesting in the light of the upcoming FLEX mission, which comes with a spatial resolution of 300 m and a temporal resolution of 27 days. This resolution allows for the collection of a few SIF observations at the field scale during each growing season, which is expected to be sufficient to constrain a water stress function in a crop growth model. Improving the parametrization of the drought stress function is expected to provide major improvements in the field of land surface modeling (Verhoef and Egea, 2014; Jonard et al., 2020).

3.4.5 In-situ validation of water stress function parametrization

Because of the importance of water stress in a plant's water regime (Vereecken et al., 2008) and thereby its influence on photosynthesis and transpiration, considerable effort has been invested in the in-situ or lab-scale parametrization of these functions (Cai et al., 2018a,b). While these methods succeed in parametrizing a water stress function with great precision, their potential of characterizing a stress function at large scale is limited, possibly masking the spatial variability in the water stress conditions. Hupet et al. (2003) managed to inversely estimate the root water uptake parameters based on soil moisture data obtained with ground-penetrating radar. Only relying on soil moisture data, their approach does not account for the variation in a plant's ability to extract water. The framework proposed here relies on few SIF observations, causing it to be suitable at a large spatial scale. Because of the direct link between VCMax, SIF emission and water stress, SIF provides more direct information about the plant water status. However, VCMax depends on the initial value of VCMax,25 as well as on $\overline{\alpha}$, which depends on the Feddes function and soil water content, which in turn depends on the soil hydraulic properties. Neither the Feddes function nor VCMax nor the soil hydraulic properties is easy to obtain through in-situ measurements. Any error in the initial estimation of VCMax or in the soil hydraulic properties is therefore inevitably translated to a compensating error in $\overline{\alpha}$ through the estimation of h_3. It is therefore hard to interpret the value of $\overline{\alpha}$ outside of this model, and

it might disagree with plant-based in-situ measurements of drought stress.

3.5 Summary and outlook

This study establishes a framework for parametrizing a drought stress function in a crop growth model using SIF observations, by coupling the AgroC crop growth model with the SCOPE model. Because of the many variables affecting the SIF signal, the AgroC-SCOPE model was not able to reproduce the variability in the observed SIF signal. Nevertheless, accounting for drought stress corrected a systematic overestimation of the ϵ_{760} by adjusting the parametrization of the Feddes function in AgroC. It should be noted that through the inversion procedure, the optimal value of h_3 is affected by many model parameters regarding photosynthesis and on soil water availability. The new parametrization changed the stress factor and therefore the VCMax, in turn changing the estimates of photosynthetic activity. This leads to better estimates of NEE and ETA during the summer months. While the ϵ_{760} observations only covered a short subset of the growing season, a better estimate of h_3 improves the ETA and NEE estimates throughout the entire growing season. This is potentially interesting for using FLEX data to estimate drought stress. With FLEX being the first satellite designed to monitor SIF emission, it will be able to retrieve SIFA with a higher signal-to-noise ratio and a higher spatial resolution (300 m) compared to previous satellites. Since FLEX has a revisit time of 27 days, it will only provide a few data points during each growing season. Using the framework established here, we expect that the few SIFA observations provided by FLEX will provide significant improvement to the crop growth model and land surface model estimates during drought conditions.

3.6 Appendix: description of the photosynthesis model based on Farquhar approach

The photosynthesis module in AgroC makes use of a Farquhar et al. (1980)-based approach, tailored to the SUCROS model (Spitters et al.,

1988). It considers three scenarios: light-limited photosynthesis, water-limited photosynthesis and rubisco-limited photosynthesis. Photosynthesis depends on the meteorological conditions including absorbed photosynthetically active radiation (APAR), atmospheric pressure (P_{atm}), air temperature (T_{air}), relative humidity (RH) and the ambient CO_2 and O_2 concentration (c_s and o_i). The plant physiological parameters are VCMax, the CO_2 partial pressure at compensation point (Γ^*). The latter variable is calculated based on o_i and the temperature coefficients K_c and K_o:

$$\Gamma^* = 0.5 \cdot \frac{K_c}{K_o} \cdot 0.21 \cdot o_i, \tag{3.21}$$

in which the temperature coefficients are based on T_{air} and on constants: $K_{c25} = 30$ Pa and $K_{o25} = 30000$ Pa at $25°C$ as well as $a_{Kc} = 2.1$ and $a_{Ko} = 1.2$ (Eq. 3.22-3.23).

$$K_c = K_{c25} \cdot (a_{kc})^{\frac{T_{\text{air}}-25}{10}} \tag{3.22}$$

$$K_o = K_{o25} \cdot (a_{ko})^{\frac{T_{\text{air}}-25}{10}} \tag{3.23}$$

The VCMax (Eq. 3.2) is calculated based on the VCMax,25, $\overline{\alpha}$ and on the temperature sensitivity factor ($f(T_{\text{air}})$; Eq. 3.24), which is calculated based on T_{air}, the freezing temperature of water (T_{freeze}) (both expressed in Kelvin) and on the universal gas constant (R_{gas}):

$$f(T_{\text{air}}) = \left[1 + \exp \frac{-220000 + 710 \cdot (T_{\text{air}} + T_{\text{freeze}})}{0.001 \cdot R_{\text{gas}} \cdot (T_{\text{air}} + T_{\text{freeze}})}\right]^{-1} \tag{3.24}$$

As implemented in SCOPE, the c_i was calculated in Eq. 3.25:

$$c_i = \max\left(\Gamma^*, c_s \cdot \left(1 - \frac{1.6}{m \cdot \text{RH} \cdot \overline{\alpha}}\right)\right) \tag{3.25}$$

in which m is the Ball-Berry slope parameter. Photosynthesis (A) is finally calculated as the minimum of water/carboxylation limited (first part) and the light limited (second part) photosynthesis (Eq. 3.26):

$$A = \min\left(\frac{\text{VCMax} \cdot (c_i - \Gamma^*)}{c_i + K_c \cdot (1 + o_i/K_o)}, \frac{(c_i - \Gamma^*) \cdot 4.6 \cdot \text{APAR} \cdot \zeta}{c_i + 2 \cdot \Gamma^*}\right) \tag{3.26}$$

in which the quantum efficiency ζ was set to 0.06.

Chapter 4

Water availability and atmospheric demand controls on spaceborne SIF yield

This chapter is based on the following article:

De Cannière, S., Baur, M., Chaparro, D., Jagdhuber, T., Jonard, F. Water availability and atmospheric dryness controls on spaceborne sun-induced chlorophyll fluorescence yield, in revision in Remote Sensing of Environment.

Abstract

Climate change is amplifying the duration, frequency, and intensity of droughts, harming global ecosystems. During droughts, plants can close their stomata to save water, at the expense of a reduced carboxylation rate. When in a carboxylation-limited regime, plants benefit from an increase in water availability, as it increases their photosynthetic rate. The sun-induced chlorophyll fluorescence (SIF) signal, measurable from satellites, is mechanistically linked to this rate. Like canopy photosynthesis, SIF carries an imprint from the available irradiation (PAR) as well as on the canopy structure and on the efficiency of the photosynthesis at the photosystem level. Normalizing the global TROPOMI SIF observations with TROPOMI reflectance and MODIS Normalised Difference Vegetation Index (NDVI) data, we extracted the fluorescence quantum yield (ϕ_F), which lab-scale experiments have found to be linked to the photosynthetic efficiency. Plant physiologists have long proved the photosynthetic efficiency to be sensitive to plant water status conditions. Here, the plant water status is controlled by the soil moisture (SM) and the vapour pressure deficit (VPD). Combining data from the TROPOMI, AIRS and SMAP satellite sensors, this study describes how SM and VPD affect the ϕ_F at the global scale. We identify a VPD range (VPD $<$ 1.5 kPa) in which the ϕ_F is mainly controlled by VPD, and another (VPD $>$ 1.5 kPa) in which the ϕ_F is co-regulated by SM and VPD. The precise values of this range, as well as the magnitude of ϕ_F values are affected by the plant isohydricity. To gain a deeper understanding of the link between ϕ_F and photosynthetic efficiency at large scale, we used the link between ϕ_F and data on the canopy conductance (Gs), that were calculated using remote sensing data-driven models. A comparison found that the ϕ_F-Gs relationship at large scale is in line with the ϕ_F-Gs relationship described in plant-level studies.

4.1 Introduction

Water is an essential element for plants to grow and for ecosystems to function. Changes in the ecosystem water status jeopardize the ecosystem health, reduce crop yields and may lead to forest fires, among other impacts (Gupta et al., 2020; O et al., 2020; Venturas et al., 2021). Due to climate change, droughts are an increasingly relevant problem in the coming decades (Balting et al., 2021). From a plant physiological perspective, a drought is a shortage of water availability, combined with high atmospheric water demand (Orimoloye, 2022). This induces a series of possible reactions, which include stomatal closure, decreased photosynthetic activity, leaf water loss, cavitation, chlorophyll degradation and accelerated senescence (West et al., 2019; Jonard et al., 2011). Over the last 50 years, remote sensing has proven its value for large-scale drought stress monitoring. First-generation Earth Observation (EO) satellites have used the canopy greenness as an indicator of an ecosystem's stress status (West et al., 2018), as damaged plants tend to shed or brown their leaves. While very intuitive, greenness only provides limited information on plant physiology. Data streams generated by new-generation EO satellites are focused on signals that are more closely linked to plant health, establishing a link between the fields of plant physiology and remote sensing (Jonard et al., 2020; Mohammed et al., 2019). A key variable in this school of thought is the sun-induced chlorophyll fluorescence (SIF) signal, which originates in the heart of the photosynthetic apparatus (Porcar-Castell et al., 2021).

The mechanistic link between SIF and photosynthesis finds its origins at the level of PSII. The PSII is responsible for the electron harvesting from a water molecule and for sending it to the electron transport chain. For a PSII to provide this energy, its outermost electron pair jumps to a higher energy level, forming an excited PSII (PSII*). The energy trapped by this photosystem is split over three pathways. The first pathway is the photochemical electron chain, fuelling the Calvin cycle. The second pathway is a container category of processes that dissipate the excess trapped energy as heat. These are collectively known as non-photochemical quenching (NPQ). As a final pathway, the trapped photon can be re-emitted as chlorophyll fluorescence (Porcar-Castell et al., 2014). The fraction of photons going down each pathway is referred to as the photochemical quantum yield (ϕ_p), the non-photochemical

quantum yield (ϕ_N), and the fluorescence quantum yield (ϕ_F), respectively. The ϕ_F emission typically varies between 1 and 3% of the absorbed light radiation (Jonard et al., 2020). A lowered carboxylation decreases the energy demand by the photosynthetic electron transport chain, decreasing ϕ_P, increasing ϕ_N, which leads to a decrease in the life-time of the excited state of photosystem II (PSII*), decreasing ϕ_F (van der Tol et al., 2014). Consequently, it was possible to link ϕ_F to stomatal conductance (Gs) using leaf-level measurements (Flexas et al., 2002). Canopy-scale SIF is the aggregate of the fluorescence emission of all photosystems, the rate of which is determined by ϕ_F. Therefore, ϕ_F can be conceptualized as the physiological component of SIF.

Given its use in the field of plant physiology, there is an increasing interest in finding remote sensing based estimates of ϕ_F. Tower- or drone-based remote sensing studies have retrieved ϕ_F at the canopy scale and managed to observe a reaction in ϕ_F in function of the water availability (De Canniere et al., 2022; De Cannière et al., 2021; Wang et al., 2023; Xu et al., 2021). Similarly, Kimm et al. (2021a) pointed out the importance of the water demand, quantified by the vapour pressure deficit (VPD). Both high VPD and low SM lead to a reduction in ϕ_F. Helm et al. (2020) links the drought-induced decrease in ϕ_F to a decrease in Gs. At the satellite scale, fewer studies use ϕ_F in favour of SIF, that has shown to be reactive to drought conditions. Sun et al. (2015) linked different drought categories from the US drought monitor (Svadoba et al., 2002) to the ecosystem-scale SIF.

However, the SIF drought reaction is determined by a simultaneous canopy structural and physiological change (Dechant et al., 2020), the sum of which caused a SIF decrease that goes together with a GPP decrease (He et al., 2020). The combination of the structural and physiological components makes SIF a more performant drought diagnostic compared to greenness indices (Qiu et al., 2022). Recently, regional satellite-based studies have isolated physiological component and observed its reactivity to droughts (Gu et al., 2023; Zhang et al., 2023). Dechant et al. (2022) propose an efficient method for retrieving ϕ_F from satellite-based sensors, by normalizing the SIF. A global, satellite-based dataset of ϕ_F opens the door to an improved interpretation of SIF data through an ecophysiological lens.

Two environmental variables that stand out as constraining factors on the ecosystem-scale photosynthesis and SIF emission are water

availability, typically quantified with the SM and the atmospheric water demand, quantified with the VPD (Fu et al., 2022; Lu et al., 2022). In order to interpret the control of VPD and SM on photosynthesis, and therefore on ϕ_F and SIF, it is important to consider the stomatal behaviour. The connection between Gs, ϕ_F and photosynthesis is well-established at the plant level. The specific nature of this connection at the ecosystem level differs on a series of ecosystem properties, of which isohydricity is a key trait. Isohydricity is an ecophysiological trait that describes the sensitivity of the stomata to increasing drought conditions. A plant is more isohydric if its stomata are sensitive to drought (i.e., they tend to close in response to drought), and more anisohydric if the stomata are less sensitive (i.e., they tend to remain open despite of drought conditions). More isohydric plants save up water during drought periods at the cost of a lower carboxylation rate, while more anisohydric plants maintain high photosynthetic rates during drought periods, putting themselves under risk of hydraulic failure but potentially outperforming their more isohydric neighbours (Novick et al., 2019). Considering the environmental variables soil moisture (SM) and vapour pressure deficit (VPD), as well as the physiological variables Gs and ϕ_F at the ecosystem scale, we hypothesize that: (i) VPD and SM are important controlling factors on ϕ_F, (ii) as anisohydric plants are known to have a less strict stomatal response to changes in environmental factors, an effect of the anisohydricity is expected on the response of ϕ_F to VPD and SM, (iii) an effect of soil water retention characteristics is expected on the response of ϕ_F to VPD and SM and (iv) the relationship between canopy conductance (Gs) and ϕ_F holds in a way it holds at the scale of the individual plant (e.g., Flexas et al., 2002).

4.2 Materials and Methods

4.2.1 Data

L-band passive microwave soil moisture from SMAP

Passive microwave remote sensing at L-band (1.4 GHz) provides an excellent tool for monitoring soil moisture regularly and globally. Advantages of this technique include: (i) compared to higher frequencies, the longer wavelengths maximize the soil depth to which the signal is

sensitive; (ii) clouds are transparent, allowing for all-weather retrievals and (iii) compared to active microwave techniques and to shorter wavelengths, L-band passive microwave emission is less affected by the canopy structure. The coarse spatial resolution of passive microwave SM retrievals is particularly suited for regional to global scale research. This study makes use of L-band SM data from the Soil Moisture Active Passive (SMAP) satellite (Entekhabi et al., 2010) retrieved using the Multi-Temporal Dual-Channel Algorithm (MT-DCA; Konings and Gentine, 2017). The data come at a 3-day temporal resolution and 9 km spatial gridding.

Atmospheric data from AIRS

The evaporative water demand is monitored with the Atmospheric InfraRed Sounder (AIRS) instrument, on NASA's Aqua satellite, launched in 2002 (Aumann et al., 2003). This instrument measures the infrared radiance at 2378 spectral samples, located in three spectral regions of the thermal infrared. Along these bands, atmospheric trace gasses, like CO_2 and H_2O, have different absorption spectra. Using this information, AIRS retrieves a vertical transect of temperatures and atmospheric trace gasses concentrations at the global scale with a daily resolution (Aumann et al., 2003). This allows computing daily data of VPD (Eq. 4.1-4.2) based on the saturation water vapour pressure (e_{sat}; kPa), air temperature (T_{air}; ^{o}C) and the air relative humidity (RH; %).

$$e_{sat} = 0.61094 \cdot e^{\frac{17.625 \cdot T_{air}}{T_{air}+243.04}} \tag{4.1}$$

$$\text{VPD} = e_{sat} \cdot \left(1 - \frac{\text{RH}}{100}\right) \tag{4.2}$$

Both Sentinel-5P (used to retrieve SIF; see Section 2.1.3) and Aqua satellites have their overpass times at 13.30, minimizing the diurnal shift between the VPD and SIF measurements. AIRS provides daily atmospheric data at 1^{o} spatial resolution. Using linear interpolation, the 1-degree dataset is re-gridded to a 9 km Equal Area Scalable Earth version 2 (EASE-2) grid. When interpreting VPD at a large scale, it is important to realize that VPD, air temperature and solar irradiation are tightly interconnected and that a VPD effect is hard to distinguish from an irradiation or a temperature effect.

SIF and NIR data from TROPOMI

The SIF data were taken from the 'TROPOSIF' product (Guanter et al., 2021), that retrieves SIF emission at its 743 nm emission peak (in mW m^{-2} sr^{-1} nm^{-1}) from the TROPOMI sensor onboard the Sentinel-5P satellite. The retrieval uses the spectral fitting window between 743 and 758 nm and relies purely on solar Fraunhofer lines, reducing its sensitivity to atmospheric effects compared to retrieval methods that include the atmospheric absorption bands. For the SIF retrieval, the observed signal over the different bands is split into a smooth (true) reflectance signal and a fluorescence signal. The latter makes up for the difference between the true and apparent reflectance (i.e., the reflectance as observed by the satellite). The retrieval assumes cloud-free conditions. The same TROPOSIF product also provided the broadband NIR radiances (NIR_{RAD}; in mW m^{-2} sr^{-1} nm^{-1}). TROPOMI has a 16-day revisit time and a swath of 2600 km, allowing it to combine nadir and off-nadir measurements. This combination allows a daily global coverage. The spatial resolution of the data product goes up to 3.5 km x 5.5 km at nadir, while going down to 14.5 x 5.5 km off-nadir. Each data point in the TROPOSIF product contains a quality value, with penalties for high Solar Zenith Angle (SZA), a low average top of atmosphere (TOA) NIR_{RAD}, an extreme value for SIF, or a high Viewing Zenith Angle (VZA). As a final quality control, the χ^2-value between the calculated and observed spectra is calculated, allowing to identify the retrievals that have been hampered by clouds. The calculated spectrum is the sum of the smooth (true) reflectance and the fluorescence. Following the recommendations laid out in Guanter et al. (2021), this study only selected TROPOSIF SIF and NIR_{RAD} data that did not take any penal point from the beforementioned categories. In the TROPOSIF dataset, SIF values can be negative. These values are the result of the lack of ground-based calibrations, as well as of a series of noise introduced by the atmosphere. Negative SIF values were mainly reported over areas with only sparse vegetation. While negative SIF values are not physical, they do represent the regions with the lowest SIF emissions and deleting the negative SIF values would introduce a negative bias in the system. Therefore, the negative SIF values were considered in our analyses. The negative data comprised of 23% of the data.

NDVI data from MODIS

Information on the vegetation development comes from NDVI data, that were obtained from the MOD13C1 product (Didan, 2015). This product is derived from the MODerate Imaging Spectroradiometer (MODIS) on board of the Aqua satellite. This product bins two 8-day composite surface reflectance granules into a 16-day period and is set out on a 0.05^0 grid. The product has a staunch quality control, removing any cloud-affected data. In a second instance, the data were spatially aggregated and temporally interpolated to form a global 9 km product at a daily resolution. This approach allows to get a smooth signal on the vegetation development that minimizes the cloud effects, that profoundly affect the NDVI retrieval. Table 4.1 gives an overview of all the used remote sensing products, as well as on their resolutions. All datasets were re-gridded to 9 km and linearly interpolated to a daily time-step.

Table 4.1: Overview of used sensors and data products.

Variable	Sensor	Spatial grid	Time step	Reference
Soil Moisture	SMAP	9 km	3 days	(Konings et al., 2017)
NDVI	MODIS	0.05^o	16 days	(Didan, 2015)
VPD	AIRS	1^o	1 day	(Aumann et al., 2003)
NIR_{RAD}	TROPOMI	Up to 3.5 km x 5.5 km	1 day	(Guanter et al., 2021)
SIF_{740}	TROPOMI	Up to 3.5 km x 5.5 km	1 day	(Guanter et al., 2021)

Isolating the physiological component from SIF to create a global ϕ_F dataset

To convert satellite-based SIF to ecosystem-scale ϕ_F values, three multiplicative factors need to be considered (Jonard et al., 2020) (Eq. 4.3). However, the precise implementation is slightly different from a satellite-based sensor compared to a local-scale sensor.

$$\mathrm{SIF} = \mathrm{PAR}{\cdot}\mathrm{fPAR} \cdot \phi_\mathrm{F} \cdot f_{esc} \tag{4.3}$$

The first term is the photosynthetically active radiation (PAR), that fuels the photosynthesis. The second factor is the fraction of this PAR that the leaves absorb (fPAR). Finally, there is the escape probability (f_{esc}), the probability of a re-emitted photon by PSII to reach the sensor. The non-physiological part of SIF, being the fPAR, PAR and f_{esc} can be grouped in the NIRvP variable (Dechant et al., 2022) as in Eq. 4.4.

$$\mathrm{NIRvP} \approx \mathrm{PAR}{\cdot}\mathrm{fPAR}{\cdot} f_{esc} \tag{4.4}$$

While SIF has very strict spectral retrieval requirements, NIRvP can be measured by using only the Normalized Difference Vegetation Index (NDVI) and the reflected radiance in thetop of atmosphere near-infrared part ($\mathrm{NIR_{rad}}$), as shown in Eq. 4.5.

$$\mathrm{NIRvP} = \mathrm{NDVI}{\cdot}\mathrm{NIR_{rad}} \tag{4.5}$$

Finally, normalizing SIF by NIRvP provides an estimate for ϕ_F (Eq. 4.6), the fluorescence yield (Zeng et al., 2022):

$$\phi_\mathrm{F} \approx \frac{\mathrm{SIF}}{\mathrm{NIRvP}} \tag{4.6}$$

As an additional quality control on the TROPOSIF product, data points of ϕ_F with a NIRvP < 25 $\mathrm{mWm^{-2}sr^{-1}nm^{-1}}$ were not considered, as they represent too small vegetation or too low solar radiations.

4.2.2 Evaluating the effect of environmental factors on ϕ_F

Grasping the spatial and temporal variation of ϕ_F

The analysis was based on data from the years 2019 and 2020. Three steps were made to explore the behaviour of ϕ_F along the spatial and

temporal dimensions. First, a pixel-averaged map of global yearly ϕ_F was made for the year 2019. Second, to verify that the ϕ_F indeed represents effects that are unrelated to canopy-greenness, the pixel-based Pearson's correlation coefficient betweenϕ_F and NDVI was calculated for the year 2019. Third, to visualize the effect of a drought stress on large-scale ϕ_F, a ϕ_F map of Western Europe was made before and during the 2019 European Summer Drought (Blauhut et al., 2022).

Evaluating the effect of SM and VPD in a phase space

As a next step, we analyse the effect of the environmental variables SM and VPD on ϕ_F by plotting each observation of ϕ_F values in function of its corresponding VPD and SM observations in a phase space. While plant drought stress is a complex and multi-dimensional problem, SM and VPD represent respectively the supply and demand of water. Each point in the phase space considers a specific set of environmental conditions, i.e., a VPD-SM combination, and shows the average ϕ_F value for these conditions. The observed ϕ_F values over the years 2019 and 2020 were binned based on both their SM (55 bins, between 0 and 0.55 m^3/m^3, bin width 0.01 m^3/m^3) and VPD (40 bins, between 1 and 5 kPa, bin width 0.1 kPa). To ensure statistical representativeness, SM-VPD bins that contained fewer than 1200 measurements were removed. Within the phase space, contour lines connect points of equal ϕ_F. The shape of these lines qualitatively reveals the controlling factor on ϕ_F . The analysis itself is done in three steps. In a first instance, a global average of the relationship between SM-VPD and ϕ_F is made through a phase space. The global analysis has the advantage of containing a maximal number of observations, but it neglects spatial variations in the response of ϕ_F to SM and VPD. In a second and third instance, the respective effects of the soil and vegetation are considered. The soil effects are characterized by the soil moisture content at (i) field capacity, which is a function of the soil texture and structure. The main vegetation effects are evaluated with (i) the landcover and with (ii) the degree of anisohydricity.

Data stratification of the global ϕ_F dataset with land cover, isohydricity and soil moisture at field capacity

Mechanistically linked to photosynthesis, plant-scale ϕ_F is sensitive to plant isohydricity (Attia et al., 2015; Cocozza et al., 2016), although the precise relationship at ecosystem scale is unclear. The global ϕ_F dataset was stratified based on the degree of anisohydricity of each pixel (Table 4.2) using a global database of isohydricity from (Konings and Gentine, 2017). This dataset quantifies an ecosystem's isohydricity based on the diurnal variation on satellite AMSR-E observations of X-band Vegetation Optical Depth (VOD), a proxy for the water potential in the leaves. This variation is quantified as the slope (σ) of the linear regression between daytime and night-time VOD. Pixels showing little σ values ($\sigma \sim 0$) were considered as more isohydric, meaning they have a strict stomatal control, therefore low diurnal VOD variation. Pixels with s values close to 1 were instead considered more anisohydric. Those pixels typically have higher daily transpiration rates, and therefore a larger difference between daytime and nighttime VOD (Konings and Gentine, 2017). While some ecosystems are reported to have a seasonality in their degree of anisohydricity, driven by leaf phenology (Gong et al., 2022), or due to species turnover (Wu et al., 2021). Studying time-variable effects of isohydricity is beyond the scope of this study. To assess the effect of isohydricity and anisohydricity on the ϕ_F under different SM and VPD conditions, we split ecosystem-scale isohydricity into 6 discrete classes.

In addition to the isohydricity effect, the effects of land management were studied. To do so, croplands were treated distinctly from other vegetation types as they typically show a clear anisohydric behaviour and farming practices allow agricultural crops to grow optimally, with high photosynthetic rates. Such management practices are not present in natural ecosystems. The vegetation type information come from the International Geosphere–Biosphere Programme (Friedl et al., 2010) land cover classification information. As a third explanatory effect, we stratified the global dataset along its soil moisture value at field capacity, taken from OpenLandMap Hengl and Gupta (2019). The latter is key parameter in the soil water retention. Both the isohydricity and the land cover analysis were carried out on the global dataset.

Table 4.2: Isohydricity classes, based on the slope between midday and midnight vegetation optical depth σ (Konings and Gentine, 2017).

Strictly Isohydric	**Isohydric**	**Rather Isohydric**	**Rather Anisohydric**	**Anisohydric**	**Strictly Anisohydric**
0—0.2	0.2—0.4	0.4—0.6	0.6—0.8	0.8—1	1—1.2

4.2.3 Modelling Gs at the continental scale

SM and VPD affect the ϕ_F through partially driving stomatal closure (Jonard et al., 2020), as closed stomata limit the plant's carboxylation rate. This sensitivity is tested by comparing ϕ_F observations to Gs model estimates. The Gs data are obtained with a soil-plant hydraulic model, originally designed by (Carminati and Javaux, 2020) and expanded by (Wankmüller and Carminati, 2021). Here we feed the model remote sensing observations of SM and VPD (Table 4.1) as inputs to predict Gs for Africa. Limiting the scope of the analysis to the African continent reduces the computation time to a manageable amount, while still analysing a large diversity of different biomes and climates. Due to the coarse input datasets and the computationally expensive nature of the model, we estimate Gs at 36 km gridding. The soil plant hydraulic model operates under the steady-state assumption, i.e., all water fluxes equalize between soil and plant compartments. Water flow between soil and plant follows from the water potential difference between compartments and the compartment conductance. The decrease of soil conductance as a result of root water uptake is nonlinear and can quickly limit the conductance of the whole soil-plant system in dry conditions, which might exert strong control on stomatal response (Carminati and Javaux, 2020). The model setup does not prescribe species-specific traits or levels of isohydricity. The relationship of Gs to SM and VPD is resulting from the modelś soil and plant hydraulics and the local SM and VPD time series. Our goal is to provide a simple comparison between observations of SM and VPD control on ϕ_F and plant hydraulics-based SM and VPD control on Gs. We do not attempt to provide and optimal fit between model and observations but interpret differences in relation mechanism not represented in the model.

The driving force for water flow from the soil to the leaves is the water potential difference. The plant regulates this water flow rate by adjusting the resistance on this path. This resistance is controlled by the stomata, the opening of which is controlled with the phytohormone abscisic acid (ABA) (Grantz et al., 2019; Pantin et al., 2013). The production of ABA depends on the plant water status, as well as on its photosynthetic activity. Wankmüller and Carminati (2021) described the effect of the stomatal/canopy conductance on the plant hydraulic model conductance. The relative level of ABA (-) follows from a sink-source equation (Eq. 4.7):

$$|ABA| \propto \frac{-\Psi_{\text{leaf}} + \delta\Psi}{A + \delta_A} \tag{4.7}$$

where the source term in the numerator depends on the leaf water potential Ψ_{leaf} (MPa) and a constant minimum production rate δ_Ψ (MPa). The sink term in the denominator depends on an assimilation rate A and a constant minimum degradation rate δ_A (μmol $m^{-2}s^{-1}$) . The ABA dynamics drive the Gs dynamics, that determine the photosynthetic rate, by determining the inflow of CO_2 trough the stomata. Because of the steady-state assumption, the assimilation rate A μmol $m^{-2}s^{-1}$ is modelled as a function of stomatal conductance and a saturation curve (Eq. 4.8:)

$$\mathrm{A}\left(\mathrm{G_S}\right) = \frac{\frac{\mathrm{G_S}}{1.6}\mathrm{A_{max}}}{\frac{\mathrm{G_S}}{1.6} + \mathrm{K_M}} \tag{4.8}$$

where $\mathrm{A_{max}}$ (μmol $m^{-2}s^{-1}$) is the maximum assimilation rate and K_M(μmol $m^{-2}s^{-1}$) is the Michaelis-Menten constant. Traditionally, $\mathrm{G_S}$ (μmol $m^{-2}s^{-1}$) linked to the transpiration rate using the following simple model (Medlyn et al., 2011):

$$\mathrm{G_S} = \mathrm{TA_{leaf}} \frac{\mathrm{P_{atm}}}{\mathrm{VPD}} \tag{4.9}$$

where $\mathrm{TA_{leaf}}$ is the transpiration rate, $\mathrm{P_{atm}}$ the atmospheric pressure and VPD the vapour pressure deficit. The transpiration rate $\mathrm{TA_{leaf}}$ is estimated in the function of the leaf area index, as well as on the differences in soil and leaf water potential, multiplied by the plant hydraulic

resistance (see Wankmüller and Carminati (2021) for the precise equations). The ABA dynamics play a role in the value of plant resistance. This way, equations 4.7 to 4.9 are all linked to each other, as any change in any of the variables in any of these equations inevitably leads to a change in all the other variables. Specifically, this means that the stomata open progressively, increasing Gs, as the |ABA| decreases (positive feedback mechanism), until the |ABA| reaches a local minimum, corresponding to a local minimum in Eq. 4.7. The latter solution results in a steady-state Gs. This minimum is found with an optimization procedure over the leaf-level transpiration rate.

Here we use remote sensing observations of SM and VPD as inputs to predict Gs for Africa. We parameterize root length as time-static but variable between locations based on MODIS LAI. MODIS LAI is taken from MCD15A2H Terra/Aqua MODIS 8-day composites (Myneri et al., 2015). We include variable Brooks-Corey soil parameters based on empirical equations by Rawls and Brakensiek (1985) and information on soil type, bulk density as well as residual and field capacity water content from OpenLandMap (Hengl and Gupta, 2019) (Table 4.3).

Table 4.3: Parametrization of the Gs model.

Parameter name	**Parameter**	**Parameter Value**	**Unit**
Maximum assimilation rate	A_{max}	38	μmol m^{-2} s^{-1}
Minimum degradation of ABA	ϵ_A	1	μmol m^{-2}s^{-1}
Minimum production of ABA	ϵ_ψ	2	MPa
Michaelis-Menten constant	K_M	150	mmol m^{-2}s^{-1}
Atmospheric pressure	P$_{atm}$	100	kPa

We refer to (Carminati and Javaux, 2020) and (Wankmüller and Carminati, 2021) for a more detailed description of the model framework and provide our exact parameterization in the supplement. Despite of the expected effect of the isohydricity on Gs, the model does not consider isohydricity. Neither does the model framework does not include any functional dependence of Gs on light availability or temperature, which should limit the ability of the model to capture Gs dynamics in very humid areas.

4.3 Results

4.3.1 Global patterns of ϕ_F

Figure 4.1 shows the global average ϕ_F for 2019 at 9 km resolution. Regions that typically show a clear moisture gradient, such as the Sahel region or Northern Australia, tend to show a gradient in ϕ_F. Western Europe, India, Brazil, Tropical Africa and Southeast Asia show high values of ϕ_F.

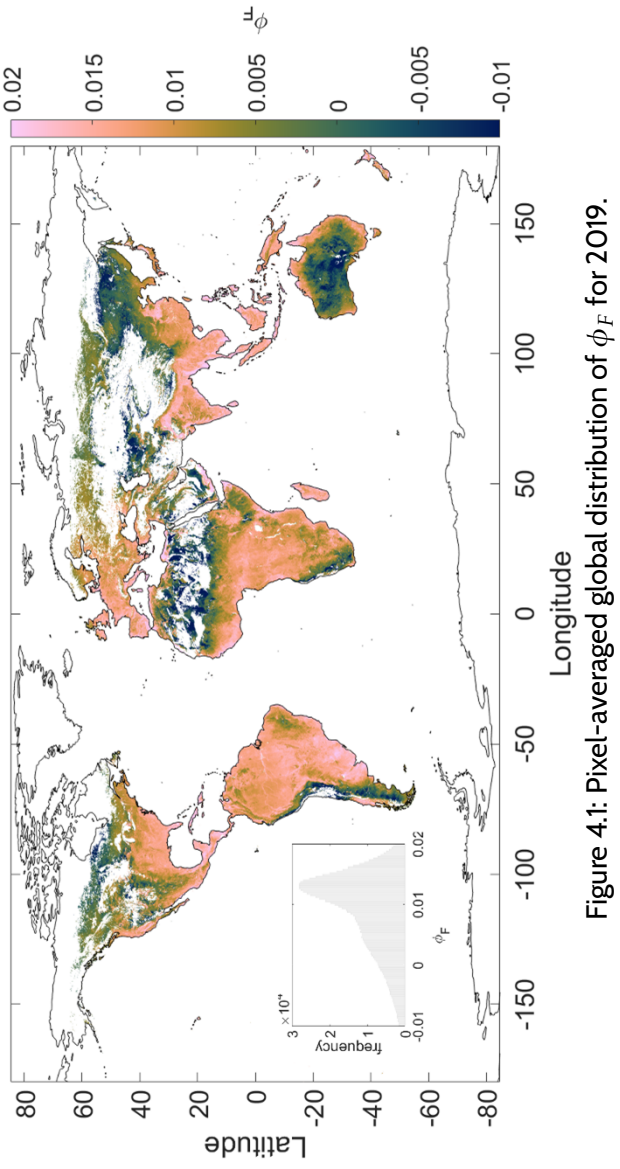


Figure 4.1: Pixel-averaged global distribution of ϕ_F for 2019.

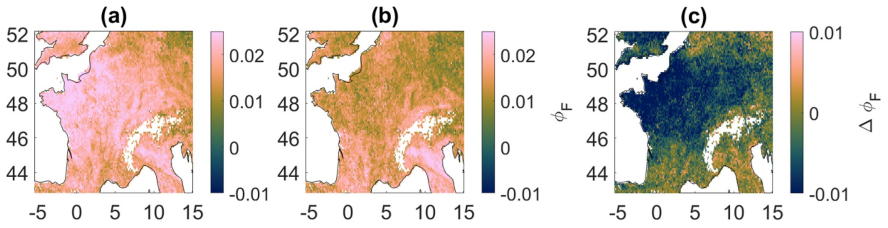


Figure 4.2: (a) Spatial overview of the average ϕ_F for June 1^{st}-June 11^{th} (b) Spatial overview of the average ϕ_F for June 25^{th}-July 5^{th}, the 2019 European heatwave; (c) difference in ϕ_F between Figures (a) and (b).

In addition to the spatial patterns, the ϕ_F also shows reactivity to disturbances, that typically reduce the ϕ_F. This concept is illustrated by Figure 4.2, which shows the ϕ_F over Western Europe during a regular 2019 spring (Figure 4.2a) and the First European heatwave 2019 (Figure 4.2b) in Western Europe (Blauhut et al., 2022). The map shows a clear decrease in ϕ_F in France and Southern Germany (Figure 4.2c).

Figure 4.3 shows the pixel-based Pearson's correlation coefficient between NDVI and ϕ_F ($\rho_{\phi_F\text{-NDVI}}$) for 2019. Spatially, regions with a high ϕ_F-NDVI correlation tend to concentrate in regions that have either a semi-arid climate, such as the Sahel, or that are situated at high latitudes, such as Siberia or Canada. The histogram of the correlation coefficient shows a clear peak around 0, indicating that the ϕ_F is unrelated to the NDVI for most pixels.

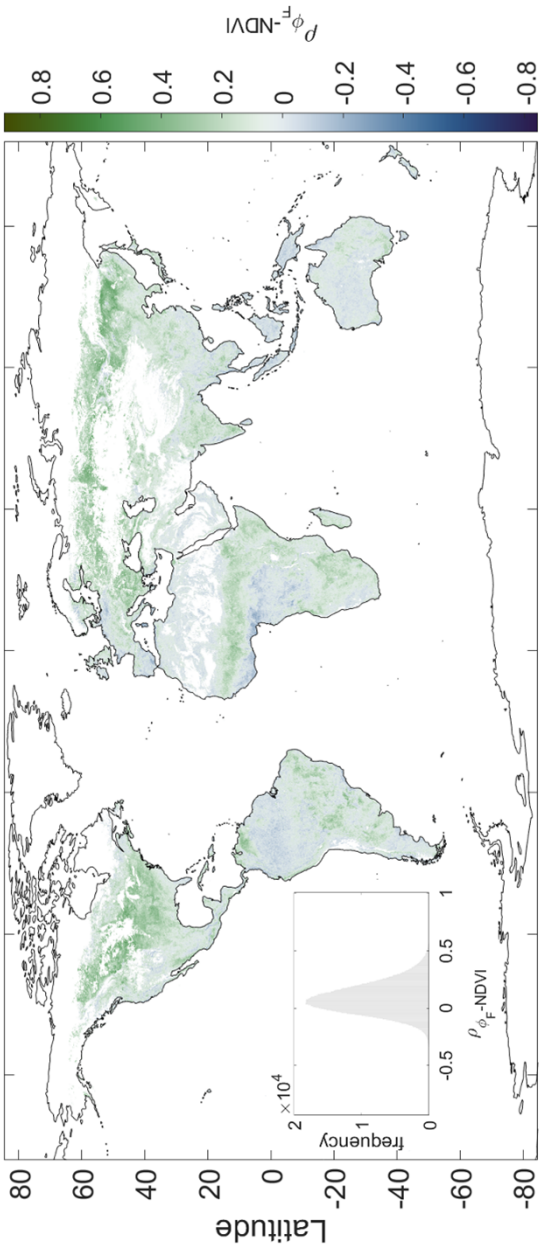


Figure 4.3: Global map of the ϕ_F-NDVI based Pearson's correlation coefficient for 2019.

4.3.2 Observed control of SM and VPD on ϕ_F

Figure 4.4 shows the global ϕ_F as a function of the SM and VPD. The highest ϕ_F values are found in the VPD range between 2 and 3 kPa. For the region with VPD < 1.8 kPa, the horizontal contour lines indicate that VPD is the only driving factor for the ϕ_F. For the region with VPD > 1.8 kPa, the more curved and diagonal contour lines indicate a co-regulation of ϕ_F by SM and VPD, especially for VPD > 2.5 kPa. Figure 4.12 shows in another way that VPD is the main factor driving ϕ_F for the region VPD < 1.8 kPa. For higher VPD, a decrease in soil moisture leads to a decrease in ϕ_F.

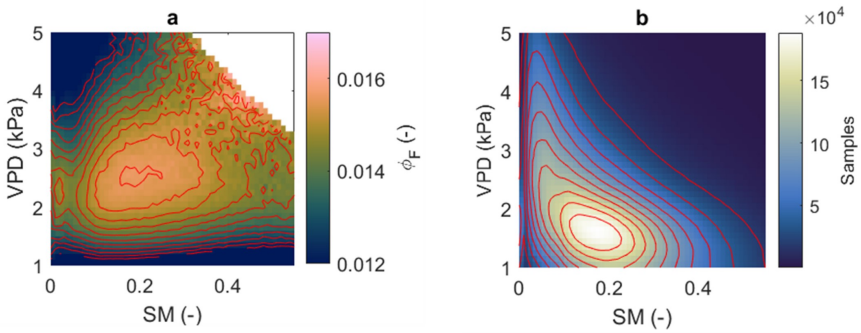


Figure 4.4: (a) phase space showing the average ϕ_F for each SM-VPD combination that emerged from a global analysis during the years 2019 and 2020. The red lines denote contour lines of regions of equal ϕ_F values. (b) Number of samples for each SM-VPD combination.

4.3.3 Isohydricity modulates control of SM and VPD on ϕ_F

Figure 4.5 shows the ϕ_F values in function of both the SM and VPD conditions along the isohydricity strata. All the subplots replicate the global behaviour, with maximal ϕ_F values found in the region of VPD between 2 and 3 kPa, albeit with a variability in function of biotic and environmental ecosystem characteristics. In most isohydricity classes (isohydricity > 0.2), only a slight isohydricity effect was observed. In contrast, in the two most anisohydric categories (isohydricity < 0.2), the ϕ_F values were notably higher than in the more isohydric classes. In the most anisohydric class, the ϕ_F was almost completely decoupled from the water availability, with a decrease in ϕ_F only setting in when the SM values approach to 0.

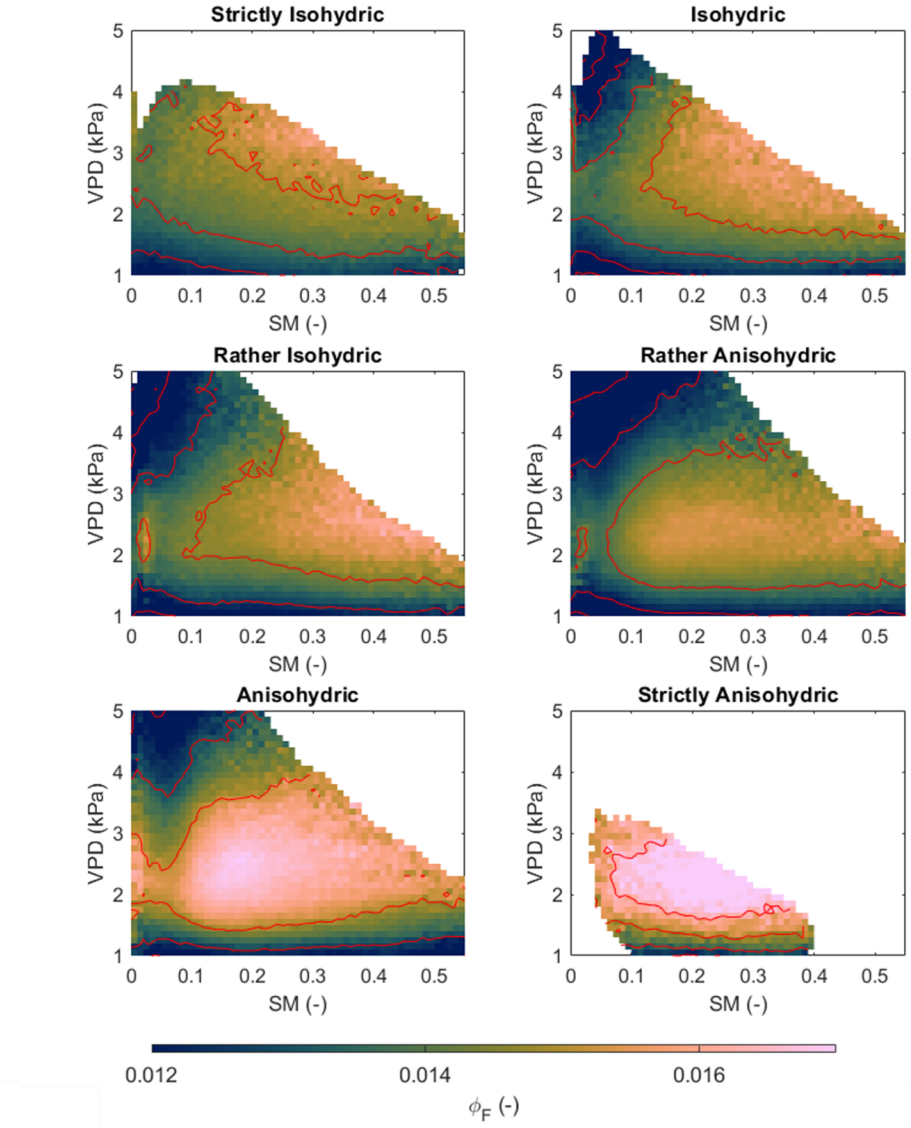


Figure 4.5: Phase spaces of the ϕ_F values along the SM-VPD space for six different isohydricity classes.

Figure 4.6 shows the effect of increasing VPD on the ϕ_F under ranges of averaged soil moisture conditions for the different isohydricity classes. The figure shows a very clear difference in the ϕ_F emission for the VPD range between 1 and 3 kPa. For VPD > 2.5 kPa, the ϕ_F tends to decrease in response to a higher VPD. Consistent with Figure 4.5, there is an increasing trend of ϕ_F with increasing isohydricity, and very anisohydric regions show the highest ϕ_F values, especially for VPD above 1 kPa. It is worth noting that the more isohydric ecosystems show a higher ϕ_F at VPD < 0.8 kPa. For the lower SM classes, the isohydricity effect on ϕ_F is more notable, as the two more anisohydric lines clearly show the highest ϕ_F value in the plot with the lowest soil moisture in the region with VPD > 0.8 kPa. In contrast, the plot with SM > 0.45 m^3/m^3 shows that the isohydricity almost plays no effect on ϕ_F, except for the most anisohydric category.

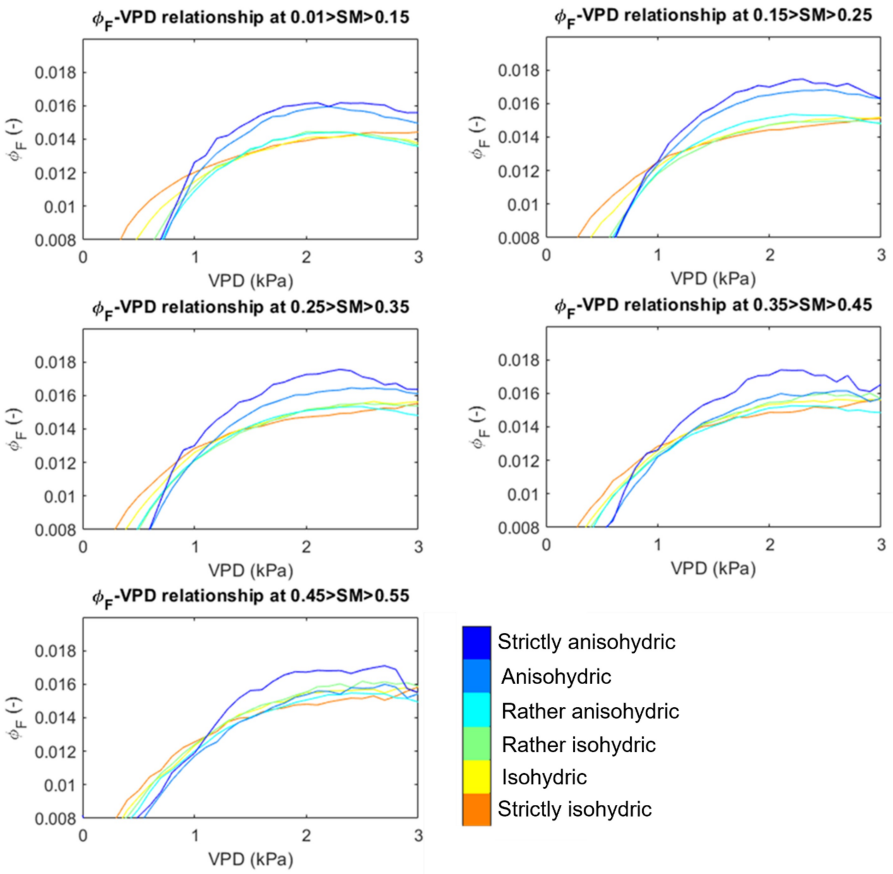


Figure 4.6: ϕ_F-VPD relationship at different soil moisture condition ranges and isohydricity classes. Values for VPD > 3 kPa were not shown, as there were too few observations in this class.

Croplands tend to behave differently in their SM-VPD space compared to other vegetation (Figure 4.7). As a main difference, the croplands show higher ϕ_F values compared to the non-croplands, while the shape of the contour lines does not change significantly. It should be noted that the cropland vegetation contains a higher proportion of more anisohydric pixels (mean of 0.4 for non-croplands, mean of 0.2 for croplands, Figure 4.13).

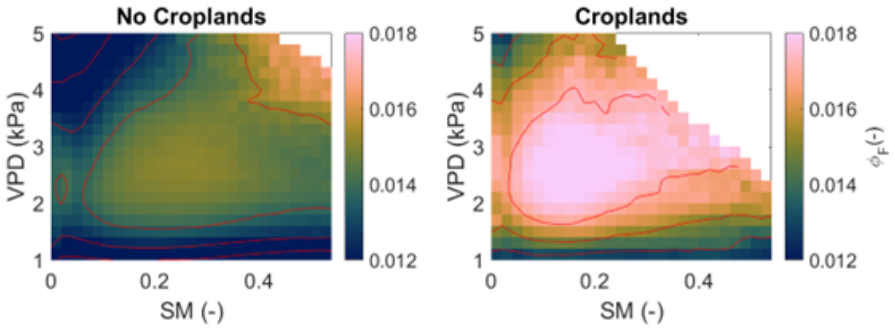


Figure 4.7: Phase space of ϕ_F along the SM-VPD space for croplands and non-croplands (i.e., other vegetation types that are not croplands).

4.3.4 Effect soil water retention characteristics on the control of SM and VPD on ϕ_F

Depending on the soil physical characteristics, mainly the soil texture, soil water can be more or less available to a plant. The soil moisture retention characteristics do not affect the relationship between VPD and ϕ_F. However, they do change the control of SM on ϕ_F. A remarkable behaviour is found in the category of soils that already reach field capacity below an SM of 0.1 (Figure 4.8). Such soils reach a maximal ϕ_F at very low SM values, with a subsequent decrease. Moving to the categories that have a higher SM at field capacity, a double effect can be seen. First: the gradual decrease of ϕ_F at high SM values disappears. Second, the zone of maximal ϕ_F gradually moves to a higher SM region.

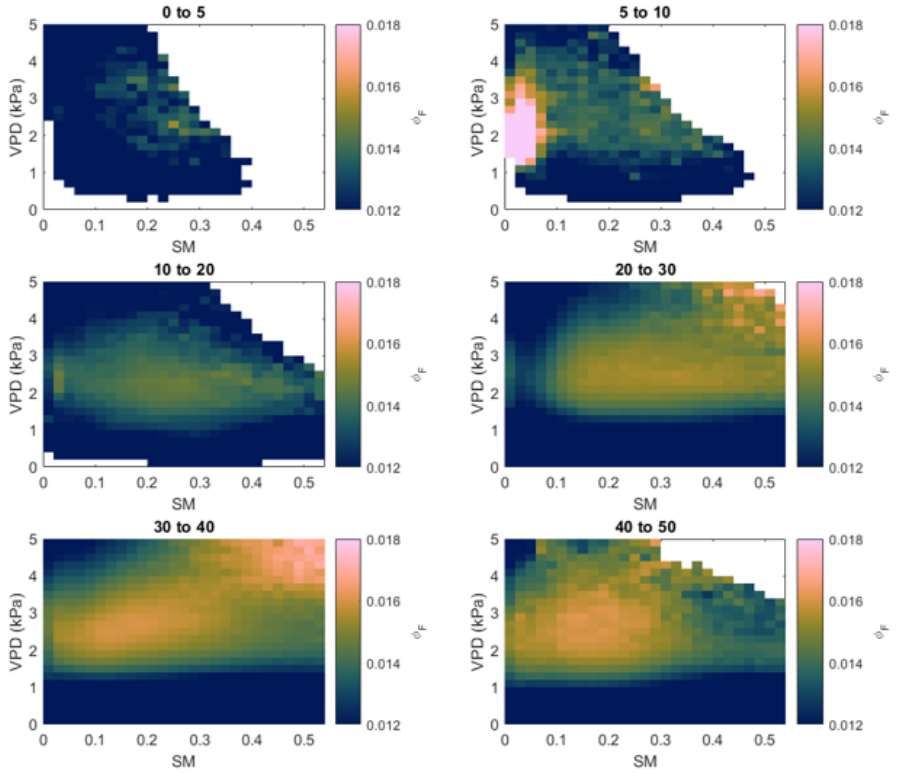


Figure 4.8: Phase space of ϕ_F along the SM-VPD space stratified along the soil moisture at field capacity. The titles refer to the lower and upper-bound soil moisture at field capacity (in percentage) for each category.

4.3.5 Linking ϕ_F to canopy conductance

Figure 4.9 shows the tile and contour plots of ϕ_F and Gs. The main similarity between the ϕ_F and Gs phase space is that they both decrease with decreasing SM conditions, but the ϕ_F decreases are less steep compared to the Gs decrease. Overall, both show a similar VPD-dominated regime at high SM and a co-regulated regime at low SM. For SM < 0.15 m^3/m^3, the Gs lines are close to vertical along the entire VPD range. This behaviour is not replicated by the ϕ_F data. ϕ_F at low SM might pick up adapted dryland vegetation, which is not rep-

resented in the trait-less model. For the low VPD range, modelled Gs does not increase with VPD, which is likely due to the limitation that Gs is only driven by water limitation (i.e., SM and VPD) but is not an explicit function of temperature or light.

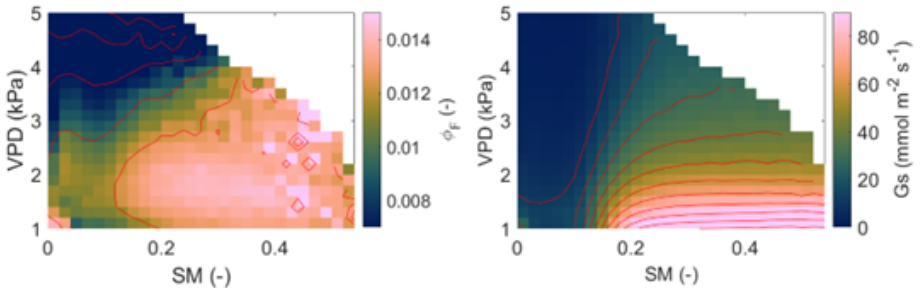


Figure 4.9: ϕ_F (left) and Gs (right) values over the African continent during 2019-2020 in the SM-VPD phase space. The ϕ_F dataset was re-gridded to 36 km before being put in the phase space. The minimal threshold for an SM-VPD combination to be included in the plot was at 120 samples.

Leaf-scale observations on fluorescence yield and stomatal conductance have shown a concave relationship, in which the ϕ_F approaches a maximal value for high Gs values. The ϕ_F-Gs curve showed a concave relationship (e.g., Flexas et al., 2002). The same behaviour is replicated in Figure 4.10, despite of being made at the continental scale. When looking at the map of the pixel-based correlation of ϕ_F and Gs (Figure 4.11), the strongest correlation between Gs and ϕ_F is found in the Sahel region as well as in East Africa, but overall observed ϕ_F and modelled Gs show reasonably high correlations in most water limited areas. A low and negative correlation between ϕ_F and Gs can be found in some parts of the Ethiopian Highlands as well as in the Congolese Rainforest.

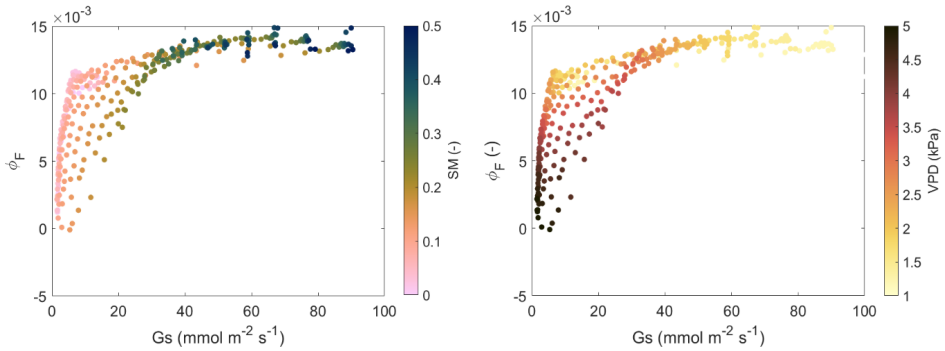


Figure 4.10: ϕ_F values from the SM-VPD space over the African continent during 2019-2020 (Figure 4.9) plotted in function of the Gs value and SM (left) or VPD (right) in the colourbar. Each dot represents the ϕ_F average over the considered SM-VPD bin.

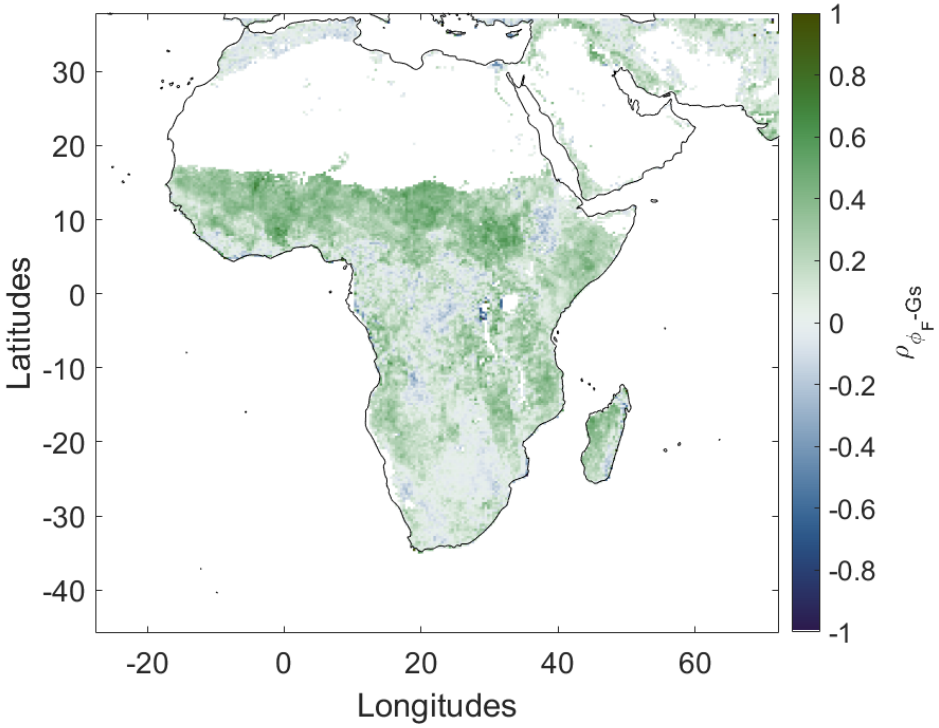


Figure 4.11: Pixel-based correlation between Gs and ϕ_F over Africa during the years 2019 and 2020. Data points with a VPD < 1.5 kPa were excluded from the analysis, as ϕ_F and Gs are de-coupled for low VPD values

4.4 Discussion

4.4.1 Interpretation of spatial patterns in global ϕ_F data

The different phase spaces (Fig. 4.4-4.8) show that the ϕ_F is sensitive to the soil, plant and atmospheric characteristics. These sensitivities are consistent with the spatial gradients of ϕ_F that appear in figure 4.1. Clear examples here are the increase in ϕ_F over the Sahel region or in the Australian Outback, where the ϕ_F decreases gradually when entering the desert zone. In addition, in some mountain areas such as those in the Western United States, ϕ_F is lower because high altitude regions tend to show a lower photosynthetic activity (Fujimura et al., 2010). Low ϕ_F values are mainly found in regions with either sparse vegetation, like the Australian Outback, or low irradiations, such as Siberia. In such regions, a low SIF value is also expected.

The low correlation coefficient between NDVI and ϕ_F (figure 4.3) shows that ϕ_F and NDVI are fundamentally different, strengthening the case that satellite-based ϕ_F indeed represents the physiological component of the SIF emission independently of vegetation greenness. Figure 4.3 shows only two situations in which NDVI and ϕ_F tend to be correlated. The first is in regions with high latitudes. There, high VPD values are rare, so ϕ_F tends to show a seasonality with high ϕ_F in summer and lower in winter, which is similar to the typical NDVI seasonality. Both are driven by limitations in temperature and irradiation which are found at high latitudes. The second situation where NDVI and ϕ_F show a high correlation is in regions where plants tend to shed or brown their leaves in the dry season, such as the Sahel region (Tagesson et al., 2015). Furthermore, regions where Jonard et al. (2022) identified a strong coupling between light availability and sun-induced chlorophyll fluorescence tended to show a high ϕ_F-NDVI correlation coefficient.

4.4.2 Landscape-scale interpretation of ϕ_F

Constraining effect of SM and VPD on ϕ_F at the landscape scale

While SIF data have proven their ability to detect drought stress, especially drought onset, at the regional to global scales (e.g., Cao et al., 2021; Sun et al., 2015), the contribution of the physiological component to this reaction has been subject to debate. Some studies suggest

that the SIF variability is induced by variation in escape probability $f_{esc,}$ which dwarfs the variability induced by the ϕ_F (Dechant et al., 2020; Ryu et al., 2019; Yang and van der Tol, 2018). Local-scale studies have reported a short-term variation in f_{esc} as a result of changes in leaf turgor (Xu et al., 2021) or due to wind effects (Liu et al., 2020). In addition, prolonged stress leads to a lowered NDVI, an effect that persists after the stress period (Wong et al., 2021), which provides an additional difficulty in interpreting SIF data. Working on ϕ_F comes with the advantage that it is stripped of non-physiological effects.

Acknowledging the importance of the structural changes on the escape probability, regional-scale studies using satellite-based SIF data have shown that variation in ϕ_F has its value in drought monitoring, thanks to its sensitivity to the efficiency of the photosynthetic apparatus (Gu et al., 2023; Kimm et al., 2021b). In the latter studies, the reaction of ϕ_F to a drought is shown in a way similar to Figure 4.2. A quantitative analysis of the effect of a dry soil and a high vapour pressure deficit on photosynthesis shows a reduction on photosynthetic activity under high VPD or low SM (Sulman et al., 2016). The phase spaces in our study show a similar decrease in ϕ_F with the decrease in SM or the increase in VPD. This suggests that ϕ_F bears the potential of being a tool for quantitatively evaluating the plant hydraulic functioning.

The changes in ϕ_F according to SM and VPD variability are similar to those occurring in Gs, as shown in Figure 4.9. This suggests that the link between Gs and ϕ_F, as described at the leaf scale (Flexas et al., 2002) or at the canopy scale (Kimm et al., 2021a) holds to the landscape scale. Gs is known to be constrained by a combination of SM and VPD, both at the ecosystem (Novick et al., 2019) and the local level (Zhang et al., 2021). A similar result is obtained for photosynthesis as such (Fu et al., 2022). This result is consistent with the concept of light- and water-limitation in ecosystem-scale photosynthesis (Jonard et al., 2022), since water limitation is assumed to induce a reduction in Gs through stomatal closure. As low irradiation values typically go together with low VPD values, the increase in ϕ_F at low VPD is likely an irradiation or a temperature effect.

While lab- and local- scale studies traditionally consider SM and VPD as two independent variables, there is a significant landscape-scale interaction between SM and VPD, as a high VPD (i.e., dry air) tends to dry out the soil (Liu et al., 2020), and dry/wet soils have also

the capacity to reinforce dry/wet atmospheric conditions. These interactions explain why some SM-VPD combinations are more frequent than others, and why the high SM-high VPD combination is so rare (Figure 4.4b). In this sense, the co-regulation of SM and VPD on ϕ_F, reported in Figure 4.4, can also represent a downstream effect of the dry air drying out the soil, or vice-versa. Determining whether SM or VPD (water availability or atmospheric water demand) is the main driving factor on the changes in ϕ_F would require further assessment on how SM and VPD are interrelated both in space and time (Feldman et al., 2020).

While the satellite-based ϕ_F data and the modelled Gs provide one single value for large areas, local-scale studies have reported significant within-field and within-plant variability of ϕ_F or SIF emission. This high degree of spatial variability finds its origins in spatial differences in stress and irradiation conditions (Pinto et al., 2016; Wieneke et al., 2016; Zeng et al., 2022). In addition to small-scale spatial variations in environmental factors, plants can have different biotic traits such as isohydricity and heat resistance. Both show a variation at the level of the individual plant (Bussotti et al., 2020; Pinto et al., 2016; Wu et al., 2020). The high sensitivity of ϕ_F to subtle changes in environmental conditions can explain the high degree of spatial ϕ_F variability observed in Figure 4.2, as differences in elevation, micro-meteorology or soil composition might change the local stressors. The high spatial variability in ϕ_F is a major hurdle in upscaling ϕ_F to the landscape scale.

Role of non-photochemical quenching at the landscape scale

The most direct way to establish a link between ϕ_F and Gs is to make leaf-scale measurements with a fluorometer and a leaf chamber. A milestone study in this regard was Flexas et al. (2002), that observed a concave relationship between ϕ_F and Gs, where ϕ_F, as well as the photosynthetic rate, decrease with decreasing Gs. In the presented study, a similarly concave curve was found between TROPOMI ϕ_F and modelled Gs (figure 4.11). Helm et al. (2020) expanded this idea by comparing leaf-scale spectrometer SIF measurements with stomatal conductance measurements, and they found a similar connection between ϕ_F and Gs. Both studies attribute the decrease in ϕ_F or SIF to an observed

increase in NPQ. While it makes sense to believe that the increase in NPQ is also responsible for the decrease of satellite-based ϕ_F at the landscape scale, it is impractical to verify this claim, as there is currently no reliable method for estimating NPQ from a remote sensing platform. The closest we have to a remote-sensing based NPQ estimate comes from the PRI. Short-term PRI dynamics are closely linked to NPQ dynamics. Using airborne imagery over an orchard, Zarco-Tejada et al. (2012) observed a simultaneous decrease in SIF, PRI and Gs, strengthening the case that the drought-induced decrease in canopy-scale SIF is indeed driven by a decrease in Gs and an increase in NPQ. While the link between NPQ and ϕ_F at the landscape scale remains in a speculative sphere, it is important to consider NPQ in the interpretation of ϕ_F under water-limited conditions, since the NPQ component forms a key element in linking ϕ_F to ecosystem-scale photosynthesis (Lee et al., 2015; Qiu et al., 2018).

4.4.3 The position of ϕ_F in the landscape of remote sensing signals

Optical remote sensing measures mainly the greenness and near-infrared signatures of the vegetation, which then is linked to vegetation health since a lack of vegetation growth as the result of a prolonged soil moisture deficit is impacting the canopy greenness. However, these techniques fail to capture the drought effects at shorter timescales. To do so, a variable that reacts instantly and proportionally to stress intensity is imperative. Along with ϕ_F measurements, two other techniques are indicative of environmental constraints on photosynthesis. These are the photochemical reflectance index (PRI) that is sensitive to the NPQ component in PSII and indicators that make use of thermal remote sensing. PRI is driven by the stress-induced increase in ϕ_N, making its driving factors similar to the factors driving ϕ_F (Acebron et al., 2021; Alonso et al., 2017). However, the interpretation of the PRI is blurred by the presence of bare soil or by the canopy structure (Yang, 2022). Synergetic use of PRI and ϕ_F data is expected to lead to a better description of the energy splitting at the level of PSII. Thermal remote sensing-based stress detection relies on the decrease in latent heat flux over the leaves because of reduced gas exchange. The reduction in the latent heat flux leads to an increase in the sensible heat flux and thus in an increase in leaf temperature (Maes and Steppe, 2012). This effect

can be used to constrain the plant resistances, which allows for better modelling of the plant water and carbon fluxes (Bayat et al., 2018). Another thermal-based technique is the crop water stress index (CWSI), which compares the measured canopy temperature to a wet and dry reference (Berger et al., 2022). These variables are notoriously hard to measure, resulting in significant errors over global CWSI-based stress monitoring.

From this perspective, global ϕ_F is a promising variable that is linked in a more physiologically established way to Gs, reducing the need for ancillary data in its interpretation. Specifically, ϕ_F is mechanistically coupled to the PSII activity, allowing ϕ_F to constrain photosystem activity-related parameters in photosynthesis models. However, this comes at the cost of very strict spectral retrieval requirements. Consequently, ϕ_F comes with a coarse spatial resolution and significant instrument noise.

4.4.4 Consistent behaviour of ϕ_F and Gs at the landscape scale

Since ϕ_F carries an imprint of SM and VPD, ϕ_F is a promising variable for constraining photosynthetic activity at the landscape scale. At the leaf level, ϕ_F is mechanistically coupled to the PSII activity, allowing ϕ_F to constrain photosystem activity-related parameters in photosynthesis models. The consistency between the concave shape in figure 4.11 and the shape obtained by the leaf-scale study of Flexas et al. (2002) and by the regional-scale study of Kimm et al. (2021b) suggest that the knowledge from the leaf scale on the link between Gs and ϕ_F pave the way for a solid ecosystem-scale link between ϕ_F and photosynthesis under water limitation. There are various hurdles to take before mechanistic-based land surface models can exploit this link. The first hurdle is linked to the strict spectral requirements for SIF retrieval and the instrument noise. The second hurdle deals with the upscaling of the link between ϕ_F, NPQ and photosynthesis, as stipulated in chapter 3 to the landscape scale. Given the link between photosynthesis and crop yield, satellite-based SIF has already improved the crop yield predictions (Guanter et al., 2014). Further exploring the link between ϕ_F, photosynthesis and crop yield will improve the estimations of crop yield under water-limited conditions.

4.4.5 Perspectives for the FLuorescence EXplorer (FLEX) mission

While the TROPOSIF data are encouraging for presenting SIF's ability to detect environmental constraints on photosynthesis, the first satellite designated for SIF measurements is scheduled for launch in 2025. The Fluorescence Imaging Spectrometer (FLORIS) instrument on the FLEX satellite is planned to come with two main improvements: a finer spatial resolution and a higher signal-to-noise ratio. Additionally, FLEX data will be evaluated with the help of ground-based calibration-validation dataset, which is expected to help the interpretation of the FLEX data, providing an absolute ϕ_F scale. The spatial footprint of FLEX is in the same order of magnitude as the footprint of eddy covariance towers, allowing for a fairer comparison of spaceborne ϕ_F and eddy covariance estimates of Gs. A better characterization of this link will help to improve global estimates of photosynthesis and transpiration. However, the main advantage of the TROPOSIF product compared to the upcoming FLEX data is the higher temporal resolution of TROPOMI. A synergetic interpretation of both datasets might allow for ϕ_F and Gs estimations that are both accurate and frequent.

4.5 Conclusion

While a well-established variable in laboratory-scale experiments, the fluorescence yield (ϕ_F) retrieved from remote sensing platforms is a newly established variable. Mechanistically linked to the photosynthetic efficiency, ϕ_F is promising for large-scale monitoring of vegetation status. Here, ϕ_F has been retrieved at the global scale by normalizing the TROPOMI SIF data with the NIRvP, the latter accounting for the irradiation and canopy structure components of the signal. To gain insight into the environmental controls on the remotely sensed ϕ_F, the global ϕ_F data were set out in a phase space with remotely sensed vapour pressure deficit (VPD) and soil moisture (SM), from the AIRS and SMAP sensors, respectively. The observed global spatial patterns of ϕ_F show that these are responsive to limiting factors of photosynthesis, including water availability, solar irradiation or temperature, among others. Water availability and demand is described by the SM and VPD and drive ϕ_F variability. Consequently, ϕ_F shows a maximum at around intermediate soil moisture and VPD (i.e., 0.1 m^3/m^3 < SM <

0.3 m^3/m^3 and 1.5 kPa < VPD < 2.5 kPa). Results show that lower SM and/or higher VPD may lead to lowered stomatal conductance, lowering the ϕ_F, while lower VPD leads to energy limitation and higher SM leads to waterlogging. The effect of high VPD and low SM on ϕ_F is stronger for more isohydric ecosystems, as they exert stricter control over their photosynthetic activity in function of the environmental variables. On the other hand, more anisohydric ecosystems tend to have less strict control on their photosynthetic activity. The ecosystem-level link between Gs and ϕ_F is consistent with the link between these variables at the leaf scale. At the leaf scale, the increase in NPQ is an essential factor for linking Gs and ϕ_F. Despite of NPQ not being measurable from a remote sensing platform, it makes sense to believe that the NPQ is equally important to link ϕ_F and Gs at the landscape scale. Thanks to its sensitivity to VPD and SM, and carrying an imprint from Gs, ϕ_F is a very promising emerging remote sensing signal that is sensitive to the photosynthetic activity at the instant of the measurement. This contrasts with traditional, greenness-based indicators that reflect a stress legacy effect than the instantaneous stress itself. The FLEX satellite, scheduled for launch in 2025, is expected to be a game-changer, as it will retrieve ϕ_F at a finer spatial scale, a finer spectral resolution, and a higher signal-to-noise ratio. This opens the door for field-scale analyses and satellite-based modelling with ϕ_F.

4.6 Appendix

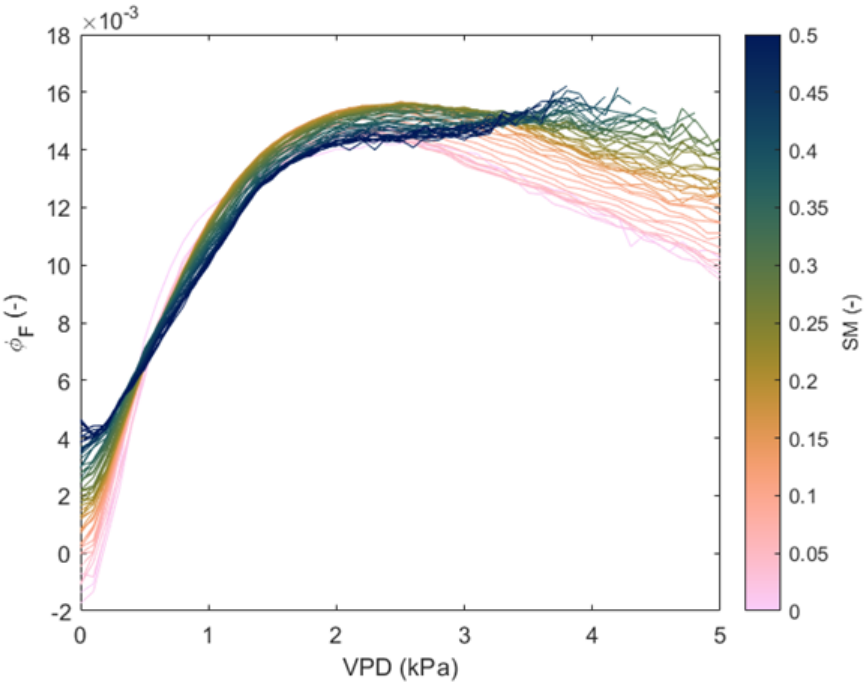


Figure 4.12: global ϕ_F-VPD relationship for different SM classes.

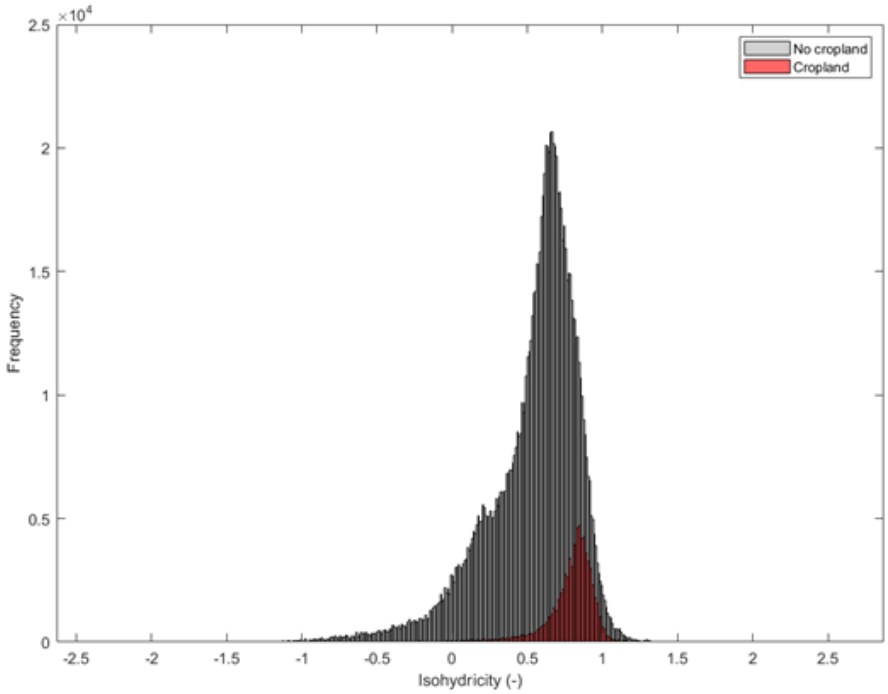


Figure 4.13: frequency of the isohydricity in for both the cropland and the non-cropland class.

Chapter 5

Conclusion and perspectives

5.1 Key findings

This thesis takes the remote sensing variable of SIF and looks at it through a plant physiological lens, with a keen interest in using it as a drought diagnostic. During a drought, a plant tends to close its stomata, saving up on its water use at the expense of a lowered CO_2 uptake, thereby lowering the energy demand by the Calvin cycle. Through a series of regulatory mechanisms, the energy harvested by the photosynthetic light reactions and energy consumed by the Calvin cycle are neatly equilibrated. Both the light supply and the CO_2 are highly dynamic variables and can change with even minor meteorological changes, such as a cloud overpass or a gust of wind. A physiologically based variable to measure the drought severity is the fluorescence yield ϕ_F. In order to retrieve ϕ_F from remote sensing data, a two-step approach is imperative. The first step deals with retrieving the sun-induced chlorophyll fluorescence (SIF), using methods that rely on Fraunhofer lines or oxygen absorption lines. In a second instance, SIF needs to be corrected for the photosynthetically active radiation (PAR), by the fraction of absorbed photosynthetically active radiation (fPAR), as well as the escape probability (f_{esc}). All three beforementioned factors show dynamics at the second's timescale, as each of them has a sensitivity to the meteorological conditions. The variable ϕ_F forms the

backbone of this thesis, since it is mechanistically linked to the plant physiology, and still retrievable through remote sensing. However, as the the retrieval relies on very narrow bands, a certain temporal (in Chapters 2 and 3) or spatial (in Chapter 4) aggregation was imperative for the sensor to capture enough energy to get a reliable signal. The thesis made advances in the observations and modeling of ϕ_F. Chapter 2 focussed on plant-level observations. It showed that plant level, the remotely sensed ϵ_{760}, conceptually similar to ϕ_F, decreased with decreasing soil moisture, on the condition that the PAR and VPD were high enough. The sensitivity observed in Chapter 2 suggested that the equations that linked ϕ_F to photosynthesis scaled from the photosystem to the canopy scale. The sensitivity is then is exploited to calibrate the Feddes water stress function in a crop growth model. The Feddes function establishes a link between soil moisture and a stress factor. This stress factor then controls the energy partitioning between ϕ_P, ϕ_N and ϕ_F. By introducing the stress factor $\overline{\alpha}$ in the calculation of K_N, and therefore of ϕ_N, the chapter comes up with a practical framework for calculating energy partitioning in photosystems under increasing stress conditions. Another interesting feature of the approach developed in Chapter 3 is that it calibrates the relationship between the stress factor $\overline{\alpha}$ and the environmental conditions, which leads to an improved estimation of the water and carbon fluxes. This is in contrast to methods that calculate the carbon and water fluxes based on SIF data in a more direct way. The advantage of the method proposed in Chapter 3 is that it only takes a few high-quality SIF measurements to improve the carbon and water flux estimations over the whole growing season. In many ways, the results of Chapter 4 are similar to the results of Chapter 2. Just like local-scale ϕ_F, global-scale ϕ_F is sensitive to SM and VPD at the moment of the measurement. Under low VPD conditions, photosynthesis is expected to be in an energy-limited regime. In such a regime, water availability is not the limiting factor on photosynthesis, and SM and fluorescence are therefore decoupled. From a certain VPD onwards, typically at around 1.8 kPa, energy is abundantly available, while the high evaporative demand by the atmosphere forces stomata to close. In such situations, water becomes a constraining factor for photosynthesis, and a clear ϕ_F-SM connection can be observed. The precise nature of the effect exerted by the environmental factors on ϕ_F is affected by the large-scale isohydricity.

Over the chapters, the findings boil down to the following key findings. First, the ϕ_F is sensitive to the plant drought conditions. Second, this sensitivity to drought conditions scales from the plant to the landscape scale. Third, plant-specific traits, such as isohydricity, play a major role in this link. Fourth, the mechanistic nature of the link between ϕ_F and photosynthesis allows it to serve as a proxy for stress severity, enabling it to calibrate a stress function. To do so, it is imperative to include a stress factor in the estimation of NPQ. Fifth, the ϕ_F reaction goes often together with a plant structural reaction.

5.2 Research Perspectives

5.2.1 Field-based research on the link between SIF and drought stress

While this thesis neatly described the behaviour of the conceptually similar variables of fluorescence emission efficiency at 760 nm (ϵ_{760}) and fluorescence yield (ϕ_F), it fails to integrate the SIFB. These data are harder to interpret, due to the shallower depth of the Telluric band at 687 nm, as well as due to reabsorption. The precise nature and intensity of the re-absorption is a function of the canopy structure. If the re-absorption problem were tackled, the shape of the fluorescence curve could be used to assess the contribution of each of the photosystems to the fluorescence signal, since the relative contribution of PSII is more important compared to PSI at the shorter wavelengths. In order to assess the reaction of the SIFB to increasing stress, a combination of in-situ measurements of leaf-scale SIFB, canopy-scale SIFB and in-situ measurements of the plant water status is necessary. A second research axis at the plant scale would be to link the fluorescence signal to other remote sensing indicators that are driven by stomatal closure. Two promising indicators here are the crop water stress index (CWSI), that is indicative of the increase in the sensible heat flux caused by the drop in stomatal closure, and the photochemical reflectance index (PRI), a narrow-band reflectance indicator indicative of the de-epoxidation state of xanthophyll (Chapter 2). A combination of PRI, CWSI and SIF can then be used to estimate the canopy conductance. Such an approach is interesting because each of these signals makes use of another plant reaction that is caused by a decrease in stomatal conductance. Such a multi-plant trait approach is less prone to random errors in either of the signals and provides thereby a convergence

of evidence to estimate of canopy conductance (Gs) or of a stress factor $\overline{\alpha}$, in a way similar to the framework proposed in Chapter 3. This could then, in turn, to better estimates of canopy-scale photosynthesis.
A third research axis at the plant scale would be to study the canopy structural reaction and investigate its usefulness for drought stress detection. Chapter 2 of this thesis describes that the canopy structure changes at diurnal timescales during stressed days. A change in leaf turgor is a probable explanation for this change. If the dynamic canopy structure can indeed be linked to the leaf turgor, the canopy structure, based on a structural index like the Fluorescence Correction Vegetation Index (FCVI) and the Near-Infrared Reflectance of Vegetation (NIRv) bear the potential to be a low-cost stress indicator, as relatively cheap broadband cameras are able to retrieve both variables with a low signal-to-noise ratio. Additionally, it would also be interesting to compare the change in the structural indices to short-term variability in vegetation optical depth (VOD), as the latter is also often looked at as an indicator for leaf water potential. A synergetic interpretation of ϕ_F and a remotely sensed proxy of leaf water potential can provide a complete picture of the plant water status. While the ϕ_F provides indeed information on the slowed-down plant growth, it fails to grasp the peril that anisohydric plants put themselves in, when they keep their photosynthetic rates high while drying themselves out. An approach that integrates both these components of a plant drought stress reaction will provide a more complete image of how vegetation health is impacted by drought stress.

5.2.2 SIF monitoring at local to regional scale with geostationary satellites

In all chapters of this thesis, the sensitivity of large-scale SIF to the environmental conditions at the moment of the measurement is pointed out. The vapour pressure deficit (VPD), as well as the downward photosynthetically active radiation (PAR) can show a large variation at diurnal timescales, and the fluorescence emission reacts instantaneously, as pointed out in Chapter 2. Chapter 4 points out that the large-scale SIF reacts to soil moisture and VPD. Consequently, it is expected that ϕ_F from geostationary satellites can provide information on the evolution of drought stress at small timescales, thereby allowing to detect flash droughts and allowing large-scale SIF to serve as an early drought

detection tool. Two geostationary satellites are to be launched soon; NASAś Tropospheric Emissions: Monitoring of POllution (TEMPO; launched on April, 7TH) and Sentinel-4 (scheduled for launch in 2024). Like the TROPOMI sensor, used in chapter 4, both sensors are designed for the retrieval of atmospheric trace gasses, but their high spectral resolution allows for SIF retrievals. The introduction of multiple SIF measurements a day at large scale could allow for monitoring plant stress reactions that occur at a sub-daily temporal scale, such as the afternoon photosynthetic depression, a phenomenon in that stressed plants slow down their photosynthesis in the afternoon. The high temporal resolution can also be useful for the structural component, as changing leaf turgor can modulate leaf orientation during the day.

5.2.3 Introducing ϕ_F in large-scale data assimilation frameworks

The third chapter in this thesis lays out a framework on how to constrain photosynthetic modules in a crop growth model. To do so, a mechanistic description of the photosynthesis is imperative, for the ϕ_P to be connected to ϕ_F. Over the stomatal conductance, stress has an impact on ϕ_P. Second, a description of the canopy structure is needed for the conversion of ϕ_F to SIF. The framework laid out in Chapter 3 is expected to be useful for large-scale SIF-based stress detection, as both the Farquhar description of photosynthesis as well as the SCOPE model can run at large spatial scales. An interesting and innovative aspect of Chapter 3 is that ϕ_F is not directly used to estimate photosynthesis. Instead, the ϕ_F observations are used to parametrize the stress function, i.e., the ϕ_F data are used to calibrate the plant stress response in function of the given environmental variables. With this approach, only a few ϕ_F observations are sufficient to improve the estimations of the photosynthesis over the entire growing season, given that meteorological data are provided during the entire season. This opens a niche for the FLEX data, as their 27-day temporal resolution will only provide a few measurements over the growing season. Inserting a few FLEX ϕ_F observations in a land surface model that uses daily meteorological data as input can improve the model fluxes during drought periods, even for the days in which there are no ϕ_F data included.

5.2.4 Potential of SIF for pest monitoring

The framework laid out in Chapter 3 establishes a mathematical link between the decrease in ϕ_P, a process that happens at the molecular scale, and the SIF, as observed by the spectrometer at the multi-plant scale. Similar to drought stress, biotic stresses have been observed to increase ϕ_N, thereby also affecting ϕ_P and ϕ_F (Pérez-Bueno et al., 2019). Such effects are already measurable in right after the infection. In this sense, SIF has an advantage compared to classical remote sensing indices, that only show a reaction when a plant shows visible pest damage. Similar to Eq. 3.10-3.13, it is possible to describe a link between ϕ_F and a biotic stress. The SCOPE part of chapter 3, which upscales the ϕ_F to the canopy scale is workable for whichever kind of stress, biotic or abiotic. Currently, the AgroC model does not have capabilities to deal with biotic stress, but a stress-induced reduction in photosynthesis in the beginning of an infection is relatively straightforward to implement, making use of a stress factor. Combined biotic-abiotic stresses, as well as severely sick plants, are harder to model. At the molecular scale, the parameters that determine the $K_n - K_p$ relationship (γ, β, and Kn0 in Table 3.3) need to be re-calculated for biotic stresses. It is probable that each specific kind of biotic stress needs its own calibration, as each biotic stress has its own way of interfering with the plant's physiology. A main difference between using SIF data to improve drought stress in a model and using SIF to improve biotic stress in a model is the concept of a stress function. A stress function, that links the stress factor $\overline{\alpha}$ to measurable variables is impossible to define for a biotic stress. Consequently, it is not straightforward to improve the fluxes over the entire growing season by inserting just a few SIF measurements, as done in Chapter 3. Instead, SIF-based pest monitoring infrastructures probably need frequent SIF measurements.

5.3 Towards operational applications in the near and distant future

5.3.1 Optimize irrigation dosing by including SIF data

This thesis shows that drought stress affects the SIF emission both at the plant scale, as well as at the landscape and global scales. At the plant or plot scale, this sensitivity can be exploited to detect water-stressed plants, that would benefit from additional irrigation water.

Pilot projects that explore the use of SIF to design smart irrigation systems have demonstrated the sensitivity of SIF to different irrigation regimes (Zhao et al., 2022), in a way similar to Chapter 2. SIF-based smart irrigation systems can work in two ways; first, frequent SIF measurements can be converted to ϕ_F measurements, allowing spotting a decrease in photosynthetic activity. Alternatively, smart irrigation systems could benefit from SIF measurements as SIF measurements allow us to finetune the threshold value of soil moisture/soil water potential by which irrigation can be helpful, alike h_3 in Chapter 3. The advantage of such a method is that only a few SIF measurements can already calibrate the soil moisture/soil water potential by which water stress kicks in. This method needs fewer SIF measurements, but it does need frequent measurements of soil moisture or soil water potential.

5.3.2 Inclusion of SIF in continental-scale drought monitoring tools

A main advantage of SIF data compared to meteorological data or soil moisture data is its ability to consider a vegetation aspect. Currently, the European Drought Observatory (EDO- European Drought Observatory, 2017) monitors the drought by making use of the Combined Drought Indicator (Sepulcre-Canto et al., 2012). The index does include some vegetation aspect in the form of fPAR data and more implicitly in soil moisture data, as plants with lower canopy conductance transpire less, leaving more water behind in the soil. An inclusion of ϕ_F in such framework would improve the drought monitor in two ways. First, ϕ_F is known to react instantaneously to a stress, compared to reflectance-based vegetation indices. Second, the reaction of ϕ_F is proportional to the drought stress intensity. Both these components provide interesting information for policymakers, as an early warning of a drought allows to take timely pre-emptive measures, such as a regulation on irrigation waters.

5.3.3 Inclusion of SIF in crop yield prediction models

Photosynthesis is the most essential process that drives plant growth. Consequently, the SIF signal has extensively been studied in the context of crop yield modelling (e.g., Guanter et al., 2014; Peng et al., 2020). The techniques used to estimate crop yield based on SIF data break

down in two broad categories: using either a mechanistic approach or a machine learning approach. The mechanistic approach is similar to the approach laid out in Chapter 3; it requires a photosynthetic model to run at a certain spatial scale, and the model can be constrained with the SIF data. As an alternative method, various researchers pointed out that the correlation between SIF and crop yield can be exploited to train machine learning algorithms (Liu et al., 2022; Peng et al., 2020). Compared to the mechanistic approach in Chapter 3, a machine learning approach is more straightforward, as it does not require an elaborate mechanistic description of the photosynthesis, and neither does it need to calibrate various photosynthetic parameters, such as the VCMax. However, current studies describe that a 5-7 year long SIF time series is imperative for an adequate crop yield prediction. Over the corn belt, SIF-based models barely outperformed models that were only trained on NIRv (Peng et al., 2020). Crop yield models are known to improve significantly when they consider the water availability in addition to the canopy greenness (White et al., 2020). Given the sensitivity of ϕ_F to drought conditions, a machine learning technique combining SM, ϕ_F and NDVI is expected to outperform current crop yield prediction models once reliable field-resolution SIF measurements are available. The 300 metre spatial resolution of the FLEX satellite provides sufficient information on the spatiotemporal variability of the vegetation without drowning the system in excessive information (Duveiller and Defourny, 2010). Therefore, FLEX data are a promising upcoming data stream for crop yield monitoring.

5.3.4 Potential for SIF in drought insurance

Drought-induced lowered crop yields reduce the farm's financial income, jeopardizing the financial health of an agricultural enterprise for the years following a drought. Given the increasing frequency of droughts, the European agricultural sector is facing ever-growing demand for reliable insurance against climatic extremes. Here, the insurance industry faces two kind of market failures. The first was an information asymmetry, in which more risk-exposed farmers were more likely to seek insurance compared to less exposed farmers. A second was a moral hazard, an effect in which an insured farmer had less incentive to minimize its crop yield loss when facing a drought. An

emerging technique to resolve these market failures is the use of an index insurance; a system that bases a pay-out on the severity of the drought, rather than on the reduction of the crop yield (Vroege et al., 2019). This technique evokes a key question: how do we quantify the severity of a drought in an objective and agriculturally meaningful way?

The workhorse of vegetation remote sensing, NDVI data have proven their value (Castillo et al., 2016), as they show how much a crop has suffered during a growing season, but SIF has the potential to provide a more mechanistic interpretation of the severity of the stress. Weather-based drought indices, or microwave-based soil moisture provide a low-cost method to estimate the severity of the drought conditions (de Leeuw et al., 2014; Kenduiywo et al., 2021), but every plant tends to react differently to drought stress, making a physiologically meaningful interpretation difficult. Here, SIF can come into play, since they allow to establish a link between stress severity -in a physiological sense, and the meteorological parameters. Such stress severity index can then contribute to an index to base an index insurance on.

5.3.5 Perspectives for the FLuorescence EXplorer (FLEX) mission

The FLuorescence EXplorer (FLEX) is the first satellite whose equipment is tailored to global SIF retrieval. FLEX data will be a game-changer in the SIF community, as they will spectacularly improve the spatial resolution, as well as the signal-to-noise ratio and the spatial resolution, of the radiance measurements, leading to high-quality SIF retrievals at a 300 m spatial resolution with a 27-day temporal resolution. This is a spatial resolution similar to MODIS or Sentinel-3 reflectances or Landsat-based thermal data. FLEX will be sent in tandem with a Sentinel-3 satellite, allowing for a synergetic interpretation of reflectance and fluorescence data. The link between SIF and stress will allow finding stress-sensitive areas within a landscape, which is not yet possible with TROPOMI data. FLEX will take measurements of both PRI, SIFB, and SIFA, as well as a measurement of NIRvP, allowing a multi-variable estimation of the plant stress status. The improved spatial resolution will open the door for new SIF applications, such as refined crop yield monitoring, or monitoring of the ecosystem health of more heterogeneous landscapes.

List of publications

Peer-reviewed

- Jonard, F., **De Cannière, S.**, Brüggemann, N., Gentine, P., Short Gianotti, D.J., Lobet, G., Miralles, D.G., Montzka, C., Pagán, B.R., Rascher, U., Vereecken, H., 2020. Value of sun-induced chlorophyll fluorescence for quantifying hydrological states and fluxes: Current status and challenges. Agricultural and Forest Meteorology 291

- **De Cannière, S.**, Herbst, M., Vereecken, H., Defourny, P., Jonard, F. 2021. Constraining water limitation of photosynthesis in a crop growth model with sun-induced chlorophyll fluorescence, in: Remote Sensing of Environment, volume 267, Page 112722.

- **De Cannière, S.**, Vereecken, H., Defourny, P., Jonard, F., 2022. Remote Sensing of Instantaneous Drought Stress at Canopy Level Using Sun-Induced Chlorophyll Fluorescence and Canopy Reflectance, In Remote Sensing, volume 14, page 2642.

- **De Cannière, S.**, Chaparro, D., Baur, M., Jagdhuber, T., Jonard, F. Environmental controls on spaceborne sun-induced chlorophyll fluorescence yield, in revision in Remote Sensing of Environment.

- Beauclaire, Q., **De Cannière, S.**, Jonard, F., Longdoz, B. Mechanistic modelling of gross primary production and latent heat flux using SIF observations in different water and light limitation conditions (in preparation).

International Conferences

- **De Cannière, S.**, Herbst, M., Rascher, U., Vereecken, H., Defourny, P., Jonard, F., 2019. Field-scale monitoring of drought stress using chlorophyll fluorescence with the coupled SCOPE-AgroC model, in: International Network on Remote Sensing of Terrestrial and Aquatic Fluorescence, Davos, Switzerland.
- **De Cannière, S.**, Herbst, M., Jonard, F., 2020. Improving drought stress parametrization in a crop growth model, in: European Geosciences Union, Vienna, Austria (online).
- **De Cannière, S.**, Jonard, F., 2021. Tracking Water Limitation in Photosynthesis with Sun-Induced Chlorophyll Fluorescence, in: IGARSS, Brussels, Belgium (online)
- **De Cannière, S.**, Jonard, F., 2022, Satellite-based monitoring of ecosystem-level drought using vegetation optical depth and sun-induced chlorophyll fluorescence, in: IGARSS, Kuala Lumpur, Malaysia (online).
- **De Cannière, S.**, Jonard, F., 2022. Monitoring a plant's reaction to drought stress with hyperspectral remote sensing and sun-induced chlorophyll fluorescence, in: European Geosciences Union, Vienna, Austria.

Bibliography

Ač, A., Malenovský, Z., Olejníčková, J., Gallé, A., Rascher, U., Mohammed, G., 2015. Meta-analysis assessing potential of steady-state chlorophyll fluorescence for remote sensing detection of plant water, temperature and nitrogen stress. Remote Sensing of Environment 168, 420–436. doi:10.1016/j.rse.2015.07.022.

Acebron, K., Matsubara, S., Jedmowski, C., Emin, D., Muller, O., Rascher, U., 2021. Diurnal dynamics of nonphotochemical quenching in Arabidopsis npq mutants assessed by solar-induced fluorescence and reflectance measurements in the field. New Phytologist 229, 2104–2119. doi:10.1111/nph.16984.

Allen, R., Pereira, L., Raes, D., Smith, M., 1998. FAO: Irrigation and Drainage Paper No 56. Food and Agriculture Organization of the United Nations (FAO). Rome.

Alonso, L., Gómez-Chova, L., Vila-Francés, J., Amorós-López, J., Guanter, L., Calpe, J., Moreno, J., 2008. Improved fraunhofer line discrimination method for vegetation fluorescence quantification. IEEE Geoscience and Remote Sensing Letters 5, 620–624. doi:10.1109/LGRS.2008.2001180.

Alonso, L., Van Wittenberghe, S., Amorós-López, J., Vila-Francés, J., Gómez-Chova, L., Moreno, J., 2017. Diurnal cycle relationships between passive fluorescence, PRI and NPQ of vegetation in a controlled stress experiment. Remote Sensing 9. doi:10.3390/rs9080770.

Attia, Z., Domec, J.C., Oren, R., Way, D.A., Moshelion, M., 2015. Growth and physiological responses of isohydric and anisohydric poplars to drought. Journal of Experimental Botany 66, 4373–4381. doi:10.1093/jxb/erv195.

Aumann, H.H., Chahine, M.T., Gautier, C., Goldberg, M.D., Kalnay, E., McMillin, L.M., Revercomb, H., Rosenkranz, P.W., Smith, W.L., Staelin, D.H., Strow, L.L., Susskind, J., 2003. AIRS/AMSU/HSB on

the aqua mission: Design, science objectives, data products, and processing systems. IEEE Transactions on Geoscience and Remote Sensing 41, 253–263. doi:10.1109/TGRS.2002.808356.

Balting, D.F., AghaKouchak, A., Lohmann, G., Ionita, M., 2021. Northern Hemisphere drought risk in a warming climate. npj Climate and Atmospheric Science 4, 1–13. doi:10.1038/s41612-021-00218-2.

Barberon, M., Engelbertus, J., Vermeer, M., De Bellis, D., Takano, J., Salt, D.E., Geldner, N., 2016. Adaptation of root funciton by nutrient-induced plasticity of endodermal differentiation. Cell 164, 447–459.

Bassham, A., Benson, A., Calvin, M., 1950. THE PATH IN PHOTOSYNTHESIS VIII: the role of malic acid. Journal of Biological Chemistry .

Bayat, B., Van Der Tol, C., Verhoef, W., 2018. Integrating satellite optical and thermal infrared observations for improving daily ecosystem functioning estimations during a drought episode. Remote Sensing of Environment 209, 375–394. doi:10.1109/IGARSS.2018.8518309.

Bayat, B., van der Tol, C., Yang, P., Verhoef, W., 2019. Extending the SCOPE model to combine optical reflectance and soil moisture observations for remote sensing of ecosystem functioning under water stress conditions. Remote Sensing of Environment 221, 386–301.

Berger, K., Atzberger, C., Danner, M., D'Urso, G., Mauser, W., Vuolo, F., Hank, T., 2018. Evaluation of the PROSAIL model capabilities for future hyperspectral model environments: A review study. Remote Sensing 10.

Berger, K., Machwitz, M., Kycko, M., Kefauver, S., Van Wittenberghe, S., Gerhards, M., Verrelst, J., Atzberger, C., van der Tol, C., Damm, A., Rascher, U., Herrmann, I., Sobejano Paz, V., Fahrner, S., Pieruschka, R., Prikaziuk, E., Buchaillot, L., Halabuk, A., Celesti, M., Koren, G., Gormus, E., Rossini, M., Foerster, M., Siegmann, B., Abdelbaki, A., Tagliabue, G., Hank, T., Darvischzadeh, R., Aasen, H., Garcia, M., Pocas, I., Bandopadhyay, S., Sulis, M., Tomelleri, E., Rozenstein, O., Filchev, L., Stancile, G., Schlerf, M., 2022. Multi-sensor spectral synergies for crop stress detection and monitoring in the optical domain: a review. Remote Sensing of Environment 280.

Blauhut, V., Stoelzle, M., Ahopelto, L., Brunner, M.I., Teutschbein, C., Wendt, D.E., Akstinas, V., Bakke, S.J., Barker, L.J., Bartošová, L., Briede, A., Cammalleri, C., Kalin, K.C., De Stefano, L., Fendeková, M., Finger, D.C., Huysmans, M., Ivanov, M., Jaagus, J., Jakubínský,

J., Krakovska, S., Laaha, G., Lakatos, M., Manevski, K., Neumann Andersen, M., Nikolova, N., Osuch, M., Van Oel, P., Radeva, K., Romanowicz, R.J., Toth, E., Trnka, M., Urošev, M., Urquijo Reguera, J., Sauquet, E., Stevkov, A., Tallaksen, L.M., Trofimova, I., Van Loon, A.F., Van Vliet, M.T., Vidal, J.P., Wanders, N., Werner, M., Willems, P., Zivković, N., 2022. Lessons from the 2018-2019 European droughts: a collective need for unifying drought risk management. Natural Hazards and Earth System Sciences 22, 2201–2217. doi:10.5194/nhess-22-2201-2022.

Bogena, H.R., Borg, E., Brauer, A., Dietrich, P., Hajnsek, I., Merz, B., Pütz, T., Schmid, H.P., Wollschläger, U., Vereecken, H., Zacharias, S., 2016. TERENO: German network of terrestrial environmental observatories. Journal of large-scale research facilities JLSRF 2, 1–8.

Bota, J., Tomas, M., Flexas, J., Medrano, H., Escalona, J., 2016. Differences among grapevine cultivars in their stomatal behavior and water use efficiency under progressive water stress. Agricultural Water Management 164, 91–99.

Briglia, N., Williams, K., Wu, D., Li, Y., Tao, S., Corke, F., Montanaro, G., Petrozza, A., Amato, D., Cellini, F., Doonan, J.H., Yang, W., Nuzzo, V., 2020. Image-Based Assessment of Drought Response in Grapevines. Frontiers in Plant Science 11, 1–12. doi:10.3389/fpls.2020.00595.

Brogi, C., Huisman, J.A., Herbst, M., Weihermüller, L., Klosterhalfen, A., Montzka, C., Reichenau, T.G., Vereecken, H., 2020. Simulation of spatial variability in crop leaf area index and yield using agroecosystem modeling and geophysicsâĂŘbased quantitative soil information. Vadose Zone Journal 19, 1–24.

Bussotti, F., Gerosa, G., Digrado, A., Pollastrini, M., 2020. Selection of chlorophyll fluorescence parameters as indicators of photosynthetic efficiency in large scale plant ecological studies 108.

Butler, W.L., 1978. Energy distribution in the photochemical apparatus of photosynthesis. Annual Review of Plant Physiology 29, 345–378.

Cai, G., Vanderborght, J., Couvreur, V., Mboh, C.M., Vereecken, H., 2018a. Parameterization of Root Water Uptake Models Considering Dynamic Root Distributions and Water Uptake Compensation. Vadose Zone Journal 17, 160125.

Cai, G., Vanderborght, J., Langensiepen, M., Schnepf, A., Hüging, H., Vereecken, H., 2018b. Root growth, water uptake, and sap flow of

winter wheat in response to different soil water conditions. Hydrology and Earth System Sciences 22, 2449–2470.

Camino, C., Gonzalez-Dugo, V., Hernandez, P., Zarco-Tejada, P.J., 2019. Radiative transfer Vcmax estimation from hyperspectral imagery and SIF retreivals to assess photosynthetic performance in rainfed and irrigated plant phenotyping trials. Remote Sensing of Environment 213.

Cammellari, C., Naumann, G., Mentaschi, L., Formetta, G., Gosling, S., Bisselink, B., De Roo, A., Feyen, L., 2020. Global warming and drought impacts in the EU. Technical Report. Joint Research Centre, European Comission. Ispra, Italy. doi:10.2760/597045.

Campbell, P.K., Huemmrich, K.F., Middleton, E.M., Ward, L.A., Julitta, T., Daughtry, C.S., Burkart, A., Russ, A.L., Kustas, W.P., 2019. Diurnal and seasonal variations in chlorophyll fluorescence associated with photosynthesis at leaf and canopy scales. Remote Sensing 11.

Campos, H., Trejo, C., Peña-Valdivia, C.B., García-Nava, R., Conde-Martínez, F.V., Cruz-Ortega, M.D.R., 2014. Photosynthetic acclimation to drought stress in Agave salmiana Otto ex Salm-Dyck seedlings is largely dependent on thermal dissipation and enhanced electron flux to photosystem i. Photosynthesis Research 122, 23–39. doi:10.1007/s11120-014-0008-6.

Cao, J., An, Q., Zhang, X., Xu, S., Si, T., Niyogi, D., 2021. Is satellite Sun-Induced Chlorophyll Fluorescence more indicative than vegetation indices under drought condition? Science of the Total Environment 792. doi:10.1016/j.scitotenv.2021.148396.

Carminati, A., Javaux, M., 2020. Soil Rather Than Xylem Vulnerability Controls Stomatal Response to Drought. Trends in Plant Science 25, 868–880. doi:10.1016/j.tplants.2020.04.003.

Castillo, M.J., Boucher, S., Carter, M., 2016. Index Insurance: Using Public Data to Benefit Small-Scale Agriculture. International Food and Agribusiness Management Review 19, 93–114.

Caturegli, L., Matteoli, S., Gaetani, M., Grossi, N., Magni, S., Minelli, A., Corsini, G., Remorini, D., Volterrani, M., 2020. Effects of water stress on spectral reflectance of bermudagrass. Scientific Reports 10, 1–12. doi:10.1038/s41598-020-72006-6.

Celesti, M., van der Tol, C., Cogliati, S., Panigada, C., Yang, P., Pinto, F., Rascher, U., Miglietta, F., Colombo, R., Rossini, M., 2018. Exploring the physiological information of Sun-induced chlorophyll fluo-

rescence through radiative transfer model inversion. Remote Sensing of Environment 215, 97–108.

Chang, C.Y., Wen, J., Han, J., Kira, O., LeVonne, J., Melkonian, J., Riha, S.J., Skovira, J., Ng, S., Gu, L., Wood, J.D., Näthe, P., Sun, Y., 2021. Unpacking the drivers of diurnal dynamics of sun-induced chlorophyll fluorescence (SIF): Canopy structure, plant physiology, instrument configuration and retrieval methods. Remote Sensing of Environment 265. doi:10.1016/j.rse.2021.112672.

Cochard, H., Venisse, J.S., Barigah, T.S., Brunel, N., Herbette, S., Guilliot, A., Tyree, M.T., Sakr, S., 2007. Putative role of aquaporins in variable hydraulic conductance of leaves in response to light. Plant Physiology 143, 122–133. doi:10.1104/pp.106.090092.

Cocozza, C., De Miguel, M., Pšidová, E., Ditmarová, L., Marino, S., Maiuro, L., Alvino, A., Czajkowski, T., Bolte, A., Tognetti, R., 2016. Variation in ecophysiological traits and drought tolerance of beech (Fagus sylvatica L.) seedlings from different populations. Frontiers in Plant Science 7, 1–14. doi:10.3389/fpls.2016.00886.

Cousins, A.B., Adam, N.R., Wall, G.W., Kimball, B.A., Pinter, P.J., Ottman, M.J., Leavitt, S.W., Webber, A.N., 2002. Photosystem II energy use, non-photochemical quenching and the xanthophyll cycle in Sorghum bicolor grown under drought and free-air CO2enrichment (FACE) conditions. Plant, Cell and Environment 25, 1551–1559. doi:10.1046/j.1365-3040.2002.00935.x.

Damm, A., Elber, J., Erler, A., Gioli, B., Hamdi, K., Hutjes, R., Kosvancova, M., Meroni, M., Miglietta, F., Moersch, A., Moreno, J., Schickling, A., Sonnenschein, R., Udelhoven, T., van der Linden, S., Hostert, P., Rascher, U., 2010. Remote sensing of sun-induced fluorescence to improve modeling of diurnal courses of gross primary production (GPP). Global Change Biology 16, 171–186.

Damm, A., Paul-Limoges, E., Haghighi, E., Simmer, C., Morsdorf, F., Schneider, F.D., van der Tol, C., Migliavacca, M., Rascher, U., 2018. Remote sensing of plant-water relations: An overview and future perspectives. Journal of Plant Physiology 227, 3–19. doi:10.1016/j.jplph.2018.04.012.

Dash, J., Curran, P., 2004. The Meris Terrestrial Chlorophyll Index. International Journal of Remote Sensing , 5403–5413.

De Cannière, S., Herbst, M., Vereecken, H., Defourny, P., Jonard, F., 2021. Constraining water limitation of photosynthesis in a crop

growth model with sun-induced chlorophyll fluorescence. Remote Sensing of Environment 267. doi:10.1016/j.rse.2021.112722.

De Canniere, S., Vereecken, H., Defourny, P., Jonard, F., 2022. Remote Sensing of Instantaneous Drought Stress at Canopy Level Using Sun-Induced Chlorophyll Fluorescence and Canopy Reflectance. Remote Sensing 14.

De Lannoy, G.J., Bechtold, M., Albergel, C., Brocca, L., Calvet, J.C., Carrassi, A., Crow, W.T., de Rosnay, P., Durand, M., Forman, B., Geppert, G., Girotto, M., Hendricks Franssen, H.J., Jonas, T., Kumar, S., Lievens, H., Lu, Y., Massari, C., Pauwels, V.R., Reichle, R.H., Steele-Dunne, S., 2022. Perspective on satellite-based land data assimilation to estimate water cycle components in an era of advanced data availability and model sophistication. Frontiers in Water 4. doi:10.3389/frwa.2022.981745.

Dechant, B., Ryu, Y., Badgley, G., Köhler, P., Rascher, U., Migliavacca, M., Zhang, Y., Tagliabue, G., Guan, K., Rossini, M., Goulas, Y., Zeng, Y., Frankenberg, C., Berry, J.A., 2022. NIRVP: A robust structural proxy for sun-induced chlorophyll fluorescence and photosynthesis across scales. Remote Sensing of Environment 268. doi:10.1016/j.rse.2021.112763.

Dechant, B., Ryu, Y., Badgley, G., Zeng, Y., Berry, J.A., Zhang, Y., Goulas, Y., Li, Z., Zhang, Q., Kang, M., Li, J., Moya, I., 2020. Canopy structure explains the relationship between photosynthesis and sun-induced chlorophyll fluorescence in crops. Remote Sensing of Environment 241. doi:10.1016/j.rse.2020.111733.

Deckmyn, G., Nijs, I., Ceulemans, R., 2000. A simple method to determine leaf angles of grass species. Journal of Experimental Botany 51, 1467–1470. doi:10.1093/jxb/51.349.1467.

Demmig-Adams, B., Cohu, C.M., Muller, O., Adams, W.W., 2012. Modulation of photosynthetic energy conversion efficiency in nature: From seconds to seasons. Photosynthesis Research 113, 75–88. doi:10.1007/s11120-012-9761-6.

Didan, K., 2015. MOD13C1 MODIS/Terra Vegetation Indices 16-Day L3 Global 0.05Deg CMG V006No Title. doi:https://doi.org/10.5067/MODIS/MOD13C1.006.

Drusch, M., Moreno, J., Bello, U.D., Franco, R., Goulas, Y., Huth, A., Kraft, S., Middleton, E.M., Miglietta, F., Mohammed, G., Nedbal, L.,

Rascher, U., Schüttemeyer, D., Verhoef, W., 2017. Concept âĂŤ ESA ' s Earth Explorer 8. IEEE Trans. Geosci. Remote Sens. 55, 1273–1284.
Ducheyne, S., 2008. A preliminary study of the appropriation of Van Helmont's oeuvre in Britain in chymistry, medicine and natural philosophy. Ambix 55, 122–135. doi:10.1179/174582308X255479.
Duveiller, G., Defourny, P., 2010. A conceptual framework to define the spatial resolution requirements for agricultural monitoring using remote sensing. Remote Sensing of Environment 114, 2637–2650. doi:https://doi.org/10.1016/j.rse.2010.06.001.
EDO- European Drought Observatory, 2017. Trend Viewer - European Drought Observatory - JRC European Commission.
Egea, G., González-Real, M.M., Baille, A., Nortes, P.A., Diaz-Espejo, A., 2011. Disentangling the contributions of ontogeny and water stress to photosynthetic limitations in almond trees. Plant, Cell and Environment 34, 962–979. doi:10.1111/j.1365-3040.2011.02297.x.
Elleder, L., Kasparek, L., Sirova, J., Kabelka, T., 2020. Low water stage marks on hunger stones: Verification for the Elbe from 1616 to 2015. Climate of the Past 16, 1821–1846. doi:10.5194/cp-16-1821-2020.
Entekhabi, B.D., Njoku, E.G., Neill, P.E.O., Kellogg, K.H., Crow, W.T., Edelstein, W.N., Entin, J.K., Goodman, S.D., Jackson, T.J., Johnson, J., Kimball, J., Piepmeier, J.R., Koster, R.D., Martin, N., Mcdonald, K.C., Moghaddam, M., Moran, S., Reichle, R., Shi, J.C., Spencer, M.W., Thurman, S.W., Tsang, L., Zyl, J.V., 2010. The SoilMoistureActive Passive (SMAP) Mission 98.
Eriksen, R.L., Adhikari, N.D., Mou, B., 2020. Comparative photosynthesis physiology of cultivated and wild lettuce under control and low-water stress. Crop Science 60, 2511–2526. doi:10.1002/csc2.20184.
European Space Agency (ESA), 2015. Report for mission selection: An Earth Explorer to observe vegetation in fluorescence. Technical Report.
Farquhar, G., von Caemmerer, S., Berry, J., 1980. A biochemical-model of photosynthetic CO2 assimilation in leaves of C3 species. Planta 149, 78–90.
Feddes, R., Bresler, E., Neuman, S., 1974. Field test of a modified numerical model for water uptake by root systems. Water Resources Research 10, 1199–1206.
Feldman, A.F., Short Gianotti, D.J., Trigo, I.F., Salvucci, G.D., Entekhabi, D., 2020. Land-Atmosphere Drivers of Landscape-Scale

Plant Water Content Loss. Geophysical Research Letters 47. doi:10.1029/2020GL090331.

Feng, B., Liu, P., Li, G., Dong, S.T., Wang, F.H., Kong, L.A., Zhang, J.W., 2014. Effect of Heat Stress on the Photosynthetic Characteristics in Flag Leaves at the Grain-Filling Stage of Different Heat-Resistant Winter Wheat Varieties. Journal of Agronomy and Crop Science 200, 143–155. doi:10.1111/jac.12045.

Féret, J.B., Gitelson, A., Noble, S., Jacquemoud, S., 2017. Prospect-d: Towards modeling leaf optical properties through a complete lifecycle. Remote Sensing of Environment 193, 204–215.

Flexas, J., Díaz-Espejo, A., Conesa, M.A., Coopman, R.E., Douthe, C., Gago, J., Gallé, A., Galmés, J., Medrano, H., Ribas-Carbo, M., Tomàs, M., Niinemets, U., 2016. Mesophyll conductance to CO2 and Rubisco as targets for improving intrinsic water use efficiency in C3 plants. Plant Cell and Environment 39, 965–982. doi:10.1111/pce.12622.

Flexas, J., Escalona, J.M., Evain, S., Gulías, J., Moya, I., Osmond, C.B., Medrano, H., 2002. Steady-state chlorophyll fluorescence (Fs) measurements as a tool to follow variations of net CO2 assimilation and stomatal conductance during water-stress in C3 plants. Physiologia Plantarum , 26–29.

Flexas, J., Ribas-Carbó, M., Bota, J., Galmés, J., Henkle, M., Martínez-Cañellas, S., Medrano, H., 2006. Decreased Rubisco activity during water stress is not induced by decreased relative water content but related to conditions of low stomatal conductance and chloroplast CO2 concentration. New Phytologist 172, 73–82. doi:10.1111/j.1469-8137.2006.01794.x.

Friedl, M.A., Sulla-Menashe, D., Tan, B., Schneider, A., Ramankutty, N., Sibley, A., Huang, X., 2010. MODIS Collection 5 global land cover: Algorithm refinements and characterization of new datasets. Remote Sensing of Environment 114, 168–182. doi:10.1016/j.rse.2009.08.016.

Fu, Z., Ciais, P., Prentice, I.C., Bastos, A., Luo, X., Green, J.K., Gentine, P., Makowski, D., Stoy, P.C., Yang, H., Hajima, T., 2022. Along a Large Range of Soil Water De Fi Cits. Nature Communiacations 13, 989–999.

Fujimura, S., Shi, P., Iwama, K., Zhang, X., Gopal, J., Jitsuyama, Y., 2010. Effect of altitude on the response of net photosynthetic rate to carbon dioxide increase by spring wheat. Plant Production Science 13, 141–149. doi:10.1626/pps.13.141.

Gajanayake, B., Reddy, K.R., 2016. Sweetpotato responses to mid- and late-season soil moisture deficits. Crop Science 56, 1865–1877. doi:10.2135/cropsci2015.03.0154.

Galmés, J., Medrano, H., Flexas, J., 2007. Photosynthetic limitations in response to water stress and recovery in Mediterranean plants with different growth forms. New Phytologist 175, 81–93. doi:10.1111/j.1469-8137.2007.02087.x.

Gamon, J., Penuelas, J., Field, C., 1992. A narrow-waveband spectral index that tracks diurnal changes in photosynthetic efficiency. Remote Sensing of Environment 41, 35–44.

Gao, B.C., 1996. NDWI A Normalized Difference Water Index for Remote Sensing of Vegetation Liquid Water From Space. Remote Sensing of Environment 58, 257–268. doi:10.3109/9781420073553-3.

Garbulsky, M.F., Penuelas, J., Gamon, J., Inoue, Y., Filella, I., 2011. The photochemical reflectance index (PRI) and remote sensing of leaf, canopy and ecosystem radiation use efficiencies A review and meta-analysis. Remote Sensing of Environment 135, 281–297.

Gentine, P., Alemohammad, S.H., 2018. Reconstructed Solar-Induced Fluorescence: A Machine Learning Vegetation Product Based on MODIS Surface Reflectance to Reproduce GOME-2 Solar-Induced Fluorescence. Geophysical Research Letters 45, 3136–3146. doi:10.1002/2017GL076294.

Genty, B., Briantais, J.M., Baker, N.R., 1989. Electron Transport and Quenching of Chlorophyll Fluorescence. Biochimica et Biophysica Acta 990, 87–92.

Gest, H., 2002. History of the word photosynthesis and evolution of its definition. Photosynthesis Research 73, 7–10. doi:10.1023/A:1020419417954.

Ghazaryan, G., König, S., Rezaei, E.E., Siebert, S., Dubovyk, O., 2020. Analysis of drought impact on croplands from global to regional scale: A remote sensing approach. Remote Sensing 12, 1–17.

Gong, F., Chen, X., Yuan, W., Su, Y., Yang, X., Liu, L., Sun, Q., Wu, J., Dai, Y., Shang, J., 2022. Partitioning of three phenology rhythms in American tropical and subtropical forests using remotely sensed solar-induced chlorophyll fluorescence and field litterfall observations. International Journal of Applied Earth Observation and Geoinformation 107, 102698. doi:10.1016/j.jag.2022.102698.

Govindjee, 1995. Sixty-Three Years Since Kautsky: Chlorophyll a Fluorescence. Functional Plant Biology 22, 131. doi:10.1071/pp9950131.

Grantz, D.A., Linscheid, B.S., Grulke, N.E., 2019. Differential responses of stomatal kinetics and steadyâĂŘstate conductance to abscisic acid in a fern: comparison with a gymnosperm and an angiosperm. New Phytologist 222, 1883–1892. doi:10.1111/nph.15736.

Grassi, G., Magnani, F., 2005. Stomatal, mesophyll conductance and biochemical limitations to photosynthesis as affected by drought and leaf ontogeny in ash and oak trees. Plant, Cell and Environment 28, 834–849. doi:10.1111/j.1365-3040.2005.01333.x.

Gu, H., Yin, G., Yang, Y., Verger, A., Filella, I., Zeng, Y., Hao, D., Xie, Q., Li, X., Xiao, J., 2023. Satellite-detected Contrasting Responses of Canopy Structure and Leaf Physiology to Drought. Journal of Selected Topics in Applied Earth Observation and Remote Sensing , 1–10doi:10.1109/JSTARS.2023.3247422.

Guanter, L., Bacour, C., Schneider, A., Aben, I., Van Kempen, T.A., Maignan, F., Retscher, C., Köhler, P., Frankenberg, C., Joiner, J., Zhang, Y., 2021. The TROPOSIF global sun-induced fluorescence dataset from the Sentinel-5P TROPOMI mission. Earth System Science Data 13, 5423–5440. doi:10.5194/essd-13-5423-2021.

Guanter, L., Zhang, Y., Jung, M., Joiner, J., Voigt, M., Berry, J.A., Frankenberg, C., Huete, A.R., Zarco-Tejada, P., Lee, J.E., Moran, M.S., Ponce-Campos, G., Beer, C., Camps-Valls, G., Buchmann, N., Gianelle, D., Klumpp, K., Cescatti, A., Baker, J.M., Griffis, T.J., 2014. Global and time-resolved monitoring of crop photosynthesis with chlorophyll fluorescence. Proceedings of the National Academy of Sciences of the United States of America 111. doi:10.1073/pnas.1320008111.

Gupana, R.S., Odermatt, D., Cesana, I., Giardino, C., Nedbal, L., Damm, A., 2021. Remote sensing of sun-induced chlorophyll-a fluorescence in inland and coastal waters: Current state and future prospects. Remote Sensing of Environment 262, 112482. doi:10.1016/j.rse.2021.112482.

Gupta, A., Rico-Medina, A., Caño-Delgado, A.I., 2020. The physiology of plant responses to drought. Science 368, 266–269. doi:10.1126/science.aaz7614.

Haboudane, D., Miller, J.R., Pattey, E., Zarco-Tejada, P.J., Strachan, I.B., 2004. Hyperspectral vegetation indices and novel algorithms for pre-

dicting green LAI of crop canopies: Modeling and validation in the context of precision agriculture. Remote Sensing of Environment 90, 337–352. doi:10.1016/j.rse.2003.12.013.

He, L., Wood, J.D., Sun, Y., Magney, T., Dutta, D., Köhler, P., Zhang, Y., Yin, Y., Frankenberg, C., 2020. Tracking Seasonal and Interannual Variability in Photosynthetic Downregulation in Response to Water Stress at a Temperate Deciduous Forest. Journal of Geophysical Research: Biogeosciences 125, 1–23. doi:10.1029/2018JG005002.

Heino, M., Puma, M.J., Ward, P.J., Gerten, D., Heck, V., Siebert, S., Kummu, M., 2018. Two-thirds of global cropland area impacted by climate oscillations. Nature Communications 9, 1–10.

Helm, L., Shi, H., Lerdau, M., Yang, X., 2020. Solar-induced chlorophyll fl uorescence and short-term photosynthetic response to drought. Ecological applications 30, 1–12.

Hengl, T., Gupta, S., 2019. Soil water content (volumetric %) for 33 kpa and 1500kpa suctions predicted at 6 standard depths (0,10,30,100 and 200 cm) at 250 m resolution (version v01) [dataset].

Herbst, M., Hellebrand, H.J., Bauer, J., Huisman, J.A., ŠimÅŕnek, J., Weihermüller, L., Graf, A., Vanderborght, J., Vereecken, H., 2008. Multiyear heterotrophic soil respiration: Evaluation of a coupled CO2 transport and carbon turnover model. Ecological Modelling 214, 271–283.

Herbst, M., Pohlig, P., Graf, A., WeihermÃijller, L., Schmidt, M., Vanderborght, J., Vereecken, H., 2021. Quantification of water stress induced within-field variability of carbon dioxide fluxes in a sugar beet stand. Agricultural and Forest Meteorology 297, 108242.

Herrmann, H.A., Schwartz, J.M., Johnson, G.N., 2019. From empirical to theoretical models of light response curves - linking photosynthetic and metabolic acclimation. Photosynthesis Research 145, 5–14. doi:10.1007/s11120-019-00681-2.

Hervás-Gámez, C., Delgado-Ramos, F., 2019. Drought management planning policy: From Europe to Spain. Sustainability (Switzerland) 11, 1–26. doi:10.3390/su11071862.

Huang, J., Gómez-Dans, J.L., Huang, H., Ma, H., Wu, Q., Lewis, P.E., Liang, S., Chen, Z., Xue, J.H., Wu, Y., Zhao, F., Wang, J., Xie, X., 2019. Assimilation of remote sensing into crop growth models: Current status and perspectives. Agricultural and Forest Meteorology 276-277, 107609. doi:10.1016/j.agrformet.2019.06.008.

Hupet, F., Lambot, S., Feddes, R.A., Van Dam, J.C., Vanclooster, M., 2003. Estimation of root water uptake parameters by inverse modeling with soil water content data. Water Resources Research 39.

Ihuoma, S.O., Madramootoo, C.A., 2019. Sensitivity of spectral vegetation indices for monitoring water stress in tomato plants. Computers and Electronics in Agriculture 163, 104860. doi:10.1016/j.compag.2019.104860.

Jahns, P., Holzwarth, A., 2012. The role of the xanthophyll cycle and lutein in photoprotection of photosystem II. Biochimica et Biophysica Acta 1817, 182–193.

Jarvis, P.G., 1976. The Interpretation of the Variations in Leaf Water Potential and Stomatal Conductance Found in Canopies in the Field Author (s): P . G . Jarvis Source : Philosophical Transactions of the Royal Society of London . Series B , Biological Sciences , Publish. Philosophical Transactions of the Royal Society of London 273, 593–610.

Javaux, M., Carminati, A., 2021. Soil hydraulics affect the degree of isohydricity. Plant Physiology 186, 1378–1381. doi:10.1093/PLPHYS/KIAB154.

Jenkinson, D., Coleman, K., 2008. The turnover of organic carbon in subsoils. Part 2. Modelling carbon turnover. European journal of soil science 59, 400–413.

Jin, E.S., Yokthongwattana, K., Polle, J.E., Melis, A., 2003. Role of the reversible xanthophyll cycle in the photosystem II damage and repair cycle in Dunaliella salina. Plant Physiology 132, 352–364. doi:10.1104/pp.102.019620.

Joiner, J., Yoshida, Y., Koehler, P., Frankenberg, C., Parazoo, N.C., 2022. L2 Daily Solar-Induced Fluorescence (SIF) from MetOp-A GOME-2, 2007-2018. doi:10.3334/ORNLDAAC/2083.

Jonard, F., André, F., Ponette, Q., Vincke, C., Jonard, M., 2011. Sap flux density and stomatal conductance of European beech and common oak trees in pure and mixed stands during the summer drought of 2003. Journal of Hydrology 409, 371–381. doi:10.1016/j.jhydrol.2011.08.032.

Jonard, F., De Cannière, S., Brüggemann, N., Gentine, P., Short Gianotti, D.J., Lobet, G., Miralles, D.G., Montzka, C., Pagán, B.R., Rascher, U., Vereecken, H., 2020. Value of sun-induced chlorophyll fluorescence

for quantifying hydrological states and fluxes: Current status and challenges. Agricultural and Forest Meteorology 291.

Jonard, F., Feldman, A.F., Short Gianotti, D.J., Entekhabi, D., 2022. Observed water and light limitation across global ecosystems. Biogeosciences 19, 5575–5590. doi:10.5194/bg-19-5575-2022.

Jopia, A., Zambrano, F., Pérez-Martínez, W., Vidal-Páez, P., Molina, J., Mardones, F.d.l.H., 2020. Time-series of vegetation indices (VNIR/SWIR) derived from sentinel-2 (A/B) to assess turgor pressure in Kiwifruit. ISPRS International Journal of Geo-Information 9, 1–18.

Julitta, T., Corp, L.A., Rossini, M., Burkart, A., Cogliati, S., Davies, N., Hom, M., Arthur, A.M., Middleton, E.M., Rascher, U., Schickling, A., Colombo, R., 2016. Comparison of sun-induced chlorophyll fluorescence estimates obtained from four portable field spectroradiometers. Remote Sensing 8, 1–14. doi:10.3390/rs8020122.

Junttila, S., Hölttä, T., Puttonen, E., Katoh, M., Vastaranta, M., Kaartinen, H., Holopainen, M., Hyyppä, H., 2021. Terrestrial laser scanning intensity captures diurnal variation in leaf water potential. Remote Sensing of Environment 255. doi:10.1016/j.rse.2020.112274.

Kautsky, H., Hirsch, A., 1931. Neue Versuche zur Kohlensäureassimilation. Die Naturwissenschaften 19, 964. doi:10.1007/BF01516164.

Kebbas, S., Lutts, S., Aid, F., 2015. Effect of drought stress on the photosynthesis of Acacia tortilis subsp. raddiana at the young seedling stage. Photosynthetica 53, 288–298. doi:10.1007/s11099-015-0113-6.

Kenduiywo, B., Carter, M., Ghosh, A., Hijmans, R.J., 2021. Evaluating the quality of remote sensing products for agricultural index insurance. PLoS ONE October, 1–24. doi:10.1371/journal.pone.0258215.

Kimm, H., Guan, K., Burroughs, C.H., Peng, B., Ainsworth, E.A., Bernacchi, C.J., Moore, C.E., Kumagai, E., Yang, X., Berry, J.A., Wu, G., 2021a. Quantifying high-temperature stress on soybean canopy photosynthesis: The unique role of sun-induced chlorophyll fluorescence. Global Change Biology 27, 2403–2415. doi:10.1111/gcb.15603.

Kimm, H., Guan, K., Jiang, C., Miao, G., Wu, G., Suyker, A.E., Ainsworth, E.A., Bernacchi, C.J., Montes, C.M., Berry, J.A., Yang, X., Frankenberg, C., Chen, M., KÃ¶hler, P., 2021b. A physiological signal derived from sun-induced chlorophyll fluorescence quantifies crop physiological response to environmental stresses

in the U.S. Corn Belt. Environmental Research Letters 16. doi:10.1088/1748-9326/ac3b16.

Klosterhalfen, A., Herbst, M., Weihermüller, L., Graf, A., Schmidt, M., Stadler, A., Schneider, K., Subke, J.A., Huisman, J.A., Vereecken, H., 2017. Multi-site calibration and validation of a net ecosystem carbon exchange model for croplands. Ecological Modelling 363, 137–156.

Kohzuma, K., Tamaki, M., Hikosaka, K., 2021. Corrected photochemical reflectance index (PRI) is an effective tool for detecting environmental stresses in agricultural crops under light conditions. Journal of Plant Research 134, 683–694. doi:10.1007/s10265-021-01316-1.

Konings, A.G., Gentine, P., 2017. Global variations in ecosystem-scale isohydricity. Global Change Biology 23, 891–905. doi:10.1111/gcb.13389.

Konings, A.G., Piles, M., Das, N.N., Entekhabi, D., 2017. L-band vegetation optical depth and effective scattering albedo estimation from SMAP. Remote Sensing of Environment 198, 460–470.

Kovác, D., Alexander, A., Ladislav, Š., Peñuelas, J., Grace, J., Urban, O., 2022. Science of the Total Environment Combining NDVI , PRI and the quantum yield of solar-induced fluorescence improves estimations of carbon fluxes in deciduous and evergreen forests. Science of the Total Environment 829.

Kruger, T., Illioaia, C., Johnson, M., Ruban, A., Papagiannakis, E., Horton, P., van Grondelle, R., 2012. Controlled distorder in plant light-harvesting complex II explains its photoprotective role. Biophysical Journal , 2669–2676.

Kuhnert, M., Yeluripati, J., Smith, P., Hoffmann, H., van Oijen, M., Constantin, J., Coucheney, E., Dechow, R., Eckersten, H., Gaiser, T., Grosz, B., Haas, E., Kersebaum, K.C., Kiese, R., Klatt, S., Lewan, E., Nendel, C., Raynal, H., Sosa, C., Specka, X., Teixeira, E., Wang, E., Weihermüller, L., Zhao, G., Zhao, Z., Ogle, S., Ewert, F., 2017. Impact analysis of climate data aggregation at different spatial scales on simulated net primary productivity for croplands. European Journal of Agronomy 88, 41–52.

Kumar, M., 2016. Impact of climate change on crop yield and role of model for achieving food security. Environmental Monitoring and Assessment 188.

Lang, Y., Wang, M., Xia, J., Zhao, Q., 2018. Effects of soil drought stress on photosynthetic gas exchange traits and chlorophyll fluores-

cence in Forsythia suspensa. Journal of Forestry Research 29, 45–53. doi:10.1007/s11676-017-0420-9.

Lee, J.E., Berry, J.A., van der Tol, C., Yang, X., Guanter, L., Damm, A., Baker, I., Frankenberg, C., 2015. Simulations of chlorophyll fluorescence incorporated into the Community Land Model version 4. Global Change Biology 21, 3469–3477.

Lee, J.E., Frankenberg, C., van der Tol, C., Berry, J.A., Guanter, L., Boyce, C.K., Fisher, J.B., Morrow, E., Worden, J.R., Asefi, S., Badgley, G., Saatchi, S., 2013. Forest productivity and water stress in Amazonia: Observations from GOSAT chlorophyll fluorescence. Proceedings of the royal society B: biological sciences 230.

de Leeuw, J., Vrieling, A., Shee, A., Atzberger, C., Hadgu, K., Biradar, C., Keah, H., Turvey, C., 2014. The Potential and Uptake of Remote Sensing in Insurance: A Review. Remote Sensing 6, 10888–10912. doi:10.3390/rs61110888.

Lemordant, L., Gentine, P., Stéfanon, M., Drobinski, P., Fatichi, S., 2016. Modification of land-atmosphere interactions by CO2 effects: Implications for summer dryness and heat wave amplitude. Geophysical Research Letters 43, 10,240–10,248. doi:10.1002/2016GL069896.

Li, A., Yao, C., Xia, J., Wang, H., Cheng, Q., Penty, R., Fainman, Y., Pan, S., 2022. Advances in cost-effective integrated spectrometers. Light: Science and Applications 11, 1–18. doi:10.1038/s41377-022-00853-1.

Li, S., Pezeshki, S.R., Goodwin, S., 2004. Effects of soil moisture regimes on photosynthesis and growth in cattail (Typha latifolia). Acta Oecologica 25, 17–22. doi:10.1016/j.actao.2003.10.004.

Lin, K.H., Hwang, W.C., Lo, H.F., 2007. Chilling stress and chilling tolerance of sweet potato as sensed by chlorophyll fluorescence. Photosynthetica 45, 628–632. doi:10.1007/s11099-007-0108-z.

Liu, L., Gudmundsson, L., Hauser, M., Qin, D., Shuangcheng, L., Seneviratne, S., 2020. Soil moisture dominates dryness stress on ecosystem production globally. Nature Communications 11. doi:10.1038/s41467-020-18631-1.

Liu, Z., Zhao, F., Liu, X., Yu, Q., Wang, Y., Peng, X., Cai, H., Lu, X., 2022. Direct estimation of photosynthetic CO2 assimilation from solar-induced chlorophyll fluorescence (SIF). Remote Sensing of Environment 271, 112893. doi:10.1016/j.rse.2022.112893.

Long, S.P., Bernacchi, C.J., 2003. Gas exchange measurements, what can they tell us about the underlying limitations to photosynthesis?

Procedures and sources of error. Journal of Experimental Botany 54, 2393–2401. doi:10.1093/jxb/erg262.

Lu, H., Qin, Z., Lin, S., Chen, X., Chen, B., He, B., Wei, J., Yuan, W., 2022. Large influence of atmospheric vapor pressure deficit on ecosystem production efficiency. Nature Communications 13, 10–13. doi:10.1038/s41467-022-29009-w.

Ma, L., Sun, L., Wang, S., Chen, J., Chen, B., Zhu, K., Amir, M., Wang, X., Liu, Y., Wang, P., Wang, J., Huang, M., Wang, Z., 2022. Analysis on the relationship between sun-induced chlorophyll fluorescence and gross primary productivity of winter wheat in northern China. Ecological Indicators 139. doi:10.1016/j.ecolind.2022.108905.

MacBean, N., Maignan, F., Bacour, C., Lewis, P., Peylin, P., Guanter, L., Köhler, P., Gómez-Dans, J., Disney, M., 2018. Strong constraint on modelled global carbon uptake using solar-induced chlorophyll fluorescence data. Scientific Reports 8, 1–12. doi:10.1038/s41598-018-20024-w.

Maes, W., Steppe, K., 2012. Estimating evapotranspiration with ground-based thermal remote sensing in agriculture: a review. Journal of Experimental Botany 63, 695–709. doi:10.1093/jxb/err313.

Maes, W.H., Pagán, B.R., Martens, B., Gentine, P., Guanter, L., Steppe, K., Verhoest, N.E., Dorigo, W., Li, X., Xiao, J., Miralles, D.G., 2020. Sun induced fluorescence closely linked to ecosystem transpiration as evidenced by satellite data and radiative transfer models. Remote Sensing of Environment 249. doi:10.1016/j.rse.2020.112030.

Magney, T.S., Frankenberg, C., Fisher, J.B., Sun, Y., North, G.B., Davis, T.S., Kornfeld, A., Siebke, K., 2017. Methods Connecting active to passive fluorescence with photosynthesis : a method for evaluating remote sensing measurements of Chl fluorescence doi:10.1111/nph.14662.

Maier, S., 2002. Remote Sensing and Modelling of Solar Induced Fluorescence, in: Proceedings of the FLEX workshop, ESA SP-527; 19-20 June, p. 6.

Man, J., Yu, Z., Shi, Y., 2017. Radiation Interception, Chlorophyll Fluorescence and Senescence of Flag leaves in Winter Wheat under Supplemental Irrigation. Scientific Reports 7, 1–13. doi:10.1038/s41598-017-07414-2.

Martínez-Ballesta, M.C., Aparicio, F., Pallás, V., Martínez, V., Carvajal, M., 2003. Influence of saline stress on root hydraulic conductance

and PIP expression in Arabidopsis. Journal of Plant Physiology 160, 689–697. doi:10.1078/0176-1617-00861.

Mauder, M., Cuntz, M., DrÃije, C., Graf, A., Rebmann, C., Schmid, H.P., Schmidt, M., Steinbrecher, R., 2013. A strategy for quality and uncertainty assessment of long-term eddy-covariance measurements. Agricultural and Forest Meteorology 169, 122 – 135.

McFarlane, J.C., Watson, R.D., Theisen, A.F., Jackson, R.D., Ehrler, W.L., Pinter, P.J., Idso, S.B., Reginato, R.J., 1980. Plant stress detection by remote measurement of fluorescence. Appl. Opt. 19, 3287–3289. doi:10.1364/AO.19.003287.

Medlyn, B., Duursma, R., Eamus, D., Ellsworth, D., Prentice, C., Bartons, C., Crous, K., De Angelis, P., Freeman, M., Wingate, L., 2011. Reconciling the optimal and empirical approaches to modelling stomatal conductance. Global Change Biology 2, 2134–2144. doi:10.1111/j.1365-2486.2010.02375.x.

Meyer, T., Jagdhuber, T., Piles, M., Fink, A., Grant, J., Vereecken, H., Jonard, F., 2019. Estimating gravimetric water content of awinter wheat field from L-band vegetation optical depth. Remote Sensing 11. doi:10.3390/rs11202353.

Miyake, C., Shinzaki, Y., Miyata, M., Tomizawa, K.I., 2004. Enhancement of cyclic electron flow around PSI at high light and its contribution to the induction of non-photochemical quenching of Chl fluorescence in intact leaves of tobacco plants. Plant and Cell Physiology 45, 1426–1433. doi:10.1093/pcp/pch163.

Mohammed, G.H., Colombo, R., Middleton, E.M., Rascher, U., van der Tol, C., Nedbal, L., Goulas, Y., Pérez-Priego, O., Damm, A., Meroni, M., Joiner, J., Cogliati, S., Verhoef, W., Malenovský, Z., Gastellu-Etchegorry, J.P., Miller, J.R., Guanter, L., Moreno, J., Moya, I., Berry, J.A., Frankenberg, C., Zarco-Tejada, P.J., 2019. Remote sensing of solar —induced chlorophyll fluorescence (SIF) in vegetation: 50âĂŕyears of progress. Remote Sensing of Environment 231, 111177. doi:10.1016/j.rse.2019.04.030.

Murchie, E.H., Lawson, T., 2013. Chlorophyll fluorescence analysis: A guide to good practice and understanding some new applications. Journal of Experimental Botany 64, 3983–3998. doi:10.1093/jxb/ert208.

Myneri, R., Knayazikhin, Y., Park, T., 2015. Mcd15a2h

modis/terra+aqua leaf area index/fpar 8-day l4 global 500m sin grid v006. doi:10.5067/MODIS/MCD15A2H.006.

Nash, J., Sutcliffe, J., 1970. River flow forecasting through conceptual models part i âĂŤ a discussion of principles. Journal of Hydrology 10, 282–290.

Nguyen, T.T., Arndt, S.K., Baker, P.J., 2019. Leaf physiological responses to drought stress and community assembly in an Asian Savanna. Forests 10, 15–17. doi:10.3390/f10121119.

Niyogi, K.K., Truong, T.B., 2013. Evolution of flexible non-photochemical quenching mechanisms that regulate light harvesting in oxygenic photosynthesis. Current Opinion in Plant Biology 16, 307–314. doi:10.1016/j.pbi.2013.03.011.

Norton, A.J., Rayner, P.J., Koffi, E.N., Scholze, M., 2018. Assimilating solar-induced chlorophyll fluorescence into the terrestrial biosphere model BETHY-SCOPE v1.0: Model description and information content. Geoscientific Model Development 11, 1517–1536.

Novick, K.A., Konings, A.G., Gentine, P., 2019. Beyond soil water potential: An expanded view on isohydricity including landâĂŞatmosphere interactions and phenology. Plant Cell and Environment 42, 1802–1815. doi:10.1111/pce.13517.

O, S., Hou, X., Orth, R., 2020. Observational evidence of wildfire-promoting soil moisture anomalies. Scientific Reports 10, 11008. doi:10.1038/s41598-020-67530-4.

Orimoloye, I.R., 2022. Agricultural Drought and Its Potential Impacts: Enabling Decision-Support for Food Security in Vulnerable Regions. Frontiers in Sustainable Food Systems 6. doi:10.3389/fsufs.2022.838824.

Pacheco-Labrador, J., Perez-Priego, O., El-Madany, T.S., Julitta, T., Rossini, M., Guan, J., Moreno, G., Carvalhais, N., Martín, M.P., Gonzalez-Cascon, R., Kolle, O., Reischtein, M., van der Tol, C., Carrara, A., Martini, D., Hammer, T.W., Moossen, H., Migliavacca, M., 2019. Multiple-constraint inversion of SCOPE. Evaluating the potential of GPP and SIF for the retrieval of plant functional traits. Remote Sensing of Environment 234, 111362.

Palmer, W.C., 1965. Monitoring Drought. Technical Report.

Pantin, F., Monnet, F., Jannaud, D., Costa, J.M., Renaud, J., Muller, B., Simonneau, T., Genty, B., 2013. The dual effect of abscisic acid on stomata. New Phytologist 197, 65–72. doi:10.1111/nph.12013.

Parazoo, N.C., Bowman, K., Fisher, J.B., Frankenberg, C., Jones, D.B., Cescatti, A., Pérez-Priego, Ó., Wohlfahrt, G., Montagnani, L., 2014. Terrestrial gross primary production inferred from satellite fluorescence and vegetation models. Global Change Biology 20, 3103–3121.

Parkash, V., Singh, S., 2020. A review on potential plant-basedwater stress indicators for vegetable crops. Sustainability (Switzerland) 12.

Peng, B., Tang, J., Berkeley, L., Bernacchi, C., Cooper, M., 2020. Towards a multiscale crop modelling framework for climate change adaptation assessment. Nature plants doi:10.1038/s41477-020-0625-3.

Pérez-Bueno, M.L., Pineda, M., Barón, M., 2019. Phenotyping Plant Responses to Biotic Stress by Chlorophyll Fluorescence Imaging. Frontiers in Plant Science 10, 1–15. doi:10.3389/fpls.2019.01135.

Petruzzellis, F., Savi, T., Bacaro, G., Nardini, A., 2019. A simplified framework for fast and reliable measurement of leaf turgor loss point. Plant Physiology and Biochemistry 139, 395–399. doi:10.1016/j.plaphy.2019.03.043.

Pettigrew, W.T., 2004. Physiological consequences of moisture deficit stress in cotton. Crop Science 44, 1265–1272. doi:10.2135/cropsci2004.1265.

Pinto, F., Damm, A., Schickling, A., Panigada, C., Cogliati, S., Müller-linow, M., Ballvora, A., 2016. Sun-induced chlorophyll fluorescence from high-resolution imaging spectroscopy data to quantify spatio-temporal patterns of photosynthetic function in crop canopies. Plant Cell and Environment 39, 1500–1512. doi:10.1111/pce.12710.

Plascyk, J.A., Gabriel, F.C., 1975. The Fraunhofer Line Discriminator MKII-An Airborne Instrument for Precise and Standardized Ecological Luminescence Measurement. IEEE Transactions on Instrumentation and Measurement 24, 306–313. doi:10.1109/TIM.1975.4314448.

Porcar-Castell, A., Malenovský, Z., Magney, T., Wittenberghe, S.V., Fernández-marín, B., Maignan, F., Zhang, Y., Maseyk, K., Atherton, J., Albert, L.P., Robson, T.M., Zhao, F., Ensminger, I., Rajewicz, P.A., Grebe, S., 2021. Chlorophyll a fluorescence illuminates a path connecting plant molecular biology to Earth-system science. Nature plants 7.

Porcar-Castell, A., Tyystjärvi, E., Atherton, J., van der Tol, C., Flexas, J., Pfündel, E.E., Moreno, J., Frankenberg, C., Berry, J.A., 2014. Linking chlorophyll a fluorescence to photosynthesis for remote sensing

applications: mechanisms and challenges. Journal of Experimental Botany 65, 4065–4095.

Qiu, B., Xue, Y., Fisher, J.B., Guo, W., Berry, J.A., Zhang, Y., 2018. Satellite Chlorophyll Fluorescence and Soil Moisture Observations Lead to Advances in the Predictive Understanding of Global Terrestrial Coupled Carbon-Water Cycles. Global Biogeochemical Cycles 32, 360–375.

Qiu, R., Li, X., Han, G., Xiao, J., Ma, X., Gong, W., 2022. Monitoring drought impacts on crop productivity of the U.S. Midwest with solar-induced fluorescence: GOSIF outperforms GOME-2 SIF and MODIS NDVI, EVI, and NIRv. Agricultural and Forest Meteorology 323, 109038. doi:10.1016/j.agrformet.2022.109038.

Rabinowitsch, E., Govindjee, 1969. Photosynthesis. John Wiley & Sons, INC, New York.

Rasmussen, M., Minteer, S.D., 2014. Photobioelectrochemistry: Solar Energy Conversion and Biofuel Production with Photosynthetic Catalysts. Journal of The Electrochemical Society 161, H647–H655. doi:10.1149/2.0651410jes.

Rawls, W.J., Brakensiek, D.L., 1985. Prediction of soil water properties for hydrologic modeling, in: Watershed management in the eighties, ASCE. pp. 293–299.

Reichstein, M., Falge, E., Baldocchi, D., Papale, D., Aubinet, M., Berbigier, P., Bernhofer, C., Buchmann, N., Gilmanov, T., Granier, A., Grünwald, T., Havránková, K., Ilvesniemi, H., Janous, D., Knohl, A., Laurila, T., Lohila, A., Loustau, D., Matteucci, G., Meyers, T., Miglietta, F., Ourcival, J.M., Pumpanen, J., Rambal, S., Rotenberg, E., Sanz, M., Tenhunen, J., Seufert, G., Vaccari, F., Vesala, T., Yakir, D., Valentini, R., 2005. On the separation of net ecosystem exchange into assimilation and ecosystem respiration: Review and improved algorithm. Global Change Biology 11, 1424–1439.

Robbins, N.E., Dinneny, J.R., 2018. Growth is required for perception of water availability to pattern root branches in plants. Proceedings of the National Academy of Sciences of the United States of America 115, E822–E831. doi:10.1073/pnas.1710709115.

Roman, D., Novick, K., Brzostek, E., Dragoni, D., Rahman, F., Phillips, R., 2015. The role of isohydric and anisohydric species in determining ecosystemâĂŚscale response to severe drought. Oecologia 179, 641–654.

Rouse, J., Haas, R., Schell, J., Deering, D., 1973. Monitoring vegetation systems in the Great Plains with ERTS, in: Third ERTS Symposium, pp. 309–317.

Ryu, Y., Berry, J.A., Baldocchi, D.D., 2019. Remote Sensing of Environment What is global photosynthesis ? History , uncertainties and opportunities 223, 95–114.

Sabater, N., Alonso, L., Cogliati, S., Vicent, J., Tenjo, C., Verrelst, J., Moreno, J., 2015. A sun-induced vegetation fluorescence retrieval method from top of atmosphere radiance for the flex/sentinel-3 tandem mission. IEEE International Geoscience and Remote Sensing Symposium (IGARSS) 3, 2669–2672.

Sade, N., Gebremedhin, A., Moshelion, M., 2012. Risk-taking plants. Plant signaling and behavior 7, 767–770.

Schreiber, U., Schliwa, U., Bilger, W., 1986. Continuous recording of photochemical and non-photochemical chlorophyll fluorescence quenching with a new type of modulation fluorometer. Photosynthesis Research 10, 51–62. doi:10.1007/BF00024185.

Sepulcre-Canto, G., Horion, S., Singleton, A., Carrao, H., Vogt, J., 2012. Development of a Combined Drought Indicator to detect agricultural drought in Europe. Biogeosciences 12, 3519–3531. doi:10.5194/nhess-12-3519-2012.

Short Gianotti, D.J., Rigden, A.J., Salvucci, G.D., Entekhabi, D., 2019. Satellite and Station Observations Demonstrate Water Availability's Effect on Continental-Scale Evaporative and Photosynthetic Land Surface Dynamics. Water Resources Research 55, 540–554. doi:10.1029/2018WR023726.

Simunek, J., Suarez, D., 1993. Modeling of carbon dioxide transport and production in soil 1. model development. Water Resources Research 29, 484–497.

Siqueira, M., Katul, G., Porporato, A., 2009. Soil moisture feedbacks on convection triggers: The role of soil-plant hydrodynamics. Journal of Hydrometeorology 10, 96–112. doi:10.1175/2008JHM1027.1.

Snider, J., Collins, G., Whitaker, J., Perry, C., Chastian, D., 2014. Electron transport through photosystem II is not limited by a wide range of water deficit conditions in field-grown Gossypium hirsutum. Journal of Agronomy and Crop Science 209, 77–82.

Sperdouli, I., Moustakas, M., 2012. Interaction of proline, sugars, and anthocyanins during photosynthetic acclimation of Arabidopsis

thaliana to drought stress. Journal of Plant Physiology 169, 577–585. doi:10.1016/j.jplph.2011.12.015.

Sperry, J.S., Love, D.M., 2015. What plant hydraulics can tell us about responses to climate-change droughts. New Phytologist 207, 14–27. doi:10.1111/nph.13354.

Spitters, C., van Keulen, H., van Kraailingen, D., 1988. A simple but universal crop growth simulation model, SUCROS87. Simulation monographs, PUDOC, Wageningen.

Stirbet, A., Lazár, D., Kromdijk, J., Govindjee, 2018. Chlorophyll a fluorescence induction: Can just a one-second measurement be used to quantify abiotic stress responses? Photosynthetica 56, 86–104. doi:10.1007/s11099-018-0770-3.

Sulman, B.N., Roman, D.T., Yi, K., Wang, L., Phillips, R.P., Novick, K.A., 2016. High atmospheric demand for water can limit forest carbon uptake and transpiration as severely as dry soil. Geophysical Research Letters 43, 9686–9695. doi:10.1002/2016GL069416.

Sun, Y., Fu, R., Dikinson, R., Joiner, J., Frankenberg, C., Gu, L., Xia, Y., Fernando, N., 2015. Drought onset mechanisms revealed by satellite solar-induced chlorophyll fluorescence: Insights from two contrasting extreme events. Journal of Geophysical Research: Biogeosciences 120, 707–723. doi:10.1002/2015JG003150.Received.

Svadoba, M., LeCompte, D., Hayes, M., Heim, R., Gleason, K., Angel, J., Rippey, B., Tinker, R., Palecki, M., Stooksbury, D., Miskus, D., Stephens, S., 2002. The drought monitor. Bulletins of the American Meteorological Sociecty , 1181–1190.

Tagesson, T., Fensholt, R., Guiro, I., Rasmussen, M.O., Huber, S., Mbow, C., Garcia, M., Horion, S., Sandholt, I., Holm-Rasmussen, B., Göttsche, F.M., Ridler, M.E., Olén, N., Lundegard Olsen, J., Ehammer, A., Madsen, M., Olesen, F.S., Ardö, J., 2015. Ecosystem properties of semiarid savanna grassland in West Africa and its relationship with environmental variability. Global Change Biology 21, 250–264. doi:10.1111/gcb.12734.

Tardieu, F., Simonneau, T., Parent, B., 2015. Modelling the coordination of the controls of stomatal aperture, transpiration, leaf growth, and abscisic acid: Update and extension of the Tardieu-Davies model. Journal of Experimental Botany 66, 2227–2237. doi:10.1093/jxb/erv039.

van der Tol, C., Rossini, M., Cogliati, S., Verhoef, W., Colombo, R., Rascher, U., Mohammed, G., 2016. A model and measurement comparison of diurnal cycles of sun-induced chlorophyll fluorescence of crops. Remote Sensing of Environment 186, 663–677.

Tolomio, M., Casa, R., 2020. Dynamic crop models and remote sensing irrigation decision support systems: A review of water stress concepts for improved estimation of water requirements. Remote Sensing 12, 1–34.

Trigo-Córdoba, E., Bouzas-Cid, Y., Orriols-Fernández, I., Mirás-Avalos, J.M., 2015. Effects of deficit irrigation on the performance of grapevine (Vitis vinifera L.) cv. 'Godello' and 'Treixadura' in Ribeiro, NW Spain. Agricultural Water Management 161, 20–30. doi:10.1016/j.agwat.2015.07.011.

United States Department of Agriculture, 1987. USDA Textural Soil Classification.

van der Tol, C., Berry, J.A., Campbell, P.K., Rascher, U., 2014. Models of fluorescence and photosynthesis for interpreting measurements of solar-induced chlorophyll fluorescence. Journal of Geophysical Research: Biogeosciences 119, 2312–2327. doi:10.1002/2014JG002713.

van der Tol, C., Verhoef, W., Timmermans, J., Verhoef, A., Su, Z., 2009. An integrated model of soil-canopy spectral radiances, photosynthesis, fluorescence, temperature and energy balance. Biogeosciences 6, 3109–3129.

Vanlerberghe, G.C., Martyn, G.D., Dahal, K., 2016. Alternative oxidase: a respiratory electron transport chain pathway essential for maintaining photosynthetic performance during drought stress. Physiologia plantarum 157, 322–337. doi:10.1111/ppl.12451.

Venturas, M.D., Todd, H.N., Trugman, A.T., Anderegg, W.R.L., 2021. Understanding and predicting forest mortality in the western United States using longâĂŘterm forest inventory data and modeled hydraulic damage. New Phytologist 230, 1896–1910. doi:10.1111/nph.17043.

Vereecken, H., Huisman, J.A., Bogena, H., Vanderborght, J., Vrugt, J.A., Hopmans, J.W., 2008. On the value of soil moisture measurements in vadose zone hydrology: A review. Water Resources Research 46, 1–21.

Vereecken, H., Schnepf, A., Hopmans, J.W., Javaux, M., Or, D., Roose, T., Vanderborght, J., Young, M.H., Amelung, W., Aitkenhead, M.,

Allison, S.D., Assouline, S., Baveye, P., Berli, M., Brüggemann, N., Finke, P., Flury, M., Gaiser, T., Govers, G., Ghezzehei, T., Hallett, P., Franssen, H.J.H., Heppell, J., Horn, R., Huisman, J.A., Jacques, D., Jonard, F., Kollet, S., Lafolie, F., Lamorski, K., Leitner, D., Mcbratney, A., Minasny, B., Montzka, C., Nowak, W., Pachepsky, Y., Padarian, J., Romano, N., Roth, K., Rothfuss, Y., Rowe, E.C., Schwen, A., ŠimÅŕnek, J., Tiktak, A., Dam, J.V., Zee, S.E.A.T.M.V.D., Vogel, H.J., Vrugt, J.A., Wöhling, T., Young, I.M., 2016. Modeling Soil Processes : Review , Key Challenges , and New Perspectives 6 A Brief History of Soil Modeling. Vadose Zone Journal 15. doi:10.2136/vzj2015.09.0131.

Vergeynst, L.L., Dierick, M., Bogaerts, J.A., Cnudde, V., Steppe, K., 2015. Cavitation: A blessing in disguise? New method to establish vulnerability curves and assess hydraulic capacitance of woody tissues. Tree Physiology 35, 400–409. doi:10.1093/treephys/tpu056.

Verhoef, A., Egea, G., 2014. Modeling plant transpiration under limited soil water: Comparison of different plant and soil hydraulic parameterizations and preliminary implications for their use in land surface models. Agricultural and Forest Meteorology 191, 22–32.

Verhoef, W., Jia, L., Xiao, Q., Su, Z., 2007. Unified optical-thermal four-stream radiative transfer theory for homogeneous vegetation canopies. IEEE Transactions on Geoscience and Remote Sensing 45, 1808–1822.

Verrelst, J., Pablo Rivera, J., Van Der Tol, C., Magnani, F., Mohammed, G., Moreno, J., 2015. Global sensitivity analysis of the SCOPE model; What drives simulated canopy-leaving sun-induced fluorescence? Remote Sensing of Environment 8, 55.

Vilfan, N., van der Tol, C., Verhoef, W., 2019. Estimating photosynthetic capacity from leaf reflectance and Chl fluorescence by coupling radiative transfer to a model for photosynthesis. New Phytologist 223, 487–500.

Vincent, C., Rowland, D.L., Schaffer, B., 2015. The potential for primed acclimation in papaya (Carica papaya L.): Determination of critical water deficit thresholds and physiological response variables. Scientia Horticulturae 194, 344–352. doi:10.1016/j.scienta.2015.08.032.

Vroege, W., Dalhaus, T., Finger, R., 2019. Index insurances for grasslands - A review for Europe and North America. Agricultural Systems , 101–111.

Wang, N., Yang, P., Clevers, J.G.P.W., Wieneke, S., Kooistra, L., 2023. Decoupling physiological and non-physiological responses of sugar beet to water stress from sun-induced chlorophyll fluorescence Remote Sensing of Environment Decoupling physiological and non-physiological responses of sugar beet to water stress from sun-. Remote Sensing of Environment 286, 113445. doi:10.1016/j.rse.2022.113445.

Wang, X., Wang, L., Shangguan, Z., 2016. Leaf gas exchange and fluorescence of two winter wheat varieties in response to drought stress and nitrogen supply. PLoS ONE 11, 1–15. doi:10.1371/journal.pone.0165733.

Wankmüller, F.J.P., Carminati, A., 2021. Stomatal regulation prevents plants from critical water potentials during drought: Result of a model linking soilâĂŞplant hydraulics to abscisic acid dynamics. Ecohydrology , 1–15doi:10.1002/eco.2386.

West, H., Quinn, N., Horswell, M., 2019. Remote sensing for drought monitoring and impact assessment: Progress, past challenges and future opportunities. Remote Sensing of Environment 232, 111291. doi:10.1016/j.rse.2019.111291.

West, H., Quinn, N., Horswell, M., White, P., 2018. Assessing vegetation response to soil moisture fluctuation under extreme drought using sentinel-2. Water (Switzerland) 10, 1–22. doi:10.3390/w10070838.

White, J., Berg, A.A., Champagne, C., Zhang, Y., Chipanshi, A., Daneshfar, B., 2020. Improving crop yield forecasts with satellite-based soil moisture estimates: An example for township level canola yield forecasts over the Canadian Prairies. International Journal of Applied Earth Observation and Geoinformation 89. doi:10.1016/j.jag.2020.102092.

Wieneke, S., Ahrends, H., Damm, A., Pinto, F., Stadler, A., Rossini, M., Rascher, U., 2016. Remote Sensing of Environment Airborne based spectroscopy of red and far-red sun-induced chlorophyll fl uorescence : Implications for improved estimates of gross primary productivity. Remote Sensing of Environment 184, 654–667. doi:10.1016/j.rse.2016.07.025.

Wieneke, S., Burkart, A., Cendrero-mateo, M.P., Julitta, T., Rossini, M., Schickling, A., 2018. Linking photosynthesis and sun-induced fluorescence at sub-daily to seasonal scales. Remote Sensing of Environment 219, 247–258.

Wohlfahrt, G., Gerdel, K., Migliavacca, M., Rotenberg, E., Tatarinov, F., Müller, J., Hammerle, A., Julitta, T., Spielmann, F.M., Yakir, D., 2018. Sun-induced fluorescence and gross primary productivity during a heat wave. Scientific Reports 8, 1–9. doi:10.1038/s41598-018-32602-z.

Wong, C.Y., Gamon, J.A., 2015. Three causes of variation in the photochemical reflectance index (PRI) in evergreen conifers. New Phytologist 206, 187–195. doi:10.1111/nph.13159.

Wong, C.Y.S., Young, D.J.N., Latimer, A.M., Buckley, T.N., Magney, T.S., 2021. Remote Sensing of Environment Importance of the legacy effect for assessing spatiotemporal correspondence between interannual tree-ring width and remote sensing products in the Sierra Nevada. Remote Sensing of Environment 265, 112635. doi:10.1016/j.rse.2021.112635.

Wu, F.Z., Bao, W.K., Li, F.L., Wu, N., 2008. Effects of water stress and nitrogen supply on leaf gas exchange and fluorescence parameters of Sophora davidii seedlings. Photosynthetica 46, 40–48. doi:10.1007/s11099-008-0008-x.

Wu, G., Guan, K., Li, Y., Novick, K.A., Feng, X., McDowell, N.G., Konings, A.G., Thompson, S.E., Kimball, J.S., De Kauwe, M.G., Ainsworth, E.A., Jiang, C., 2021. Interannual variability of ecosystem iso/anisohydry is regulated by environmental dryness. New Phytologist 229, 2562–2575. doi:10.1111/nph.17040.

Wu, G., Guan, K., Li, Y., Novick, K.A., Konings, A.G., Thompson, S.E., Kimball, J.S., Kauwe, M.G.D., 2020. Interannual variability of ecosystem iso / anisohydry is regulated by environmental dryness doi:10.1111/nph.17040.

Wutzler, T., Lucas-Moffat, A., Migliavacca, M., Knauer, J., Sickel, K., Šigut, L., Menzer, O., Reichstein, M., 2018. Basic and extensible post-processing of eddy covariance flux data with REddyProc. Biogeosciences 15, 5015–5030.

Xia, J.B., Zhang, G.C., Wang, R.R., Zhang, S.Y., 2014. Effect of soil water availability on photosynthesis in Ziziphus jujuba var. spinosus in a sand habitat formed from seashells: Comparison of four models. Photosynthetica 52, 253–261. doi:10.1007/s11099-014-0030-0.

Xu, S., Atherton, J., Riikonen, A., Zhang, C., Oivukkamäki, J., MacArthur, A., Honkavaara, E., Hakala, T., Koivumäki, N., Liu, Z., Porcar-Castell, A., 2021. Structural and photosynthetic dynamics

mediate the response of SIF to water stress in a potato crop. Remote Sensing of Environment 263. doi:10.1016/j.rse.2021.112555.

Xu, Z., Zhou, G., 2011. Responses of photosynthetic capacity to soil moisture gradient in perennial rhizome grass and perennial bunchgrass. BMC Plant Biology 11. doi:10.1186/1471-2229-11-21.

Yang, K., Ryu, Y., Dechant, B., Berry, J.A., Hwang, Y., Jiang, C., Kang, M., Kim, J., Kimm, H., Kornfeld, A., Yang, X., 2018a. Sun-induced chlorophyll fluorescence is more strongly related to absorbed light than to photosynthesis at half-hourly resolution in a rice paddy. Remote Sensing of Environment 216, 658–673. doi:10.1016/j.rse.2018.07.008.

Yang, K., Ryu, Y., Dechant, B., Berry, J.A., Hwang, Y., Jiang, C., Kang, M., Kim, J., Kimm, H., Kornfeld, A., Yang, X., 2018b. Sun-induced chlorophyll fluorescence is more strongly related to absorbed light than to photosynthesis at half-hourly resolution in a rice paddy. Remote Sensing of Environment 216, 658–673.

Yang, P., 2022. Exploring the interrelated effects of soil background, canopy structure and sun-observer geometry on canopy photochemical reflectance index. Remote Sensing of Environment 279. doi:10.1016/j.rse.2022.113133.

Yang, P., van der Tol, C., 2018. Linking canopy scattering of far-red sun-induced chlorophyll fluorescence with reflectance. Remote Sensing of Environment 209, 456–467.

Yang, P., van der Tol, C., Campbell, P.K., Middleton, E.M., 2020. Fluorescence Correction Vegetation Index (FCVI): A physically based reflectance index to separate physiological and non-physiological information in far-red sun-induced chlorophyll fluorescence. Remote Sensing of Environment 240. doi:10.1016/j.rse.2020.111676.

Zarco-Tejada, P.J., González-Dugo, V., Berni, J.A., 2012. Fluorescence, temperature and narrow-band indices acquired from a UAV platform for water stress detection using a micro-hyperspectral imager and a thermal camera. Remote Sensing of Environment 117, 322–337. doi:10.1016/j.rse.2011.10.007.

Zeng, Y., Chen, M., Hao, D., Damm, A., Badgley, G., Rascher, U., Johnson, J.E., Dechant, B., Siegmann, B., Ryu, Y., Qiu, H., Krieger, V., Panigada, C., Celesti, M., Miglietta, F., Yang, X., Berry, J.A., 2022. Combining near-infrared radiance of vegetation and fluorescence

spectroscopy to detect effects of abiotic changes and stresses. Remote Sensing of Environment 270.

Zhang, J., Guan, K., Peng, B., Pan, M., Zhou, W., Jiang, C., Kimm, H., Franz, T.E., Grant, R.F., Yang, Y., Rudnick, D.R., Heeren, D.M., Suyker, A.E., Bauerle, W.L., Miner, G.L., 2021. Sustainable irrigation based on co-regulation of soil water supply and atmospheric evaporative demand. Nature Communications 12. doi:10.1038/s41467-021-25254-7.

Zhang, Y., Fang, J., Smith, W., Wang, X., Gentine, P., Scott, R., Migliavacca, M., Jeong, S., Litvak, M., Zhou, S., 2023. Satellite solar-induced chlorophyll fluorescence tracks physiological development during 2020 southwest US drought drought stress Running. Global Change Biology , 1–15doi:10.1111/gcb.16683.

Zhao, W., Wu, J., Shen, Q., Yang, J., Han, X., 2022. Exploring the Ability of Solar-Induced Chlorophyll Fluorescence for Drought Monitoring Based on an Intelligent Irrigation Control System. Remote Sensing 14. doi:10.3390/rs14236157.

Zhou, S., Duursma, R.A., Medlyn, B.E., Kelly, J.W., Prentice, I.C., 2013. How should we model plant responses to drought? An analysis of stomatal and non-stomatal responses to water stress. Agricultural and Forest Meteorology 182-183, 204–214. doi:10.1016/j.agrformet.2013.05.009.

Zhou, S., Medlyn, B., Sabaté, S., Sperlich, D., Colin Prentice, I., 2014. Short-term water stress impacts on stomatal, mesophyll and biochemical limitations to photosynthesis differ consistently among tree species from contrasting climates. Tree Physiology 34, 1035–1046.

Zhou, Z., Majeed, Y., Diverres Naranjo, G., Gambacorta, E.M., 2021. Assessment for crop water stress with infrared thermal imagery in precision agriculture: A review and future prospects for deep learning applications. Computers and Electronics in Agriculture 182. doi:10.1016/j.compag.2021.106019.

Zoogman, P., Liu, X., Suleiman, R.M., Pennington, W.F., Flittner, D.E., Al-Saadi, J.A., Hilton, B.B., Nicks, D.K., Newchurch, M.J., Carr, J.L., Janz, S.J., Andraschko, M.R., Arola, A., Baker, B.D., Canova, B.P., Chan Miller, C., Cohen, R.C., Davis, J.E., Dussault, M.E., Edwards, D.P., Fishman, J., Ghulam, A., González Abad, G., Grutter, M., Herman, J.R., Houck, J., Jacob, D.J., Joiner, J., Kerridge, B.J., Kim, J., Krotkov, N.A., Lamsal, L., Li, C., Lindfors, A., Martin, R.V., McEl-

roy, C.T., McLinden, C., Natraj, V., Neil, D.O., Nowlan, C.R., OŒş-Sullivan, E.J., Palmer, P.I., Pierce, R.B., Pippin, M.R., Saiz-Lopez, A., Spurr, R.J., Szykman, J.J., Torres, O., Veefkind, J.P., Veihelmann, B., Wang, H., Wang, J., Chance, K., 2017. Tropospheric emissions: Monitoring of pollution (TEMPO). Journal of Quantitative Spectroscopy and Radiative Transfer 186, 17–39. doi:10.1016/j.jqsrt.2016.05.008.

Zwieniecki, M.A., Holbrook, N.M., 2009. Confronting Maxwell's demon: biophysics of xylem embolism repair. Trends in Plant Science 14, 530–534. doi:10.1016/j.tplants.2009.07.002.

Abstract

During droughts, plants have to make a trade-off between minimizing water loss and allowing CO_2 uptake. This trade-off is regulated with the stomatal guard cells, the opening of which determines the joint gas exchange of CO_2 and water with the atmosphere. The decrease of the CO_2 uptake slows down the entire photosynthetic machinery, causing various reactions at the level of the photosystem. Amidst these reactions, the decrease of the CO_2 uptake changes the sun-induced chlorophyll fluorescence emission, making it an interesting signal for drought stress detection. However, many questions arise regarding the translation of the physiological processes to remote-sensing data. This is where this thesis jumps in: by studying chlorophyll fluorescence at various scales, it makes a journey from the photosystems, over the leaf and plot scales, to the global scale. At the photosystem scale, there is a clear difference in the partitioning of absorbed energy between photosynthesis, non-photochemical quenching and fluorescence emission between stressed and unstressed plants. This sensitivity can serve as the backbone of the calibration for a stress module in a crop growth model, as SIF provides a measured basis of stress intensity. Such an approach improved spectacularly the estimations of the field-scale carbon and water fluxes during the Summer months. The sensitivity between the photosystem-level fluorescence emission and the stress intensity was also observable at the global scale through a combination of satellite data. The precise nature of the SIF-stress relationship of a certain location was affected by the local isohydricity. The sensitivity of the fluorescence signal to stress conditions at both the local and global scale is promising in light of the upcoming FLuorescence EXplorer (FLEX) mission, scheduled for launch in 2025.

About the author

Simon De Cannière was born on November 28, 1995 in Antwerp, Belgium. He hold a Bsc. in Bioscience Engineering from the University of Antwerp (2016), Belgium and an Msc. in from KULeuven (2018). During his Msc. degree, he participated in a 6-month exchange with the Universität für Bodenkultur (BOKU), in Vienna, Austria. He wrote his Msc. thesis on the radiative transfer modelling of L-band passive microwave data over peatlands under supervision of Prof. Gabriëlle De Lannoy and Dr. Michel Bechtold. In October 2018, he started his Ph.D. research under the supervision of Prof. François Jonard and Prof. Pierre Defourny on a UCLouvain FSR (Fonds Special de Recherche) grant at the Earth and Life Institute at UCLouvain. The year after, he passed on a FRIA (Fonds pour la Formation à la Recherche dans l'Industrie et dans l'Agriculture) grant. The Ph.D. research was conducted in close collaboration with the Forschungszentrum Jülich, Germany. This collaboration was especially fruitful for the experimental part of the thesis. Within the context of the MISTI Initiative, he collaborated with the group of Prof. Dara Entekhabi at the Massachusetts Institute of Technology. This collaboration was fruitful for the use of the spaceborne fluorescence data at the global scale.

